Cross Section Measurements of $^{13}C(d, p)^{14}C$ Reaction at Sub-Coulomb Barrier Energies

by

Shariq Uddin Kidwai

A Thesis Presented to the

FACULTY OF THE COLLEGE OF GRADUATE STUDIES

KING FAHD UNIVERSITY OF PETROLEUM & MINERALS

DHAHRAN, SAUDI ARABIA

In Partial Fulfillment of the
Requirements for the Degree of

MASTER OF SCIENCE

In

PHYSICS

December, 1996

INFORMATION TO USERS

This manuscript has been reproduced from the microfilm master. UMI films the text directly from the original or copy submitted. Thus, some thesis and dissertation copies are in typewriter face, while others may be from any type of computer printer.

The quality of this reproduction is dependent upon the quality of the copy submitted. Broken or indistinct print, colored or poor quality illustrations and photographs, print bleedthrough, substandard margins, and improper alignment can adversely affect reproduction.

In the unlikely event that the author did not send UMI a complete manuscript and there are missing pages, these will be noted. Also, if unauthorized copyright material had to be removed, a note will indicate the deletion.

Oversize materials (e.g., maps, drawings, charts) are reproduced by sectioning the original, beginning at the upper left-hand corner and continuing from left to right in equal sections with small overlaps. Each original is also photographed in one exposure and is included in reduced form at the back of the book.

Photographs included in the original manuscript have been reproduced xerographically in this copy. Higher quality 6" x 9" black and white photographic prints are available for any photographs or illustrations appearing in this copy for an additional charge. Contact UMI directly to order.

UMI

A Bell & Howell Information Company
300 North Zeeb Road, Ann Arbor MI 48106-1346 USA
313/761-4700 800/521-0600

CROSS SECTION MEASUREMENTS OF $^{13}C(d, p)^{14}C$ REACTION AT SUB-COULOMB BARRIER ENERGIES

BY

Shariq Uddin Kidwai

A Thesis Presented to the

FACULTY OF THE COLLEGE OF GRADUATE STUDIES

KING FAHD UNIVERSITY OF PETROLEUM & MINERALS

DHAHRAN, SAUDI ARABIA

In Partial Fulfillment of the
Requirements for the Degree of

MASTER OF SCIENCE
In
PHYSICS

DECEMBER, 1996

KING FAHAD UNIVERSITY OF PETROLEUM AND MINERALS
DHAHRAN 31261, SAUDIA ARABIA

COLLEGE OF GRADUATE STUDIES

This thesis, written by ***Shariq Uddin Kidwai*** under the direction of his Thesis Advisor and approved by his Thesis Committee, has been presented to and accepted by the Dean of the College of Graduate Studies, in partial fulfillment of the requirements for the degree of MASTER OF SCIENCE in PHYSICS.

Thesis Committee

Dr. Nagadi M.M.
Thesis Advisor

Dec. 28, 1996
Dr. Naqvi A.A.
Thesis Co-advisor

Dec. 28, 1996
Dr. Abdelmonem M.S.
Member

28-Dec-1996
Dr. Khiari F.Z.
Member

Department Chairman

Dean, College of Graduate Studies

31-12-1996
Date

كلية الدراسات العليا
COLLEGE OF GRADUATE STUDIES

DEDICATED
TO
MY LATE FATHER

ACKNOWLEDEMENT

First and foremost, praise and thanks be to Almighty ALLAH, the most Gracious, the most Merciful without whose help no work can be accomplished; and peace be upon His Prophet.

Acknowledgement is due to the Physics department of King Fahd University of Petroleum and Minerals and Energy Resources Laboratories of Research Institute for their facilities and support provided for the completion of this research.

I wish to express my sincere appreciation to Dr. Mahmoud Nagadi, my thesis advisor, for his continuous guidance and encouragement throughout this study.

I would like to express my gratefulness to my thesis co-advisor Dr. Akhtar Naqvi for his valuable assistance and guidance during the course of this work, be it was data taking task, analysis part or the write-up of this manuscript. I will always be in debt to him. Thanks are also due to my thesis committee members, Dr. Mohamed Abdelmonem and Dr. Fatah Khiari for their support, advice and constructive criticism.

Also I like to extend my deep appreciation to Mr. Muhammad Raashid for operating the accelerator.

My heartfelt thanks and gratefulness also go to my mother and to my other family members for their support and encouragement for my education.

Finally the cooperation of the department chairman Dr. Muhammad Garwan is gratefully appreciated.

CROSS SECTION MEASUREMENTS OF $^{13}C(d, p)^{14}C$ REACTION AT SUB-COULOMB BARRIER ENERGIES

Shariq Uddin Kidwai

PHYSICS

DECEMBER, 1996

TABLE OF CONTENTS

LIST OF FIGURES

LIST OF TABLES

ABSTRACT (English)

NAME: SHARIQ UDDIN KIDWAI
TITLE: CROSS SECTION MEASUREMENTS OF $^{13}C(d, p)^{14}C$ REACTION AT SUB-COULOMB BARRIER ENERGIES
MAJOR: PHYSICS
DATE: DECEMBER 1996

Excitation functions and differential cross section of $^{13}C(d, p)^{14}C$ reaction were measured for 200-350 keV deuteron energies to learn about the cause of disagreement between Distorted Wave Born Approximation (DWBA) theory and experimental data at 410-810 keV deuteron energies. The differential cross sections of $^{13}C(d, p)^{14}C$ reaction at 350, 335, 310, 290, 270, 250 and 200 keV energies were fitted with DWBA model of nuclear transfer reactions using finite range approximation. An excellent agreement between the DWBA calculations and experimental data shows that only one-step stripping reaction contributes to the $^{13}C(d, p)^{14}C$ reaction at these energies. This also excludes any contribution of compound nucleus towards the cross section data at these energies. The Optical Model Potential (OMP) parameters obtained for $^{13}C(d, p)^{14}C$ reaction are in agreement with the OMP parameters at higher energies. The significantly small values of OMP parameters of the DWBA fit to $^{13}C(d, p)^{14}C$ reaction data at 410-810 keV energies were not observed in this study. This study has provided experimental cross section data of $^{13}C(d, p)^{14}C$ reaction below 350 keV deuteron energy. This data can be used to calculate vector and tensor analyzing powers of $^{13}C(d, p)^{14}C$ reaction at these energies.

MASTER OF SCIENCE DEGREE

KING FAHD UNIVERSITY OF PETROLEUM AND MINERALS
Dhahran, Saudi Arabia

December, 1996

خلاصة الرسالة

اسم الطالب الكامل : شارق الدين قدوائي

عنوان الدراسة : قياس مساحة المقطع للتفاعل كربون١٣ (ديوترون، بروتون) كربون١٤ لطاقات ما تحت الكولمبي

التخصص : فيـزيـاء

تاريخ الشهادة : ديسمبر ١٩٩٦م - شعبان ١٤١٧ هـ

لقد قيست الدوال المثارة ومساحة المقطع الزاوي للتفاعل كربون١٣ (ديوترون ، بروتون) كربون١٤ لطاقات الديوترون ما بين ٢٠٠ - ٣٥٠ كيلو الكترون فولت لنتعلم عن سبب التخالف بين نظرية تقريب بورن للموجات المشوهة والنتائج العملية لطاقات الديوترون ما بين ٤١٠ - ٨١٠ كيلو الكترون فولت. لقد قورنت النتائج العلمية لقياسات مساحة المقطع الزاوي كربون١٣ (ديوترون ، بروتون) كربون١٤ عند الطاقات ٣٥٠و٣٣٥ و٣١٠و٢٩٠و٢٧٠و٢٥٠و٢٠٠ كيلو الكيرون فولت بالحسابات النظرية بإستخدام تقريب بورن للموجات المشوهة للتفاعلات النووية المحولة مستعملا تقريب المدى المحدود. وقد وجد اتفاق ممتاز بينهما. وقد بين هذا الاتفاق أن المساهم الوحيد لهذا التفاعل ناتج من التفاعل النزعي ذوالخطوة الواحدة عند هذه الطاقات. وهذا يعني عدم مساهمة مساحة القطع الناتج من النواة المركبة عند هذه الطاقات. وقد وجد أن المتغيرات لنظرية الجهد الضوئي التي استنتجت لهذا التفاعل على اتفاق مع نظيراتها عند طاقات اعلى. وقد لوحظ أن القيم الصغيرة لبعض هذه المتغيرات عند الطاقات ٤١٠ - ٨١٠ كيلو الكترون فولت غير موجود في الدراسة الحالية، وجدير بالذكر أن الدراسة الحالية قد اعطت النتائج للمرة الاولى لمساحة المقطع للتفاعل كربون١٣ (ديوترون ، بروتون) كربون١٤ لطاقات اقل من ٣٥٠ كيلو الكترون فولت وأن هذه النتائج يمكن استخدامها في حساب القوة التحليلية المتجهة والممتدة عند هذه الطاقات.

درجة الماجستير في العلوم

جامعة الملك فهد للبترول والمعادن

الظهران ، المملكة العربية السعودية

ديسمبر ١٩٩٦م - شعبان ١٤١٧ هـ

CHAPTER 1

INTRODUCTION

The nuclear transfer reaction data provide useful information about the angular momenta of the transferred nucleon and the spectroscopic factor S [1,2]. The spectroscopic factor S depends upon the single particles states involved in the transfer reaction. The orbital angular momentum L of the transferred nucleon is determined from the angular distribution of the transfer reaction for unpolarized beam while the total angular momentum j is determined from the angular distribution of the transfer reaction for polarized beam (analyzing power measurements) [2]. One can also obtain information about D-states affects in wave function of few nucleon system from analyzing power of nuclear transfer reactions at sub-Coulomb barrier energies.

Transfer reaction studies are initiated at 350 kV accelerator laboratory of Energy Research Laboratories (ERL) using unpolarized and polarized deuteron and proton beams. The cross section measurements for $^{13}C(d, p)^{14}C$ reaction was carried as part of the nuclear transfer reaction program. Due to maximum energy limitation of the accelerator to 350 keV, nuclear transfer reactions with large positive Q-values are preferred. ^{13}C+d system had been chosen due to its large positive Q-values for (d, p), (d, α_0), (d, α_1) and (d, t) channels. These reaction channels can be studied simultaneously and the reaction protons, α-particles and the tritons with MeV energies

can easily be separated from background of the incident low energy beam. The Q-values of $^{13}C(d, p)^{14}C$, $^{13}C(d, \alpha_0)^{11}B$, $^{13}C(d, \alpha_1)^{11}B^*$ and $^{13}C(d, t)^{12}C$ reactions are 5.947, 5.167, 3.307 and 1.313 MeV respectively.

Another reason to study $^{13}C(d, p)^{14}C$ reaction was the disagreement between experimental differential cross section data of Putt [1] for $^{13}C(d, p)^{14}C$ reaction at 410-810 keV and DWBA calculations. He fitted the experimental cross section with Distorted Wave Born Approximation (DWBA) and compound nucleus corrections were carried out using Hauser-Feshbach calculations. The calculated cross section could not predict correct $^{13}C(d, p)^{14}C$ reaction cross section for angles above 110° over 410-810 keV deuteron energies. The other observation was the significantly small values of some of the geometrical parameters of the optical model potential parameters in Putt's data. Also $^{13}C(d, p)^{14}C$ reaction data is not available below 410 keV. The $^{13}C(d, p)^{14}C$ reaction data below 410 keV was also required to estimate the analyzing powers of $^{13}C(d, p)^{14}C$ reaction. These analyzing power measurements are going to be initiated at 350 kV accelerator in near future.

The lack of $^{13}C(d, p)^{14}C$ reaction data below 410 keV and the discrepancy between the theory and Putt data motivated us to carry out the study of $^{13}C(d, p)^{14}C$ stripping reaction at sub-Coulomb barrier energies. Although ERL accelerator cannot provide exactly the same energy as that in Putt experiment, but it can provide a maximum energy of 350 keV, an energy point close to the lowest energy used by Putt. It is assumed that nuclear effects do not show strong energy dependence over a small deuteron energy difference from 350-410 keV. Therefore one can learn from

$^{13}C(d, p)^{14}C$ reaction cross section at 200-350 keV about the cause of discrepancy between experimental data and DWBA theory at 410-810 keV.

This thesis contains the details of $^{13}C(d, p)^{14}C$ reaction cross section studies at 200-350 keV deuteron energies. The study was divided into four tasks namely two experimental tasks, one data reduction and experimental results task and one nuclear model fit task. First experimental task is related with the energy calibration of the KFUPM, ERL 350 kV accelerator. The calibration was carried out using nuclear resonance method. In this study resonance at 224 keV and 340 keV of $^{19}F(p, \alpha\gamma)^{16}O$ reaction were studied. This is discussed in chapter 2. The second experimental task consists of excitation functions and angular distributions measurements of the $^{13}C(d, p)^{14}C$ reaction. This task is described in chapter 3. The excitation functions of $^{13}C(d, p)^{14}C$ reaction were measured for eight angles at incident deuteron energies of 200-350 keV in 10 keV steps and angular distributions measurements of $^{13}C(d, p)^{14}C$ reaction were carried out for fourteen angles at 200, 250, 270, 290 310, 335 and 350 keV deuteron energies. The data reduction and experimental results of $^{13}C(d, p)^{14}C$ reaction data is discussed in chapter 4. Finally differential cross section data was fitted with the finite range DWBA code. The details of nuclear model fit to cross section data is given in chapter 5. The summary and conclusion of the present work is given separately in chapter 6.

CHAPTER 2

ACCELERATOR ENERGY CALIBRATION

Nuclear reactions and nuclear structure strongly depend upon the energy of probe particles. Generally these probe particles are accelerated using accelerators. Therefore, this requires precise determination of energy of the beam particles from the accelerator. The absolute energies of the particles beam from an accelerator are determined through electrostatic or magnetic analyzers. For magnetic and electrostatic analyzers the energy measurements are determined on 'absolute' scale using frequency standards. The magnetic and electrostatic analyzers provide precise data on Q-values and resonance energies of nuclear reactions as standards. Generally the Q-values and resonance energies data of the nuclear reactions is used to calibrate the accelerator beam energy [3]. The Q-value data is used for accelerator energy calibration against the reaction throughout the energy. In the reaction threshold method, the reaction yield is measured as a function of the accelerator voltage over particle energy range above and below the threshold energy. The two-third power of the yield is generally plotted as a function of the accelerator voltage and a straight-line is obtained. The intersection of this straight-line with the abscissa is the reaction Q-value [4]. On the other hand, the resonance method utilizes the assignment of resonance energy to the accelerator voltage corresponding to the mid-point of the maximum yield of the resonance

reaction. The resonance method is widely used for accelerator beam energy calibration. Table 2.1 shows some nuclear resonance reactions used for the calibration of low energy accelerator.

2.1 ACCELERATOR ENERGY CALIBRATION USING NUCLEAR RESONANCE REACTIONS

The energy calibration of the accelerator using a resonance nuclear reaction is generally carried out through excitation function measurement of the resonance reaction for a thick target. Then, the thick target yield curve is fitted with a function to determine the accelerator voltage corresponding to the resonance energy [5]. In the following section, the basic principle of the thick target yield curve is described briefly.

2.1.1 Principle of thick target yield measurement

When a charged particle traverses matter e.g. a nuclear target, it undergoes energy loss due to Coulomb excitation and nuclear reactions. A target is said to be thick if the energy loss of the beam is more than the width of the nuclear reaction under study. In nuclear studies with thick targets, the thickness of the target is generally several multiples of the resonance width. For a resonance reaction to take place in a thick target, the incident beam energy E_0, resonance energy E_R and energy loss ΔE_x in a single layer are related by the equation,

$$E_0 = E_R + n\,\Delta E_x$$

Table 2.1 **Resonance nuclear reactions used for energy calibration of low energy accelerators [4].**

Proton energy (keV)	Reaction	γ-ray energy (MeV)
163	$^{11}B(p, \gamma)^{12}C$	16.11, 11.68, 4.43
224	$^{19}F(p, \alpha\gamma)^{16}O$	7.12, 6.92, 6.13
226	$^{24}Mg(p, \gamma)^{25}Al$	2.06, 1.56, 0.95
317	$^{25}Mg(p, \gamma)^{26}Al$	6.19, 4.86, 0.82
326	$^{27}Al(p, \gamma)^{28}Si$	7.60, 7.20, 6.20
339	$^{26}Mg(p, \gamma)^{27}Al$	7.74, 5.85, 5.61
340	$^{19}F(p, \alpha\gamma)^{16}O$	7.12, 6.92, 6.13

For a beam energy E_0 equal to resonance energy E_R, n = 0, then the reaction will take place at the surface. If the beam energy is increased to $E_0 = E_R + \Delta E_x$, the reaction does not take place on the surface layer but it will take place in the first layer just after the surface. In this way, with increasing particle beam energy the location where the particle energy corresponds to the resonance energy is shifted deeper and deeper inside the target. Therefore, for a very thick target, the particle beam with relatively high energies can always find a deep layer where its energy corresponds to the resonance energy. Figure 2.1 shows a thick target with a thickness corresponding to several multiples of the resonance width. The yield of a thick target also represents this fact. It initially increases with increasing beam energy over and above the resonance energy and finally reaches a plateau in the yield where the beam energy loss is such that the particle always find a depth where its energy is equal to the resonance energy. Figure 2.2 shows a typical thick target yield curve. The location of the resonance energy E_R in this curve corresponds to the position where the yield has half of its maximum value. The width of the resonance Γ can also be extracted from the yield curve. The resonance width is equal to the energy interval where yield has dropped from 75% of its maximum value to 25% [6,7].

Thick target yield data can be fitted with a function given by [8],

$$Y \propto \tan^{-1}\left[\frac{E - E_R}{\Gamma/2}\right] + \frac{\pi}{2}$$

The important resonance parameters like E_R and Γ can be extracted from the data.

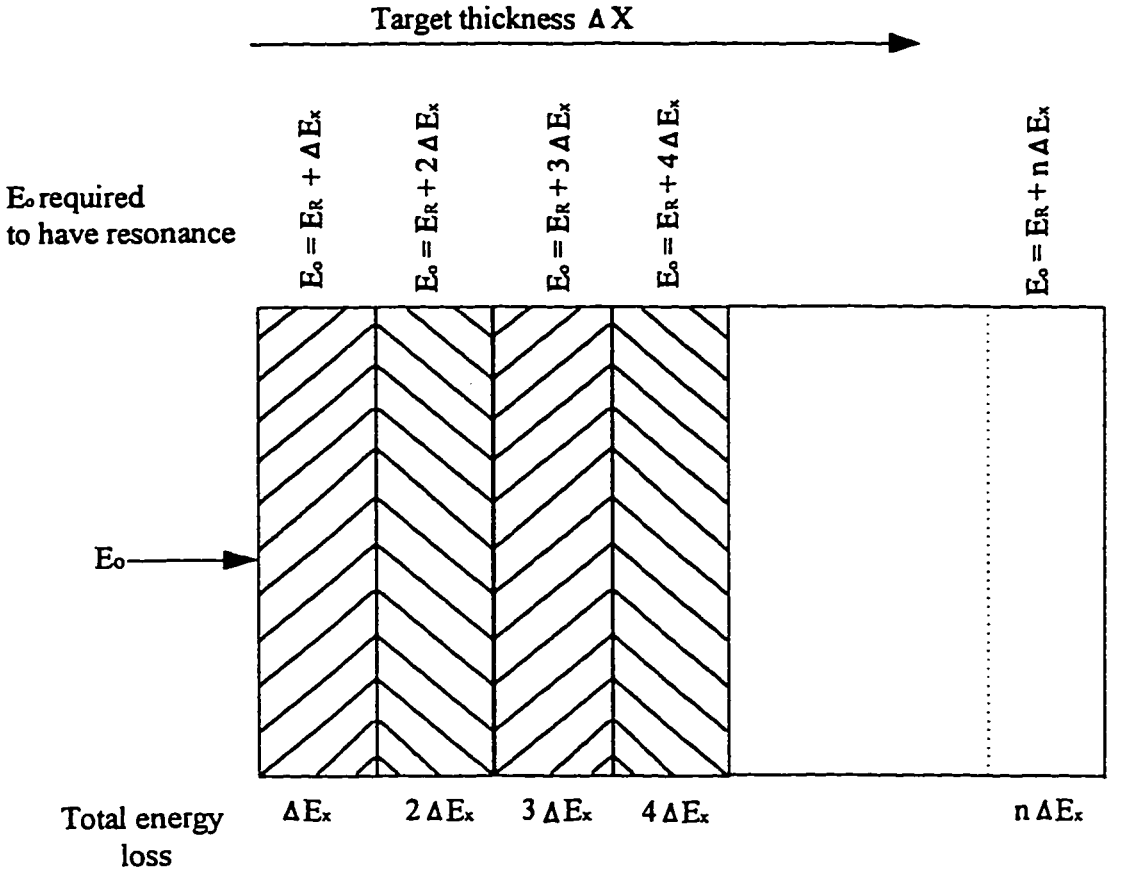

Figure 2.1 Thick target with multiple resonance widths.

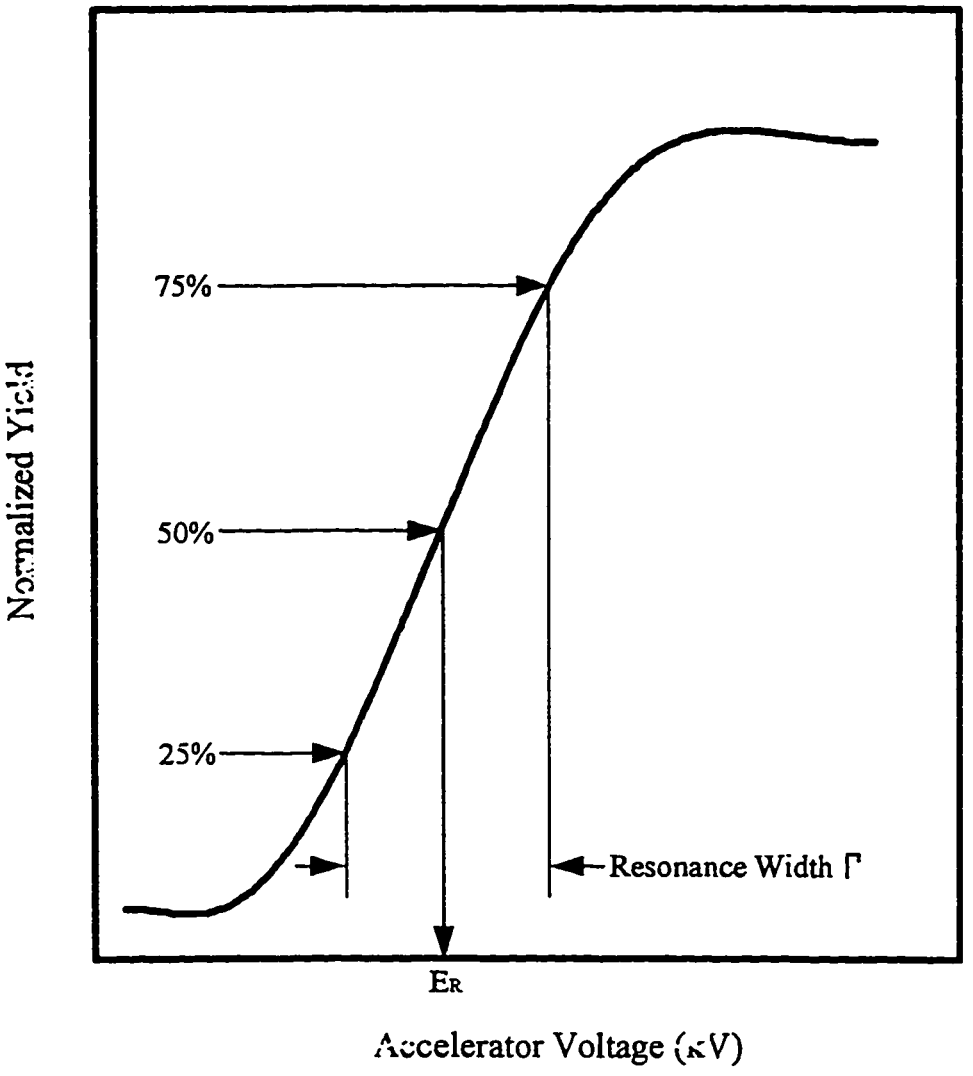

Figure 2.2 Typical thick target curve.

2.1.2 $^{19}F(p, \alpha\gamma)^{16}O$ resonance reaction for accelerator energy calibration

The $^{19}F(p, \alpha\gamma)^{16}O$ resonance reaction is commonly used for accelerator energy calibration. The reaction proceeds as following:

$$^{19}\mathrm{F} + \mathrm{p} \rightarrow \mathrm{Ne}^{20} \rightarrow {}^{16}\mathrm{O}^{*} + \alpha$$

$$\downarrow$$

$$^{16}\mathrm{O} + \gamma$$

The $^{19}F(p, \alpha\gamma)^{16}O$ reaction is studied using γ-ray detection. Since γ-rays are emitted from the excited state of ^{16}O, their energy is independent of the beam particle energies [5,9]. The $^{19}F(p, \alpha\gamma)^{16}O$ reaction has several resonances out of which two resonances at 223.99±0.07 keV and 340.46±0.04 keV are used for accelerator energy calibration [10]. The cross section of the 224 keV resonance of the $^{19}F(p, \alpha\gamma)^{16}O$ reaction is about 0.2 mb. For 340 keV resonance energy, the cross section is 160 mb which is 800 times higher than that for 224 keV resonance energy [3]. The 224 keV and 340 keV resonances of the $^{19}F(p, \alpha\gamma)^{16}O$ reaction were used to calibrate the 350 kV accelerator. In the following, the 350 kV accelerator is described briefly.

2.2 350 kV ACCELERATOR FACILITY

The KFUPM 350 kV accelerator is a high current Cockcroft-Walton type electrostatic accelerator. Its details are published elsewhere [11]. The accelerator has three ion sources. An atomic beam polarized-ion source and two duoplasmatron ion

sources. One of the two duoplasmatron sources, model 740, is a high current ion source with a maximum current of 25 mA, while model 820 is a low current ion source. In this study, the low current ion source which can deliver upto a maximum of 5 mA current, was used.

A general layout of the accelerator system is shown in Figure 2.3. The accelerator has three beam lines at 0°, 45° and 80°. The 0° and 45° beam lines are used for experiments using neutrons while the 80° beam line is dedicated for charged particle spectroscopy experiments. The accelerator assembly is situated inside a hall with thick shielding walls such that the neutron and γ-radiation dose outside the hall is reduced below the permissible limit. The accelerator's control console and a micro-VAX based data acquisition system for data analysis are located in a room outside the accelerator hall. A scattering chamber is located at the end of the 80° beam line. The details of the scattering chamber can be found elsewhere [12]. Signals from the scattering chamber are transported to the control room through a pair of patch panels located in the data control room and the accelerator hall.

The energy of the 350 kV ion accelerator was calibrated using nuclear reactions. Voltage from a regulated 350 kV power supply is applied across the accelerator tube of the accelerator. It is this which provides the net energy gain of a charged particle during its passage through the accelerator tube. A resistor gradient column connected parallel to the five segments of the accelerator tube maintains equal voltage across each segment. The voltage across the accelerator tube is read out on a digital display at the central console of the 350 kV accelerator. For experimental

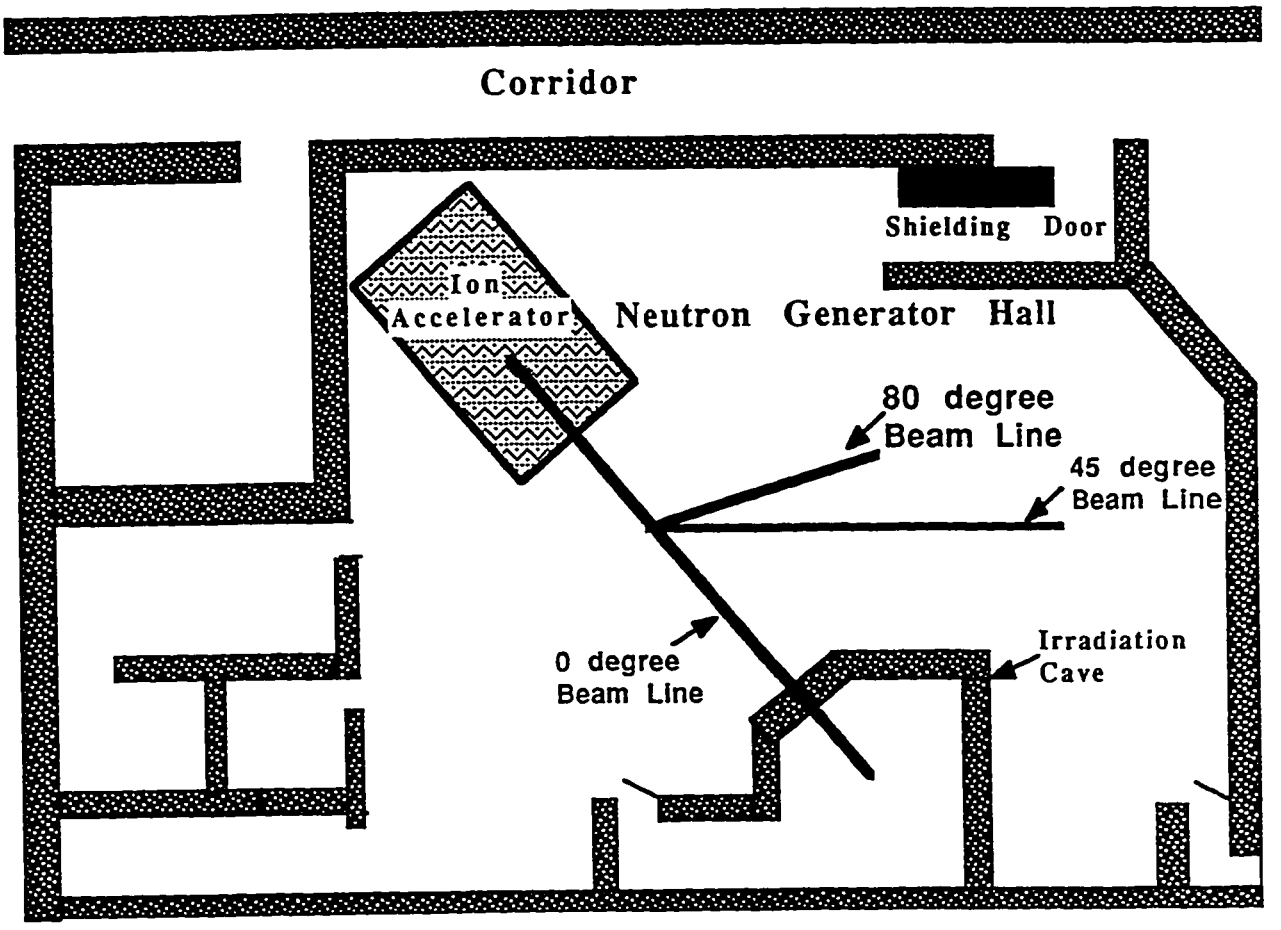

Figure 2.3 Layout of 350 kV ion accelerator system at ERL, KFUPM.

purposes, this readout is taken as the beam energy. Therefore this readout has to be calibrated against particle energies using nuclear reactions.

2.3 ERL 350 kV ACCELERATOR ENERGY CALIBRATION

The energy calibration of the KFUPM 350 kV accelerator was carried out using the $^{19}F(p, \alpha\gamma)^{16}O$ resonance reaction. The reaction was studied at 224 keV and 340 keV proton energies. Details of the experiment and the data analysis are given below.

2.3.1 Experimental set-up

Accelerator energy calibration measurements were carried out at the 80° beam line scattering chamber. The chamber initially designed for charged particle spectroscopy was modified to accommodate a NaI detector. The chamber modification to accommodate a NaI detector was achieved by using an adapter flange at one of the scattering chamber ports. The flange which is shown in Figure 2.4 allowed to place a NaI detector 5 mm away from the target. The target was mounted at the center of the table of the scattering chamber with a 45° inclination with respect to the beam axis so that the NaI detector can see the maximum area of the target. Since the target backing was thick and the beam could not pass through it, the incident beam current was measured at the target. This was achieved by mounting the target on an electrically isolated holder and measuring the current at the target.

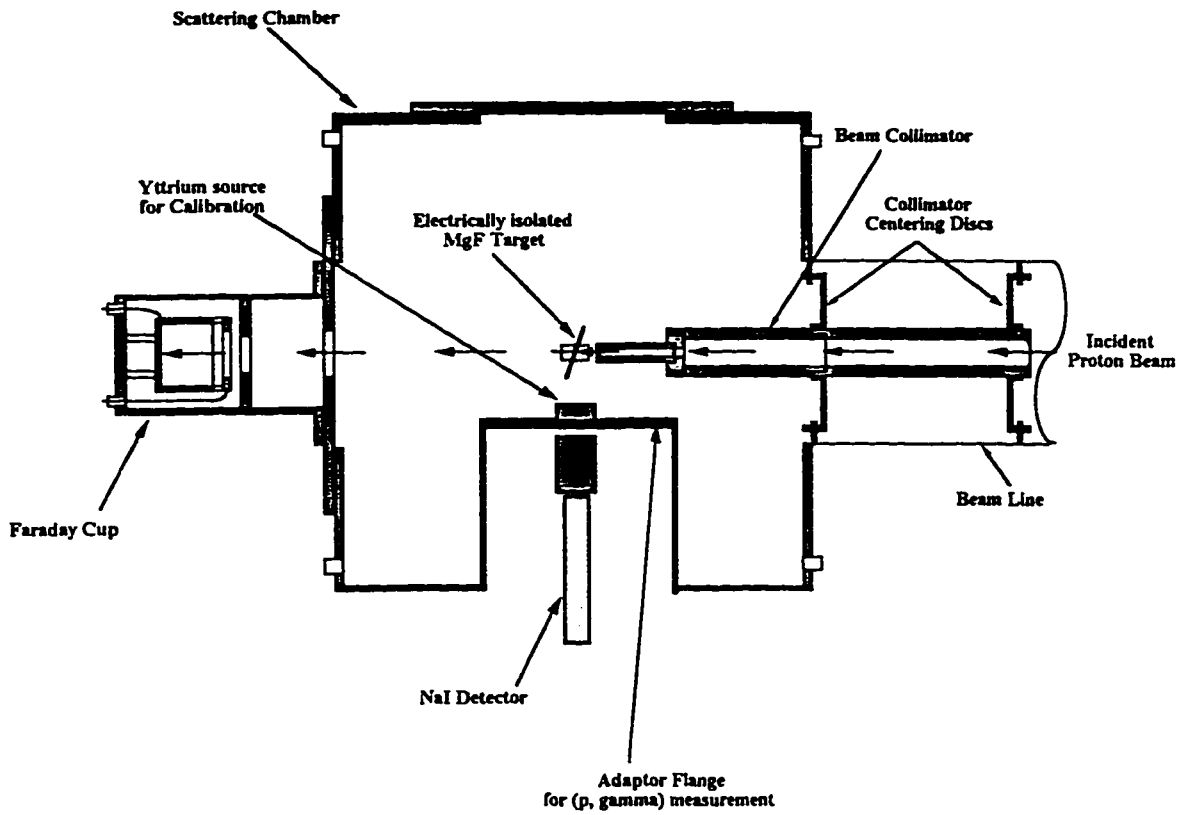

Figure 2.4 Experimental set up for $^{19}F(p, \alpha\gamma)^{16}O$ reaction.

2.3.2 Fluorine target

The ^{19}F targets were prepared by depositing 48-450 $\mu g/cm^2$ thick layer of MgF_2 on 0.5 mm thick Tantalum backings. Fluorine (F_2) contains 100% ^{19}F. The targets were prepared in the target laboratory of KFUPM Laser Research Laboratories.

2.3.3 NaI Detector

In this study, 7.12 MeV γ-rays from the $^{19}F(p, \alpha\gamma)^{16}O$ reaction were detected by a 3" × 3" (diameter × thickness) NaI(Tl) detector. The detector was coupled to a RCA 4900A photomultiplier tube using a positive HV photomultiplier base. The detector was operated at 1000 V positive bias voltage. A typical detector pulse height spectrum for ^{137}Cs source is shown in Figure 2.5. The energy resolution of the detector for 662 keV γ-rays from the ^{137}Cs spectrum with amplifier shaping time of 0.5 μsec was measured to be 6.4 %.

2.3.4 Electronics and data acquisition system

The electronics used in accelerator calibration measurements is shown in Figure 2.6. The bias voltage to the NaI detector was supplied by a HV power supply. The energy signal from the detector was fed to a preamplifier and then through a patch panel it was lead to a spectroscopy amplifier. Finally, the output of the amplifier was connected to an ADC which was hooked to a micro-VAX based data acquisition system. The data was acquired from one detector only. The data acquisition code for one detector was written using the XSYS software. It mainly consist of one data acquisition process (DAP) file and one data analysis (EVL) file which allows to process

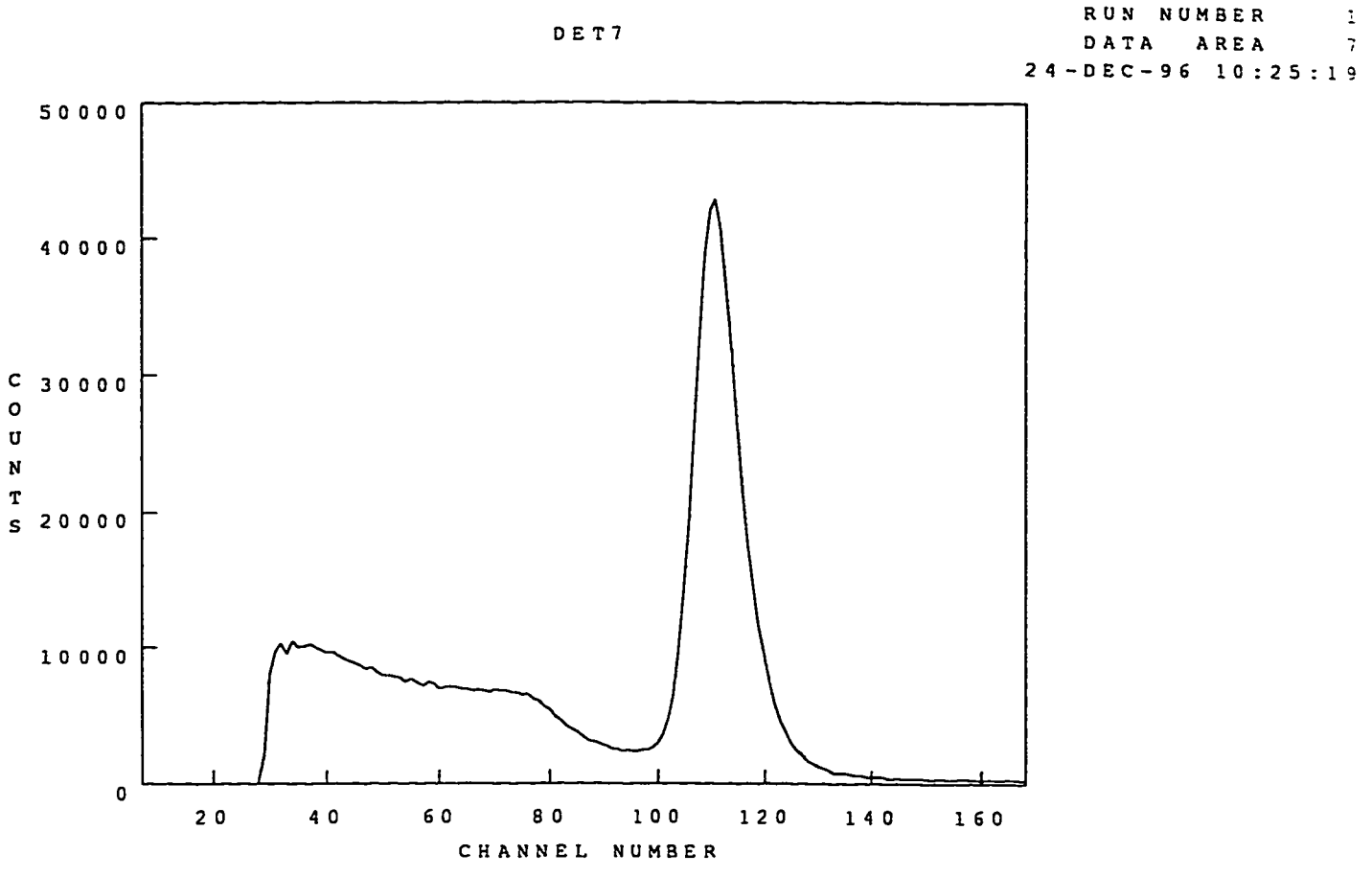

Figure 2.5 Typical energy spectrum of the NaI detector for ^{137}Cs.

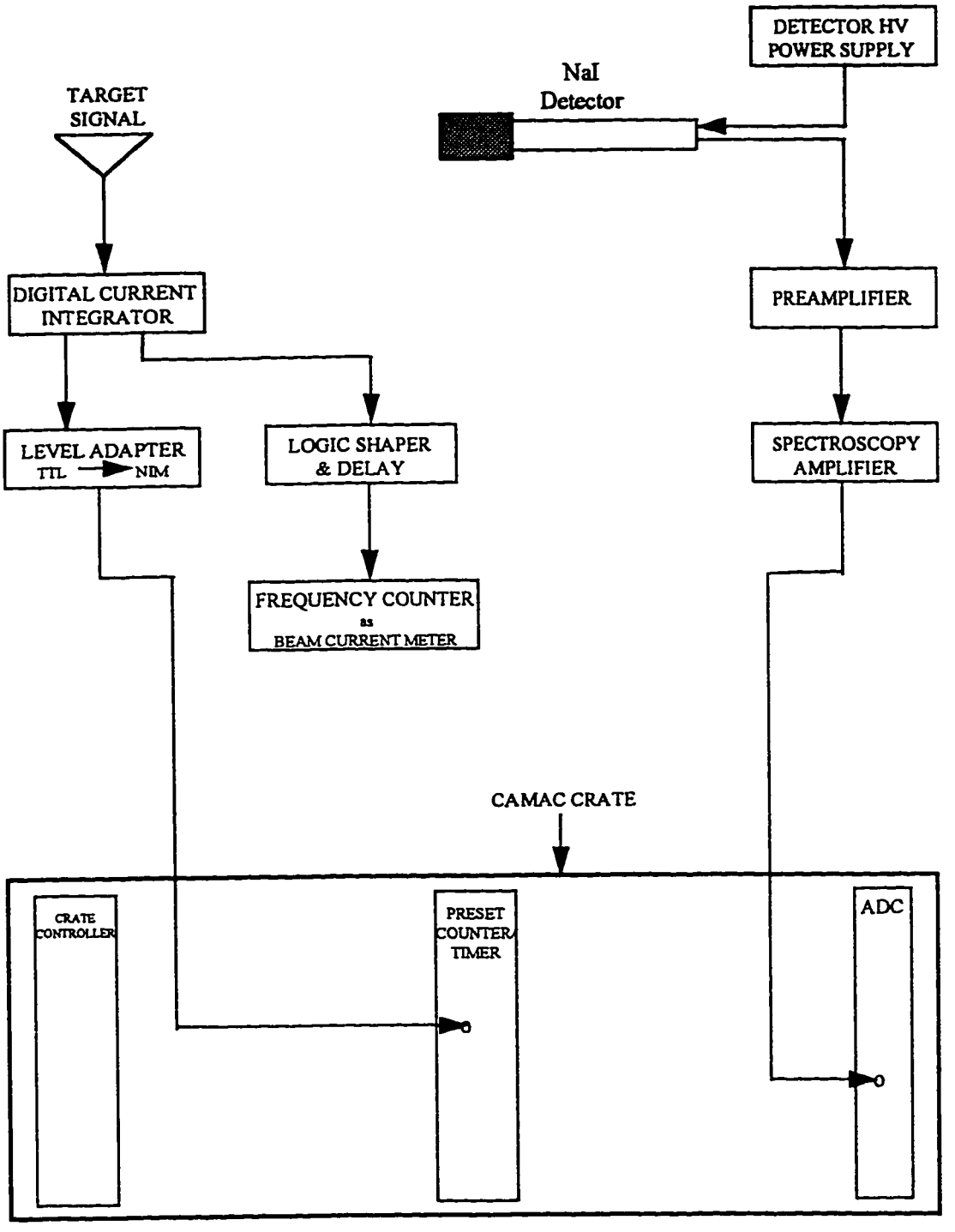

Figure 2.6 Electronics and data acquisition system for the energy calibration of the accelerator.

the ADC signal. The details of these files are given under the description of "MDET" code in section 3.7.

The calibration data was acquired for a fixed amount of charge collected at the target. For this purpose, the charge signal from the target was digitized by a Digital Current Integrator (DCI) into pulses. DCI pulses were converted into NIM signal by a LeCroy level adapter and finally fed into a Borer CAMAC preset counter/timer to control the data acquisition process.

2.3.5 Pulse height calibration of the NaI detector

In order to identify the γ peaks, the detector was calibrated using 0.898 MeV and 1.836 MeV γ-rays from ^{88}Y. The Yttrium source was mounted on the adapter flange inside the scattering chamber. The NaI detector was placed externally in the adapter flange. The NaI detector pulse height spectrum was taken using the electronics shown in Figure 2.6. A typical pulse height spectrum of ^{88}Y γ-rays with the two γ-ray peaks and the sum peak corresponding to an energy of 2.734 MeV is shown in Figure 2.7. Finally the channel number corresponding to the three peaks with 0.898 MeV, 1.836 MeV and 2.734 MeV (sum peak) energies were plotted as a function of γ-ray energy to obtain the calibration curve. Figure 2.8 shows the pulse height calibration curve of the NaI detector. The slope of the line, i.e. energy per channel, was found to be 8.7 keV/channel.

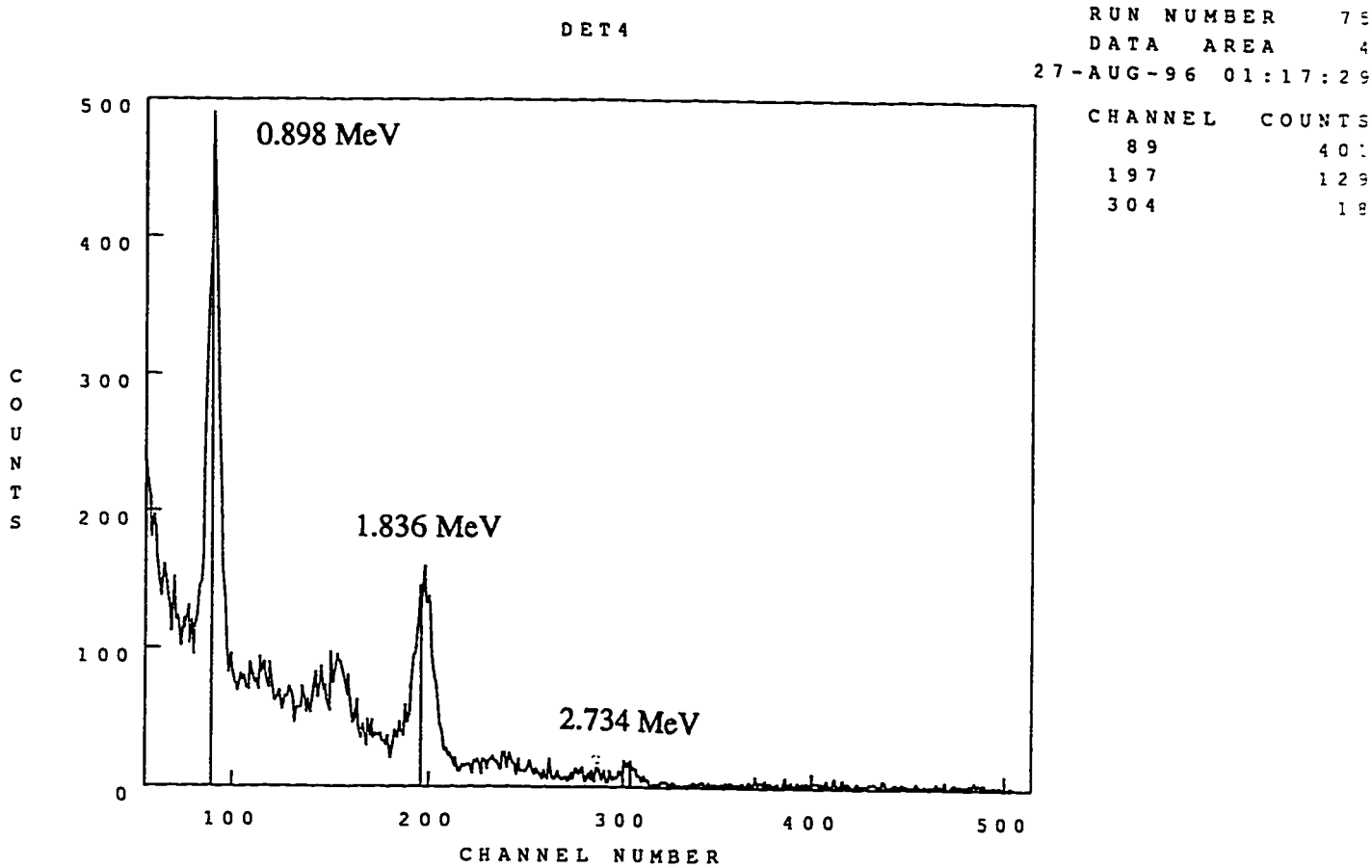

Figure 2.7 Calibration of NaI detector using ^{88}Y source.

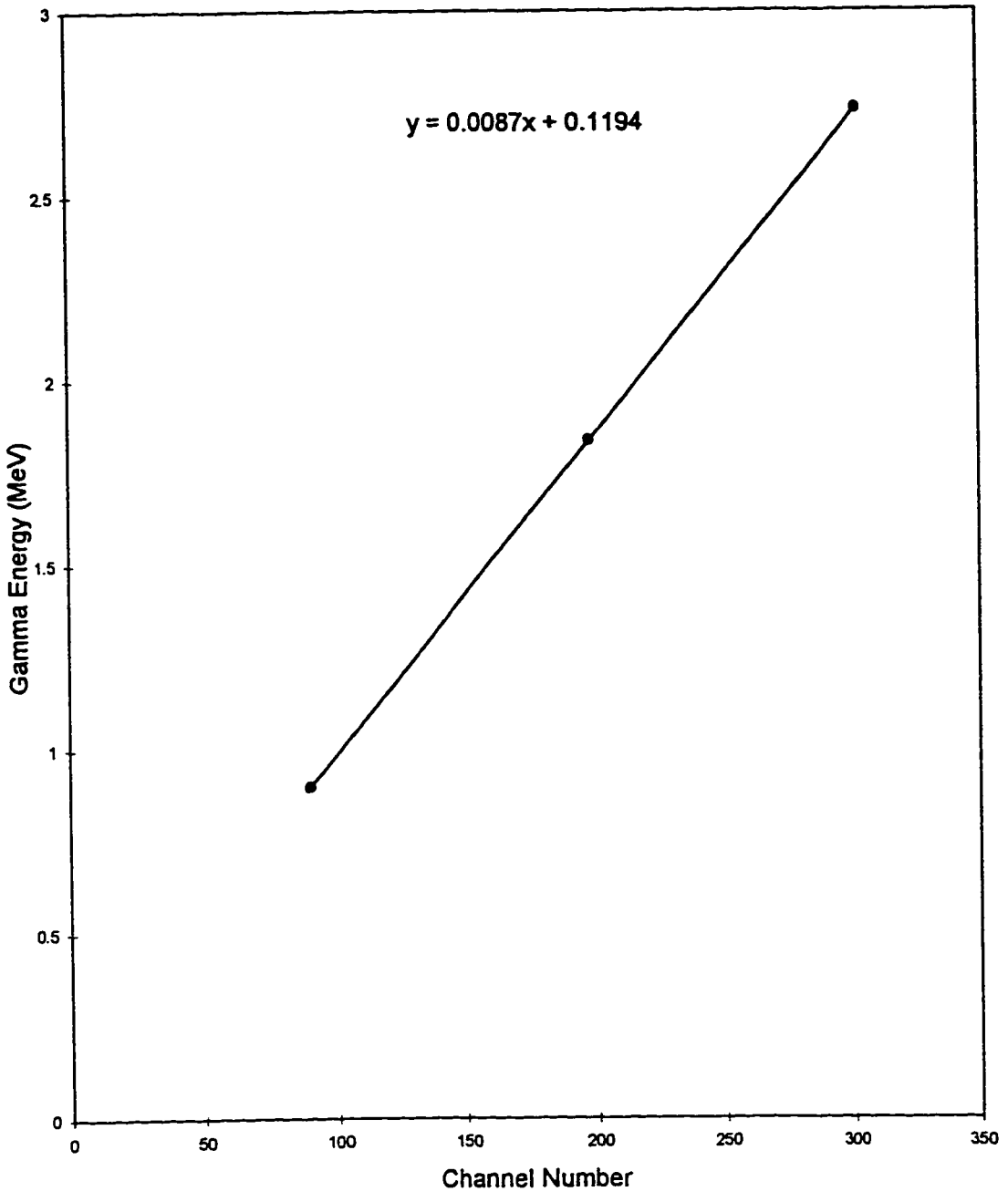

Figure 2.8 Pulse height calibration curve of NaI detector.

2.3.6 Excitation function measurement for $^{19}F(p, \alpha\gamma)^{16}O$ reaction

For accelerator energy calibration, the excitation functions of $^{19}F(p, \alpha\gamma)^{16}O$ reaction were measured at 90° for 224 keV and 340 keV resonance energies. For the 224 keV resonance energy, the accelerator voltage was varied from 216-232 kV in 2 kV steps so that the 224 keV resonance energy is well inside this range of accelerator voltage. The beam spot was chosen to be 2 mm on the target and the average beam current was 2.4 μA. Yield of γ-ray at each energy of accelerator voltage was taken for a fixed preset of 1 mC charge collected on the target. Duration of each run was almost eight minutes.

Cross section of 340 keV resonance is about 800 times higher than the 224 keV resonance accordingly the current of the incident beam was reduced by a factor of 800 to study the 340 keV resonance. On average 30-50 nA bias current was used to study the 340 keV resonance of $^{19}F(p, \alpha\gamma)^{16}O$ reaction. The beam spot was also reduced to 1 mm diameter. The accelerator voltage was varied from 325-346 kV in 2 kV steps. Each data point was taken for a preset of 5 μC collected at the target. In this case each run was completed in about three minutes. Figure 2.9 shows the γ-ray yield spectrum taken at 340 keV deuteron energy with a current of 50 nA. The spectrum shows the three peaks corresponding to 7.12 MeV γ-rays. The extreme right peak is the photo-peak of 7.12 MeV γ-rays while the remaining two peaks at the lower energy side are the single and double escape peaks of this γ-ray. The γ-ray energy corresponding to the single and double escape peaks are 6.599 and 6.098 MeV, respectively. In total 28 spectra were acquired for the two resonances.

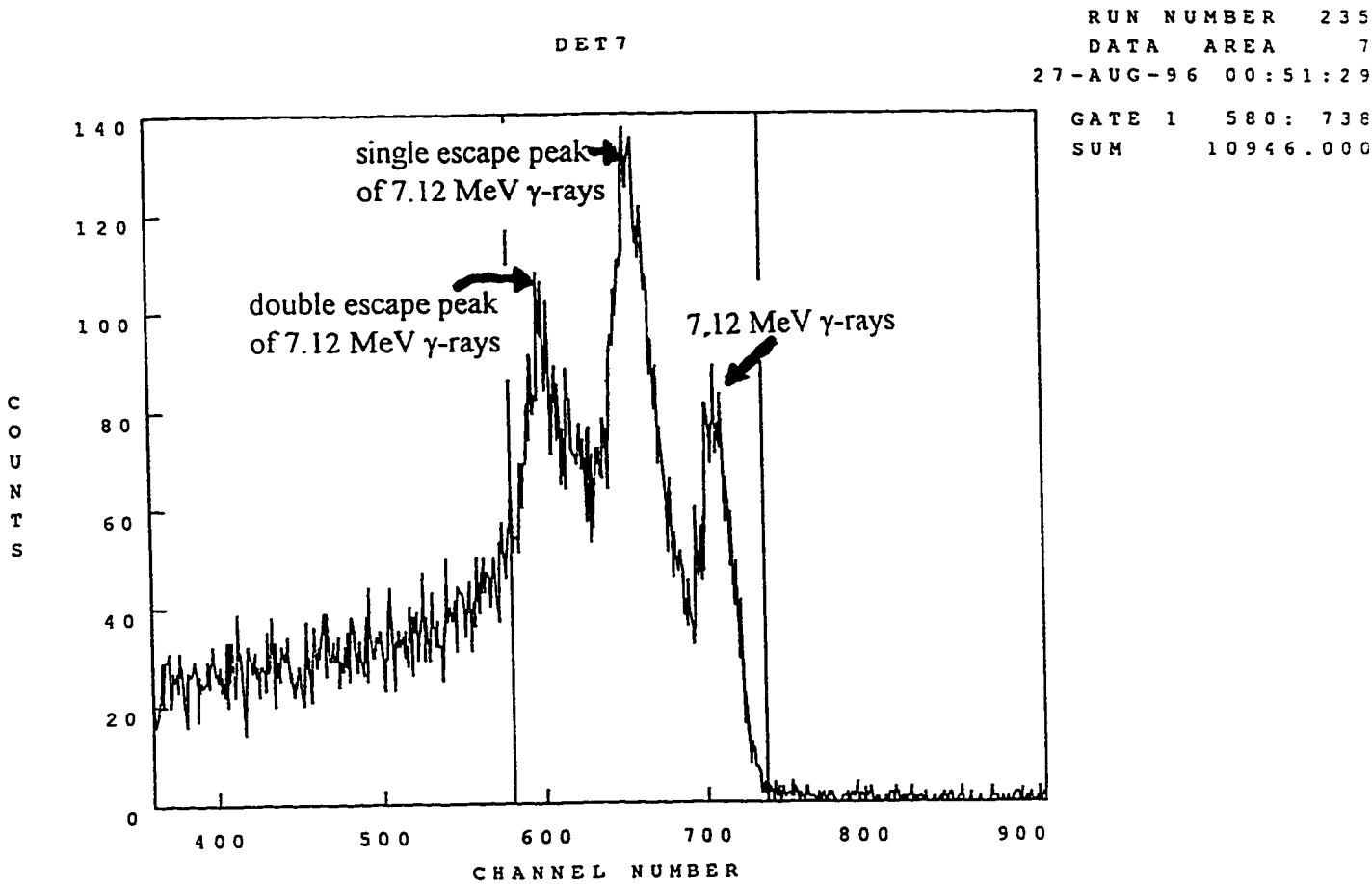

Figure 2.9 γ-ray yield spectrum of $^{19}F(p, \alpha\gamma)^{16}O$ reaction at 340 keV proton energy.

In the next step 28 spectra taken for both resonances were analyzed using OFFLINE data acquisition codes. In this step gates were set to include the photo-peak and associated single and double escape peaks. Thus integrated counts under the three peaks were obtained. Since the preset charge used for all the data points of one resonance was the same, thick target yield curve was obtained by plotting the normalized yield as a function of accelerator voltage.

Thick target yield was fitted with an arctangent function given by,

$$Y = k\left[\tan^{-1}\left(\frac{E - E_R}{\Gamma/2}\right) + \frac{\pi}{2}\right]$$

where k is the normalization constant, obtained from the plateau region of the curve. The fit was carried out using the least square method. Figure 2.10 and Figure 2.11 show the 224 keV and 340 keV resonance data respectively along with the least square fits. The fitted values of both resonance energy are listed in Table 2.2. For 224 keV and 340 keV resonances, the resonance energies are 221.5 and 334.5 keV respectively. This shows that the accelerator energy is systematically 2.5 and 5.5 keV higher than the true resonance energies.

2.3.7 Accelerator-energy calibration curve

The energy calibration curve of the 350 kV accelerator was obtained by plotting the voltage readout of the accelerator terminal as a function of proton resonance energy. Figure 2.12 shows the accelerator-energy calibration curve using two data points. The slope of this straight line is 1.0265 which shows that the proton energy is 2.65% higher than the voltage readout of the accelerator. Since only two

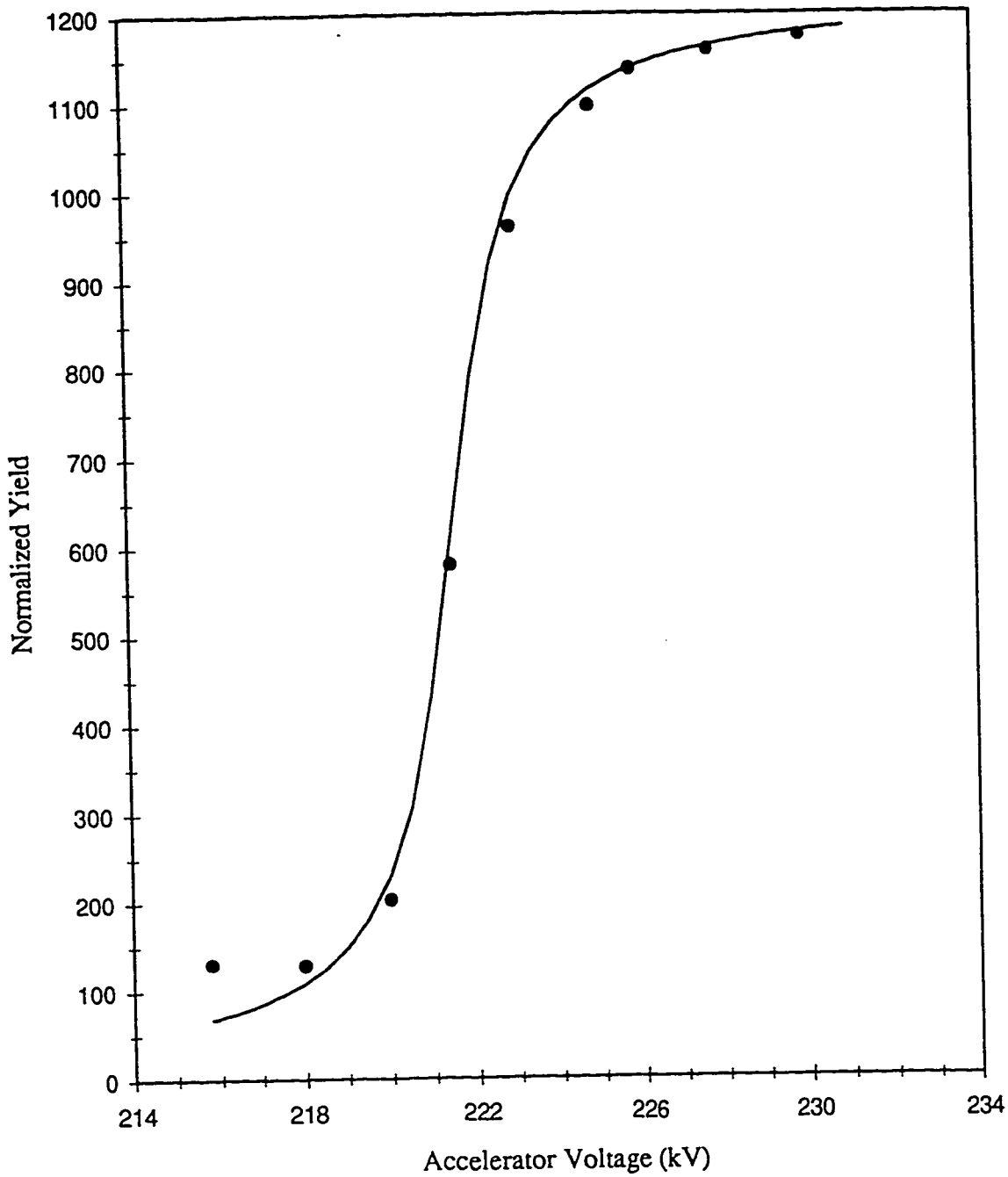

Figure 2.10 Excitation function for 224 keV resonance of $^{19}F(p, \alpha\gamma)^{16}O$ reaction.

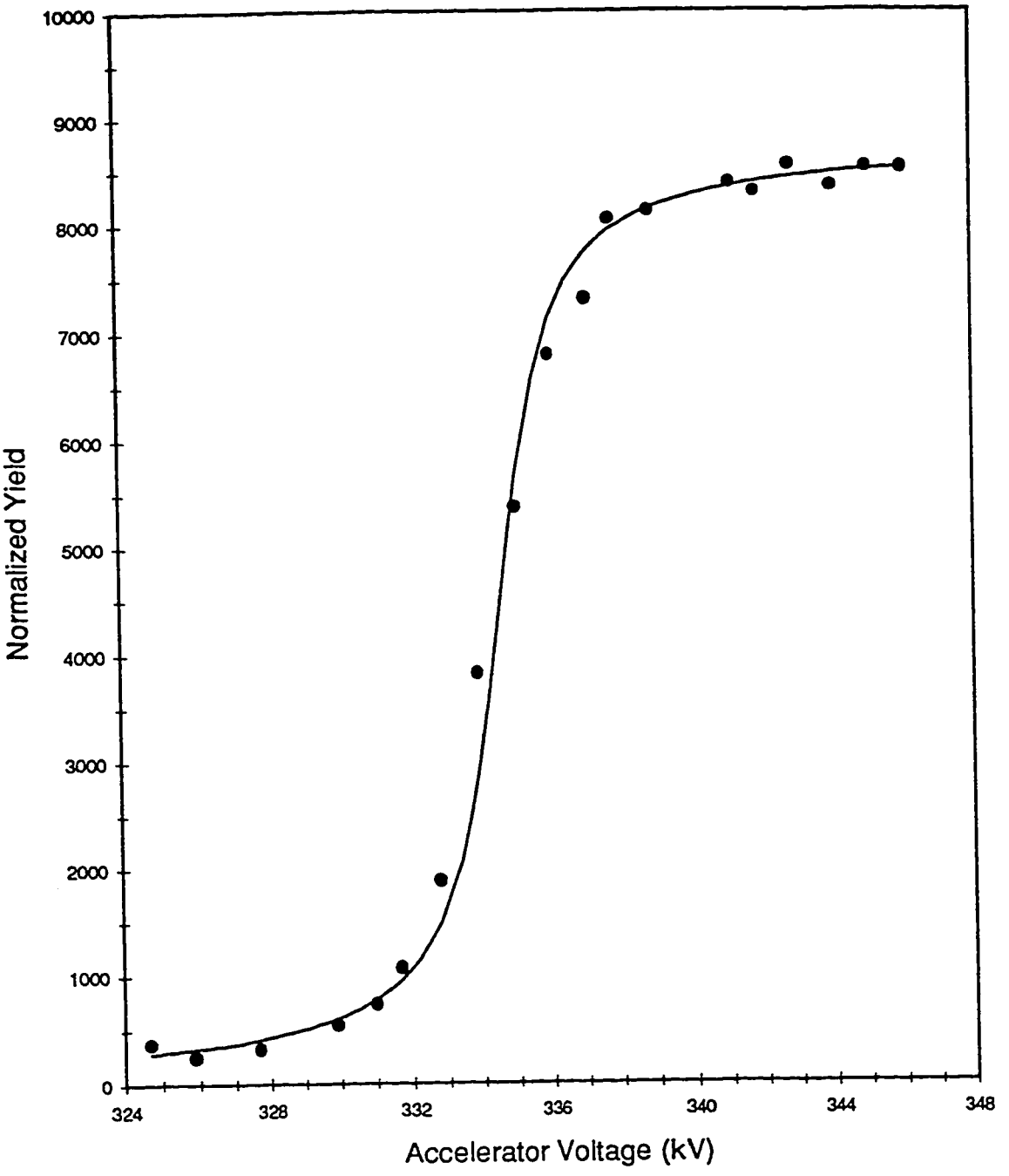

Figure 2.11 Excitation function for 340 keV resonance of $^{19}F(p, \alpha\gamma)^{16}O$ reaction.

Table 2.2 Resonance energy E_R of $^{19}F(p,\alpha\gamma)^{16}O$ reaction.

Published E_R (keV) [9]	Experimental E_R (keV)
223.99±0.07	221.5±5
340.46±0.04	334.5±7

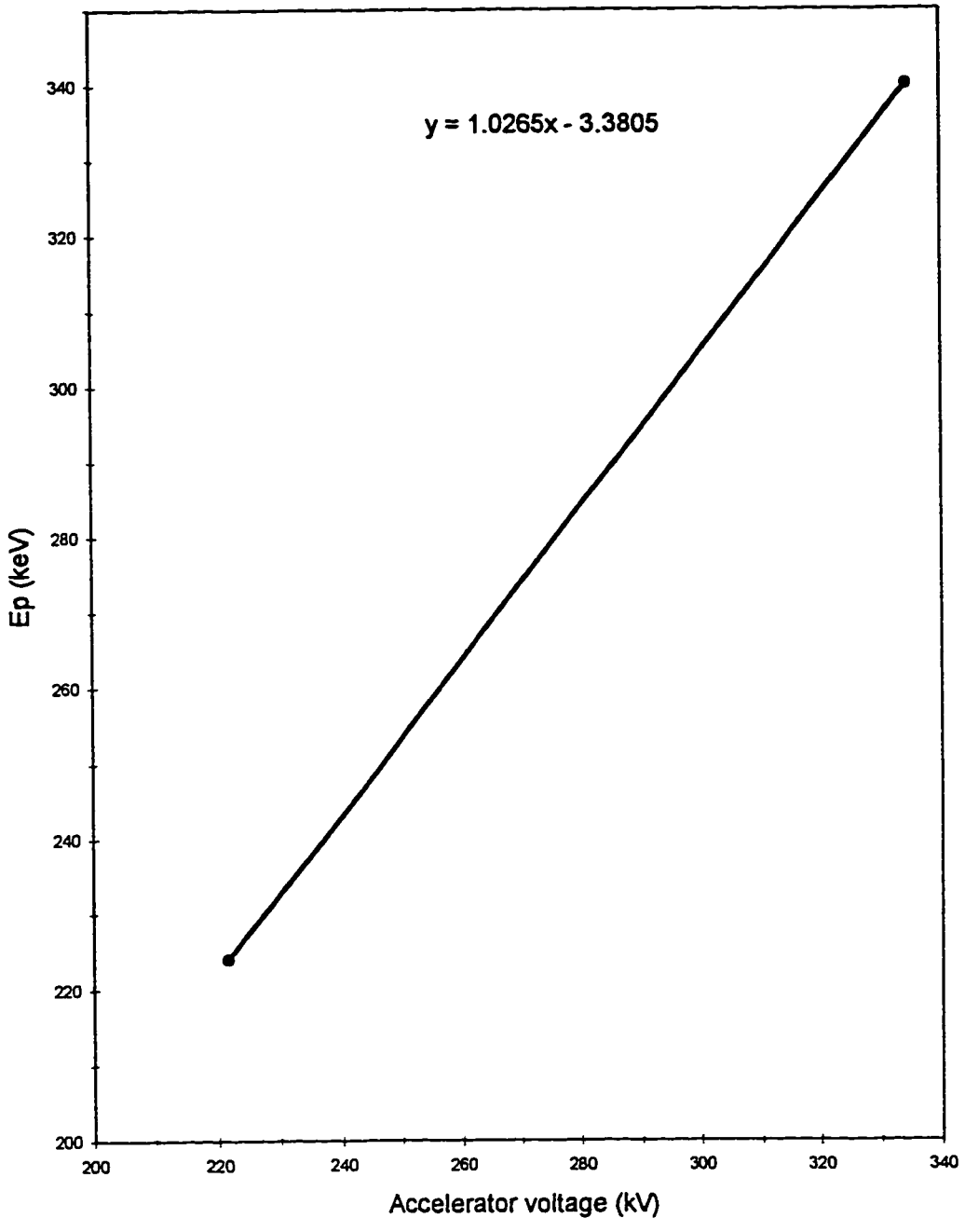

Figure 2.12 Energy calibration curve of ERL 350 kV accelerator.

resonances of $^{19}F(p, \alpha\gamma)^{16}O$ reaction were studied, more energy calibration data points at low energy resonance reactions are yet to be studied. Some of these reactions were mentioned earlier in Table 2.1.

CHAPTER 3

EXCITATION FUNCTIONS AND ANGULAR DISTRIBUTIONS MEASUREMENTS OF $^{13}C(d, p)^{14}C$

The excitation functions and the angular distributions measurements of the $^{13}C(d, p)^{14}C$ reaction were carried out at the KFUPM 350 kV accelerator laboratory. The deuteron beam energy was varied from 200-350 keV with a typical dc beam having 1-5 μA current.

3.1 EXPERIMENTAL SET-UP

The $^{13}C(d, p)^{14}C$ reaction study was carried out utilizing scattering chamber of 80° beam line of ERL 350 kV accelerator [12]. For the sake of continuity a brief description of the chamber will be given here. The chamber consists of an angle calibrated table, target holder, detector holders and a beam collimator. The beam is collimated at the target through a collimator. The beam transmitted through the target is measured at a Faraday cup located behind the target. One of the four ports of the scattering chamber is used for pumping the chamber with a rotary pump.

The detector holders can slide in a circular groove in the table to any desired angle. The detector holders consist of two parts, a vertical stand and a horizontal cylindrical collimator with pumping slots. The detector is placed behind the

holder's collimator. Two circular discs separated by 40 mm and screwed to the front and back of the collimator cylinder, are used to define the detector solid angle. In the present study front and back apertures of the collimator were chosen to be 3 and 5 mm respectively. This resulted in an effective detector solid angle of 1.25 m.sr subtended at the target. The target foil was lifted on a frame which slides inside a holder fixed to the target-holder support at the center of the table. Beam is focused on the target to a 2 mm diameter spot using the beam collimator.

3.2 MULTI-DETECTOR SET-UP

The original setup for the angular distribution measurements consist of four detectors and required four runs to cover the thirteen angles for a given angular distribution. In order to minimize the number of runs and hence the beam time, four more detectors were added. In this way the beam time was reduced by a factor of 2 and eight angles were covered simultaneously. The addition of four more detectors required a new data acquisition code which should be capable to handle the data from the eight detectors simultaneously. A new target holder was designed and was placed at 45° with respect to the beam to cover eight angles in a single run. Newly constructed detector holders were aligned using optical and as well as nuclear technique. In the following these both techniques are described briefly.

3.2.1 Detector holders' alignments using a telescope

The alignment of the detectors is an important and basic task for the measurement of a reaction yield. Initially the detector collimators were optically aligned

one by one with respect to beam collimator axis using a telescope whose axis was aligned with respect to the beam axis. For this purpose 1-mm-diameter aperture was inserted at the front end of the beam collimator and then the telescope was aligned with respect to the aperture hole and the external wall of the collimator cylinder. Once the telescope was aligned, it was used to align the detector holders. Every detector holder was placed first at 180° and the back and the front aperture of the holder's collimator were aligned with respect to the telescope axis. Then the detector holder was moved to 0° and again the front and back aperture of the holder's collimator were aligned with respect to the telescope axis. Any adjustment in the alignment was carried out using the adjusting screws of the detector's collimator and the three support screws of the angle calibrated table.

Once the alignment of the detector holders were done at 0° and 180°, they were checked randomly at other angles by assuming that the point of intersection of lines from the four pairs of detector-holders, placed diagonally opposite, should be at the center of the angle calibrated table. Thin threads were pulled through each pair. Figure 3.1 shows this set-up. It was observed that the point of intersection of these four strings was at the center of the target. This was checked also by looking through the telescope as well from the top of the chamber.

3.2.2 Detector holders' alignments using nuclear reaction

For a nuclear reaction induced by the unpolarized beam, the reaction yield at a lab. angle $+\theta$ is equal to that at $-\theta$. Therefore a pair of aligned identical detectors with the same solid angle placed at $\pm\theta$ angles will register the same reaction

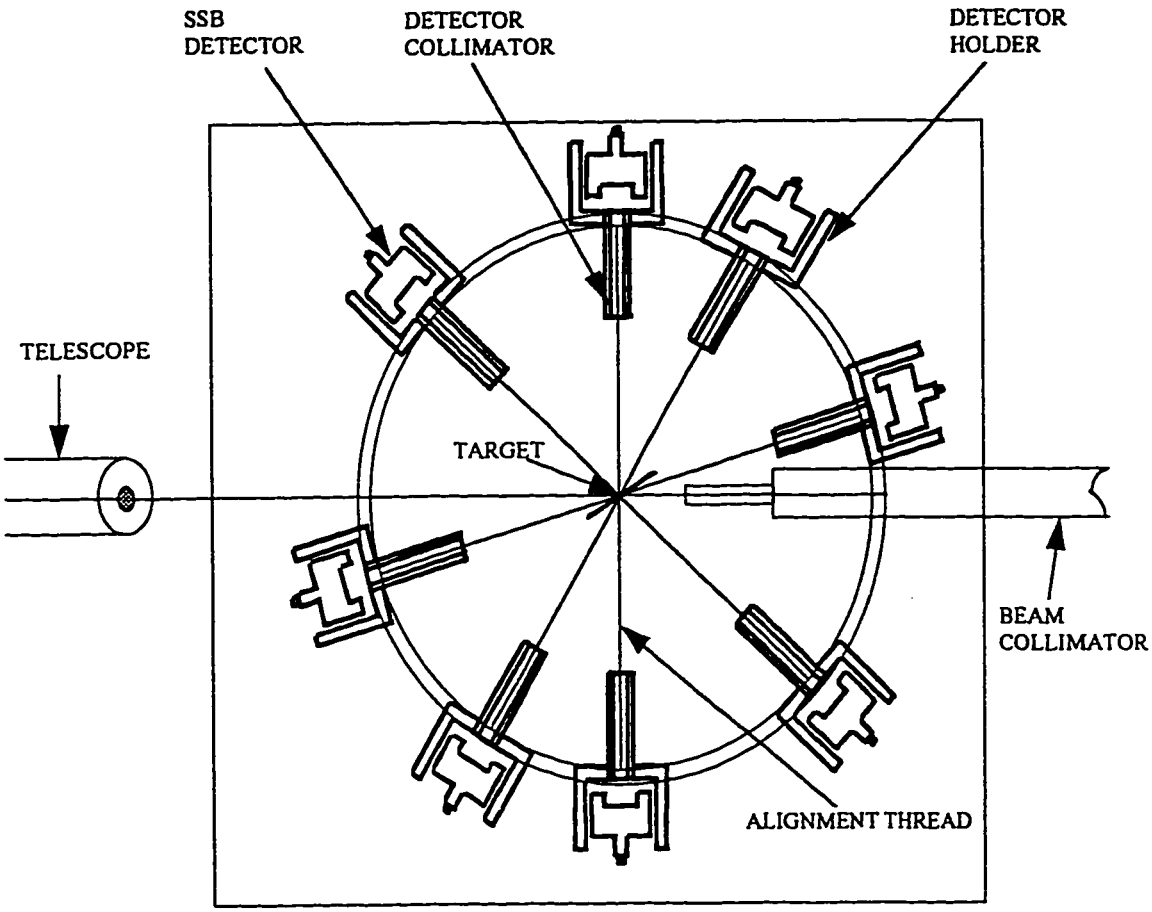

Figure 3.1 Alignment check of detector holders.

yield within the statistical uncertainties. On the other hand this fact can be used to check the alignment of the detectors.

The alignment of the eight detector holder was checked by comparing the reaction products' yield of four pairs of the detectors placed at ±30°, ±60°, ±120° and ±150°. The yield of $^{13}C(d, p)^{14}C$ reaction was studied at 325 keV. The data was acquired for the eight detectors for a period of 40 minutes using a typical beam current of 0.2 μA. In this study ^{13}C target with a typical thickness of 30 $\mu g/cm^2$ was used. Figure 3.2 shows the typical spectrum taken with +30° detector. Figure 3.3 shows the yield of the four pairs of detectors plotted together. The yield of both detectors of all the pairs agree with each other within the statistical uncertainties.

3.3 ^{13}C TARGETS

In this experiment 100% enriched ^{13}C target foils were used which were supplied by the Atomic Energy of Canada Limited, Chalkriver, Canada. In order to choose the thickness of the target foil, a compromise between the energy loss of the projectile and the ejectile and the rigidity of the target has to be achieved. The foils were thin and the deuterons and the reaction protons from $^{13}C(d, p)^{14}C$ reaction suffered only a few keV energy loss. Also the foils were rigid enough to support themselves on the frame and be safe against any mechanical shock.

In order to determine the optimum thickness of the foil, the energy loss of 100-350 keV deuterons in the ^{13}C foil was calculated using the energy loss code "Babel". Figure 3.4 shows the energy loss of deuterons in the ^{13}C foils with a maxima around 200 keV deuteron energy. For 200-350 keV deuterons, energy loss in ^{13}C foil

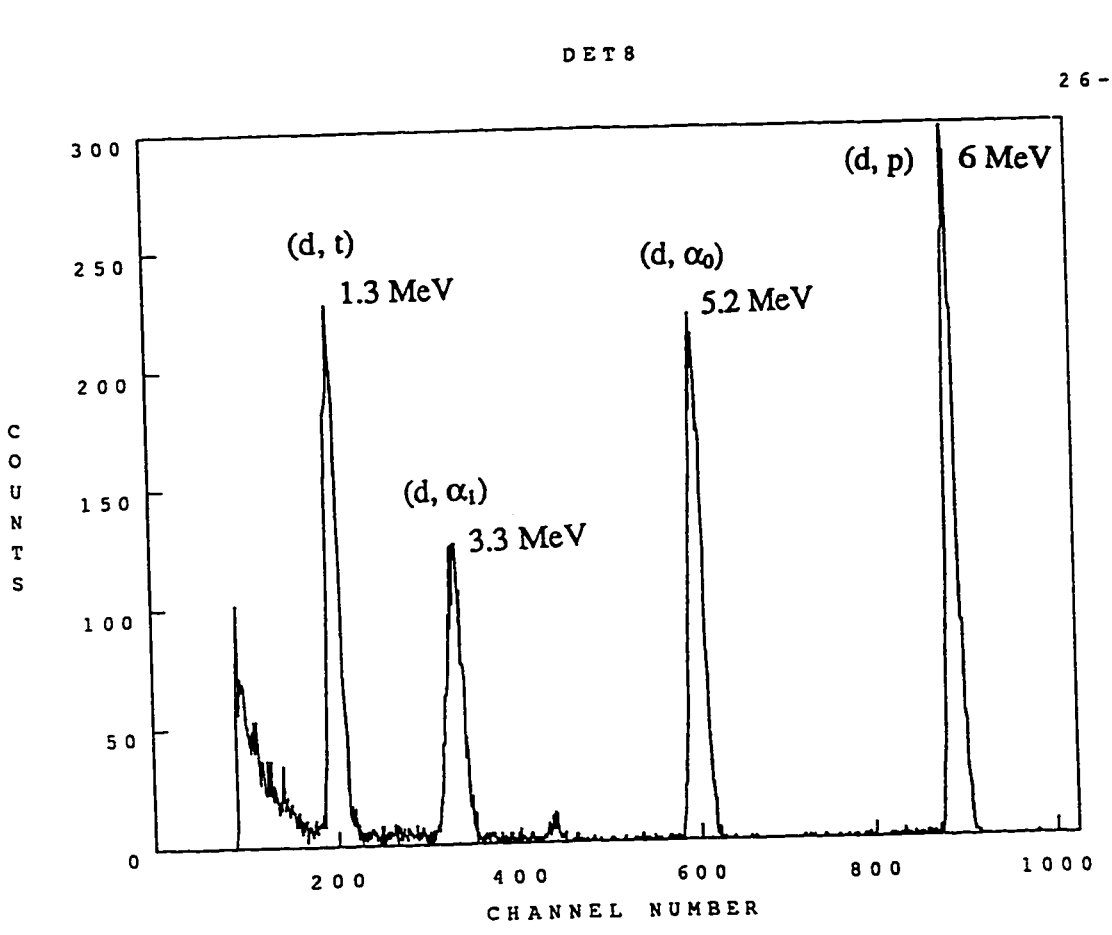

Figure 3.2 Typical spectrum of $^{13}C(d, p)^{14}C$ reaction yield at +30° detector.

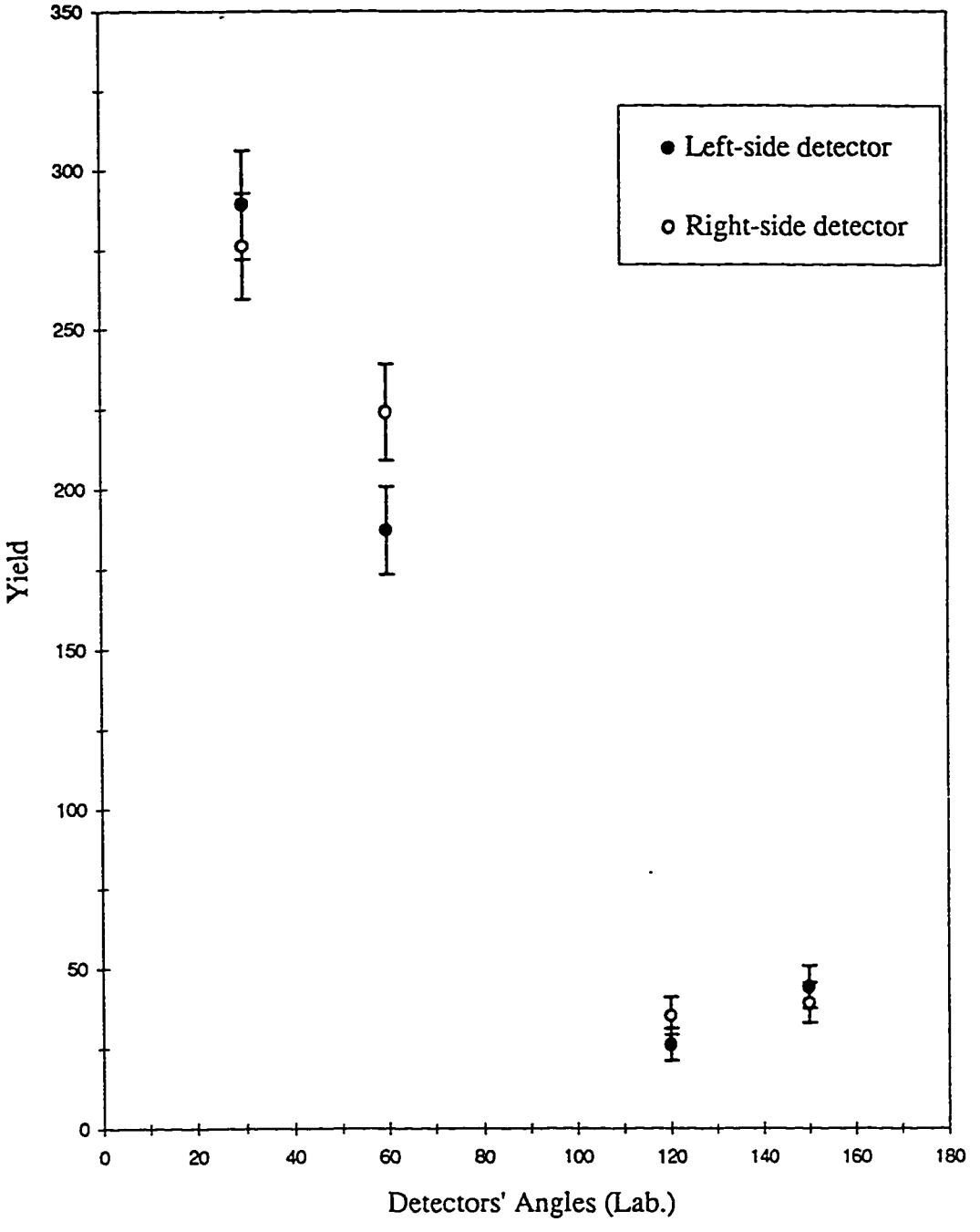

Figure 3.3 $^{13}C(d, p)^{14}C$ reaction yield for the four pairs of detectors.

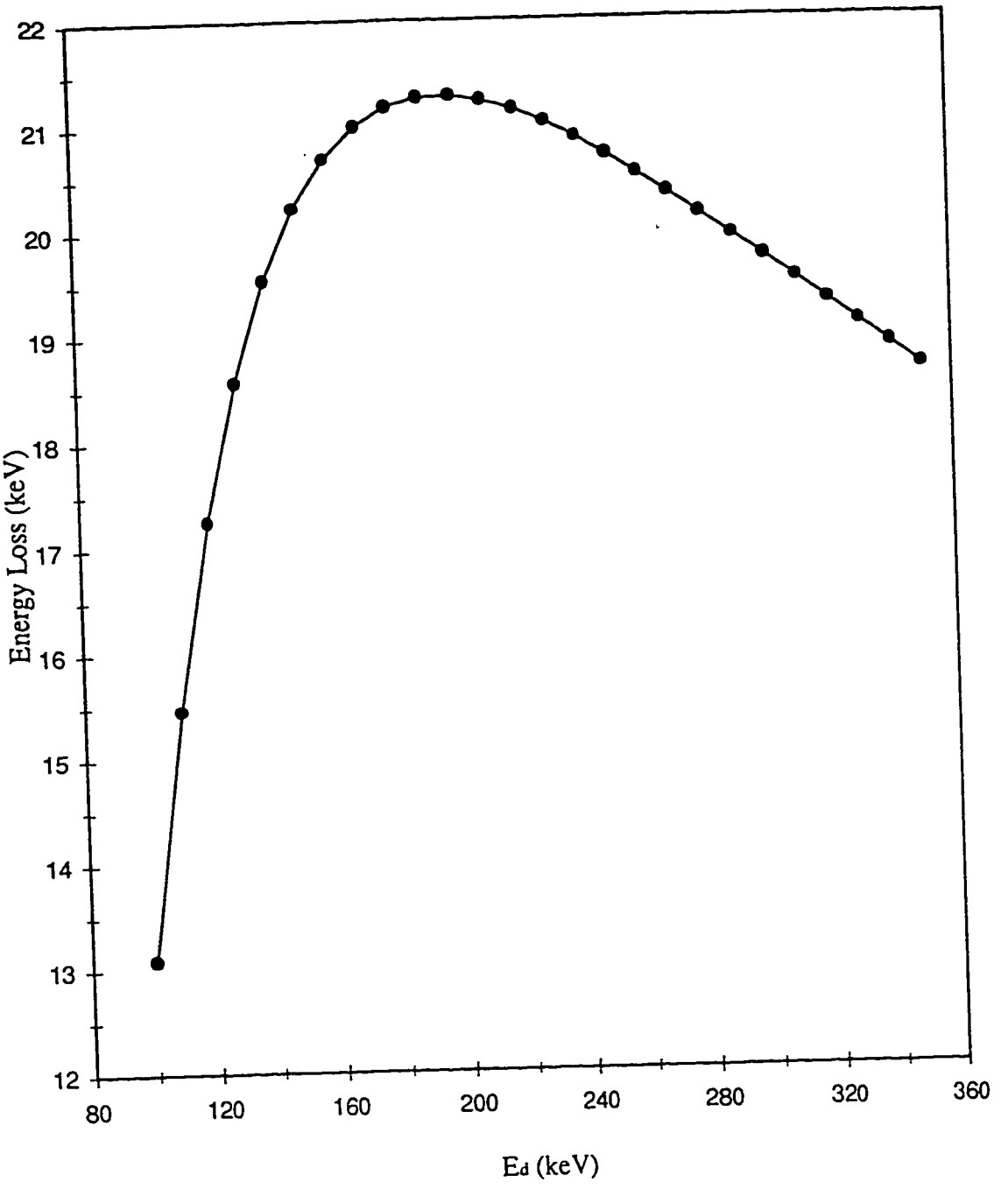

Figure 3.4 Energy loss of deuterons in ^{13}C target foil.

varies from 21.3 keV to 18.9 keV. The energy loss of protons from $^{13}C(d, p)^{14}C$ reaction in 30 $\mu g/cm^2$ ^{13}C foil was calculated using the same code. In order to determine the range of proton energy for the energy loss calculations, the minimum and the maximum energies of the protons emitted in the $^{13}C(d, p)^{14}C$ reaction with 200-350 keV deuteron energies were calculated. These calculations were carried out using reaction kinematics code "Rkin" for proton energies at 0°-180° angles. The minimum and maximum energies of protons for the $^{13}C(d, p)^{14}C$ reaction with 200 keV deuterons varies from 5.5-5.9 MeV while for 350 keV deuterons it varies from 5.6-6.1 MeV. Therefore, in the calculation of energy loss of protons in ^{13}C foils, 5.5-6.5 MeV energy range was considered. Figure 3.5 shows a loss of about 2 keV energy for the 6 MeV protons in the target. Since the ^{13}C target foils were fragile, special care had to be taken in mounting them on the frame. They were first floated on water and were then lifted very carefully on the target frame. A target thickness less than 30 $\mu g/cm^2$ would have been very difficult to float and lift. On the other hand, a thickness greater than 30 $\mu g/cm^2$ would cause considerable energy loss of the particles inside the target. Therefore it was decided to choose 30 $\mu g/cm^2$ thick ^{13}C foils.

3.4 SILICON SURFACE BARRIER DETECTORS

Silicon surface barrier detectors have an excellent energy resolution for charged particles and are widely used for charged particles spectroscopy. The typical energy resolution of a silicon surface barrier detectors with 100 μm thick depletion layer and 100 mm^2 active area for 5.5 MeV α-particles is 17 keV [13]. In this study

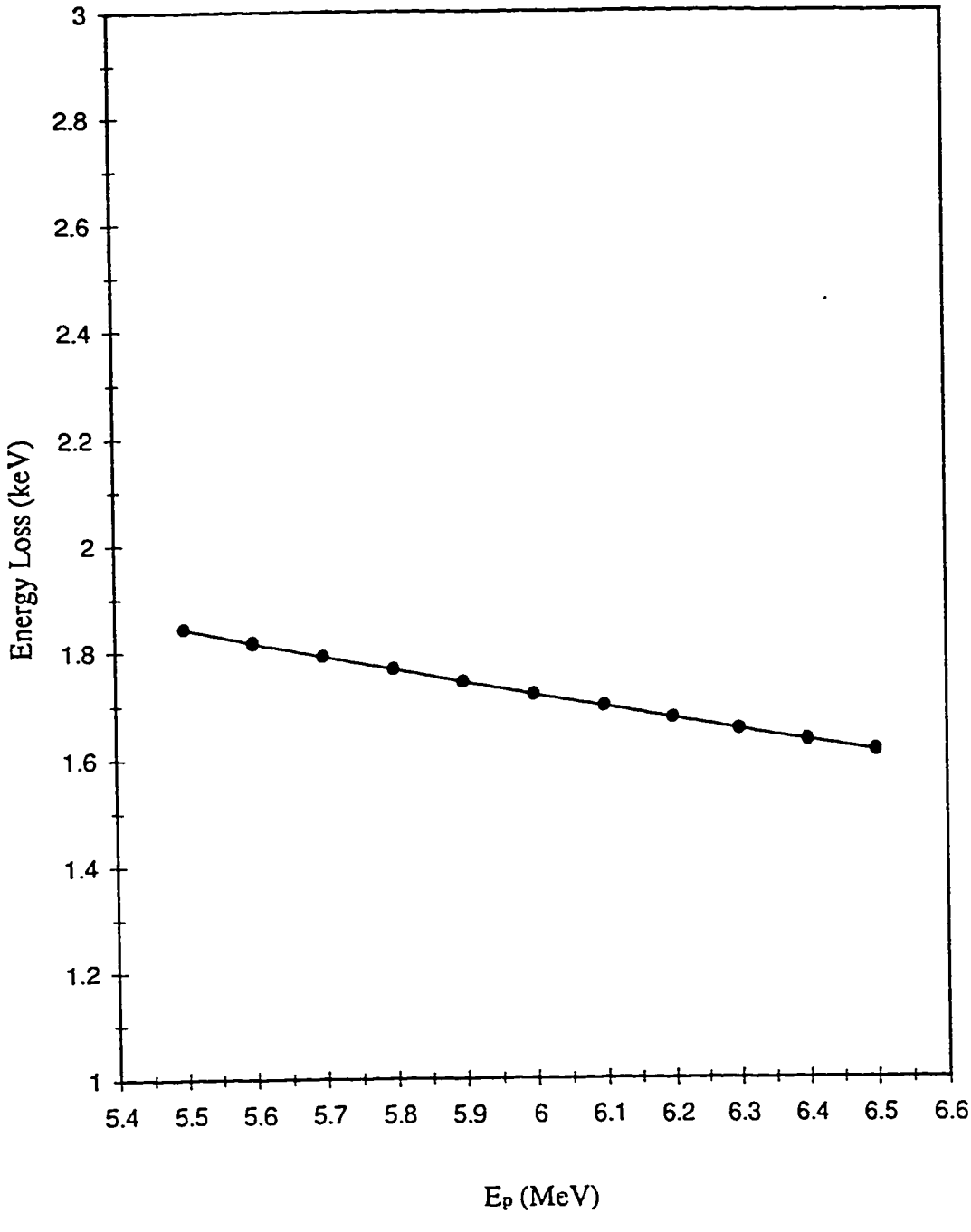

Figure 3.5 Energy loss of 6 MeV reaction protons in the ^{13}C target foil.

silicon surface barrier detectors were used to detect protons from $^{13}C(d, p)^{14}C$ reaction. The required detector depletion layer thickness and the active area were determined from the energies of the particles to be detected and the desired detector solid angle. The energy of the protons from the $^{13}C(d, p)^{14}C$ reaction is 6 MeV. Figure 3.6 shows the silicon detector nomogram [13]. The horizontal dash line from 6 MeV protons with depletion layer depth indicates that a depletion depth of 300 μm would be sufficient to stop 6 MeV protons and 23 MeV α-particles. The detector was placed at a distance of 131 mm from the target with a 1.25 m.sr solid angle. Therefore any detector having an active area greater than 20 mm^2 can be used in this experiment. In this experiment EG&G Ortec SSB detectors with 300 μm depletion layer thickness and 100 mm^2 effective area were used. These detectors have 14 keV energy resolution for 5.45 MeV α-particles and operate at 50 V bias voltage.

3.5 BEAM SUPPRESSER FOIL

When a deuteron beam hits a ^{13}C target, $^{13}C(d, p)$, $^{13}C(d, \alpha_0)$, $^{13}C(d, \alpha_1)$ and $^{13}C(d, t)$ reactions take place. Along with the above nuclear reaction, elastic scattering reaction $^{13}C(d, d)$ also takes place. The cross section of $^{13}C(d, d)$ reaction is several orders of magnitude larger than the remaining nuclear reactions. Since the silicon surface barrier detector is equally sensitive to all types of charged particles, the intense beam of the scattered deuterons will cause very large dead-times hindering the detection of particles of lesser intensity. Therefore it is desired to suppress the elastically scattered deuterons by putting a sufficiently thick absorber foil in front of the detector. The thickness of the foil should be such that it stops all elastically scattered

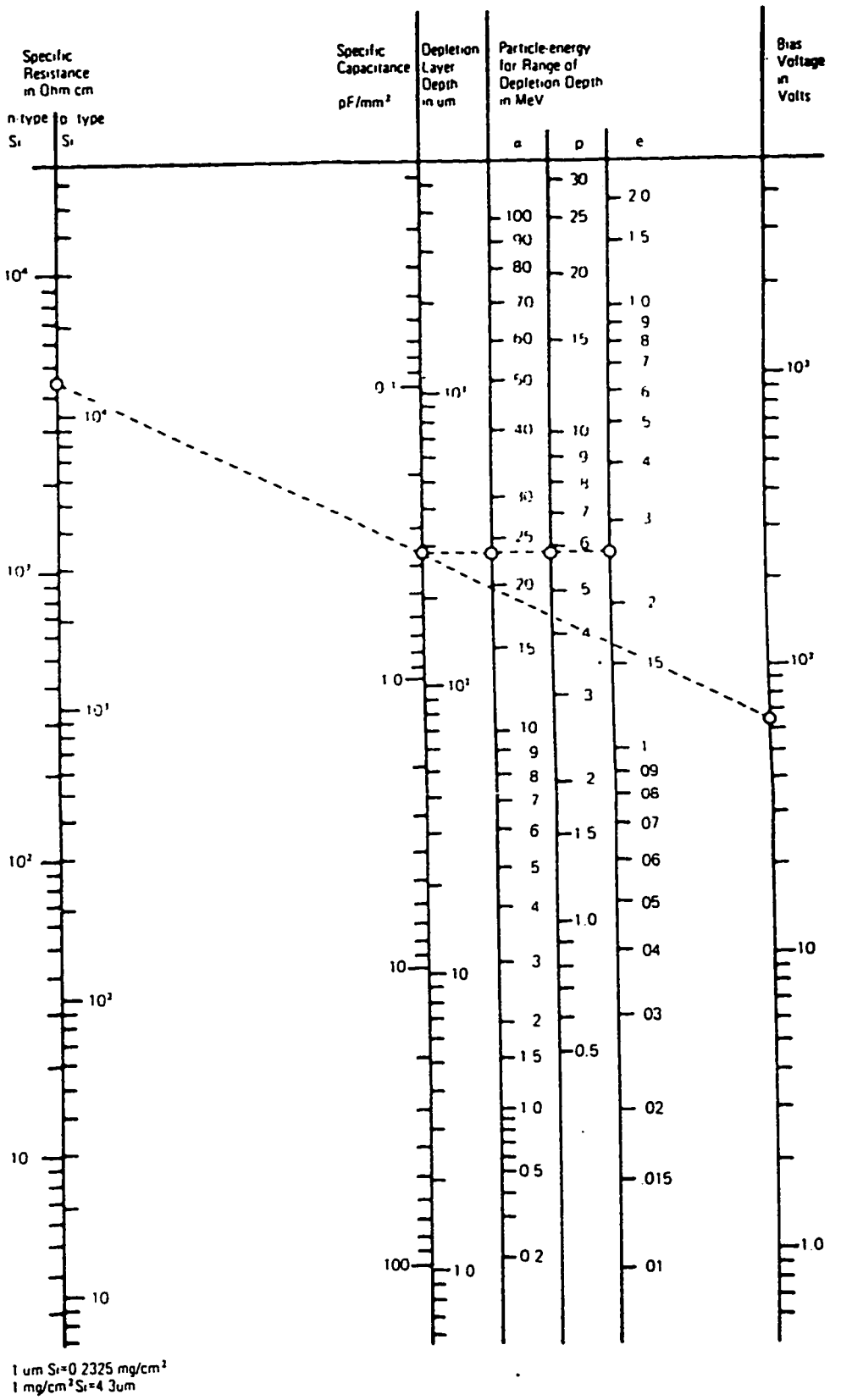

Figure 3.6 Silicon detector nomogram.

deuterons but allows the particles of interest like protons, α-particles and tritons to pass through without significant energy loss. In order to choose proper thickness and type of the foil, energy loss of deuterons and protons in the Mylar and Aluminum foils were calculated using the code "Babel". It was found that 2.6 μm thick Mylar foil and 4 μm thick Aluminum foil could stop 300-350 keV deuterons completely. On the other hand the energy loss of 6 MeV protons from $^{13}C(d, p)^{14}C$ reaction in Mylar foil is half of that in 4 μm Aluminum foil. Figure 3.7 shows the energy loss of 5-6.5 MeV protons in 2.6 μm and 4 μm Mylar and Aluminum foils. In the present study 2.6 μm thick Mylar foil was used to suppress elastically scattered deuterons. Since this thickness can stop 300 keV deuterons, $^{13}C(d, p)^{14}C$ measurements with 300-350 keV deuterons was carried out using two fold Mylar foils.

3.6 ELECTRONICS

In this study eight SSB detectors with identical sets of electronics were used. Separate electronics was used in this study to measure the particle flux through the charge collected at the Faraday cup of the scattering chamber.

The major components of the individual detector signal processing electronics were preamplifier and amplifier. The preamplifier was used to match the impedance between the detector and the spectroscopy amplifier. Also the detector bias voltage was provided through the preamplifier. The output of the preamplifier was taken out of the accelerator hall through a patch panel to a spectroscopy amplifier. The amplifier was used to amplify and shape the detector signal with a shaping time

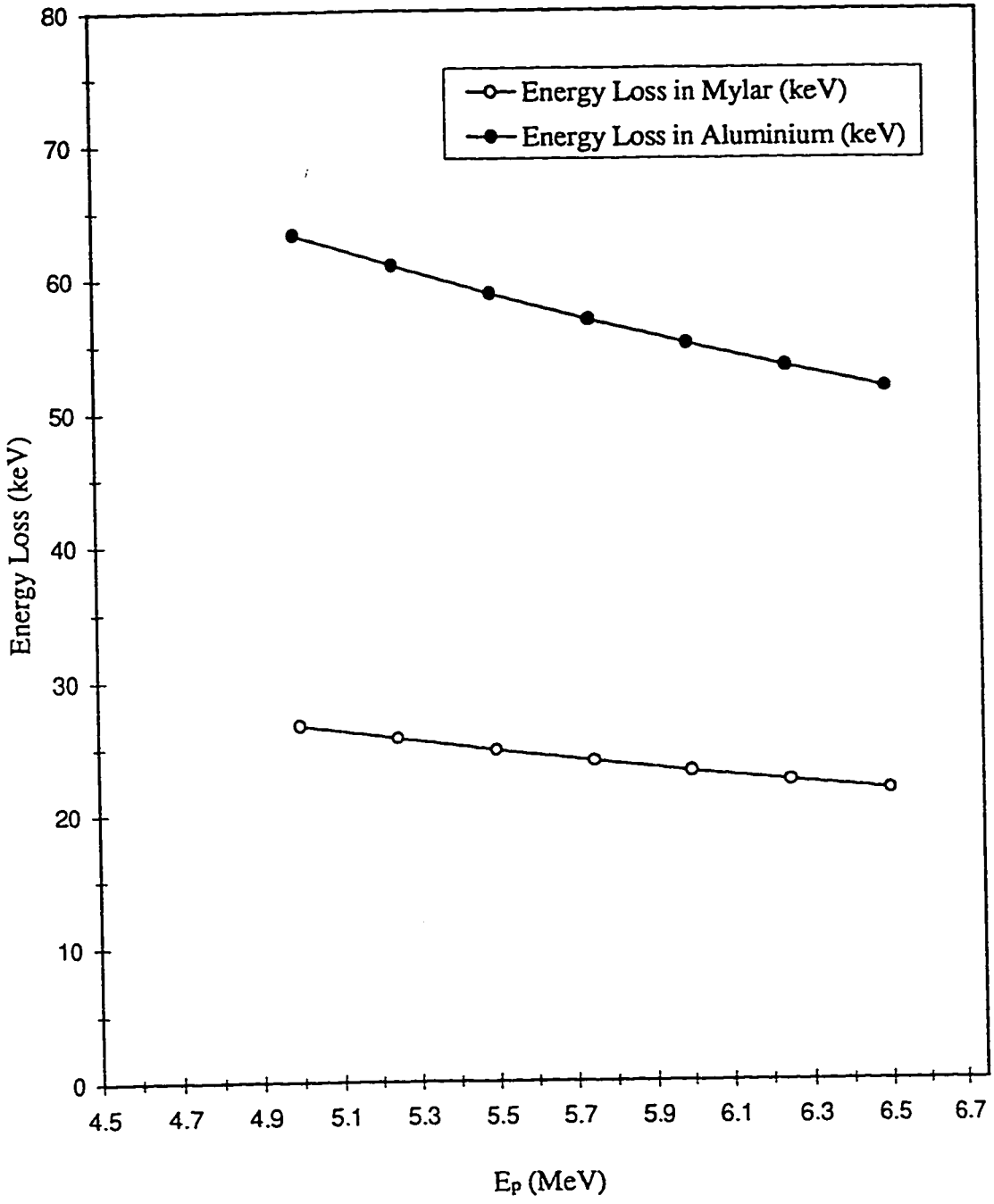

Figure 3.7 Energy loss of protons in Mylar and Aluminum foils.

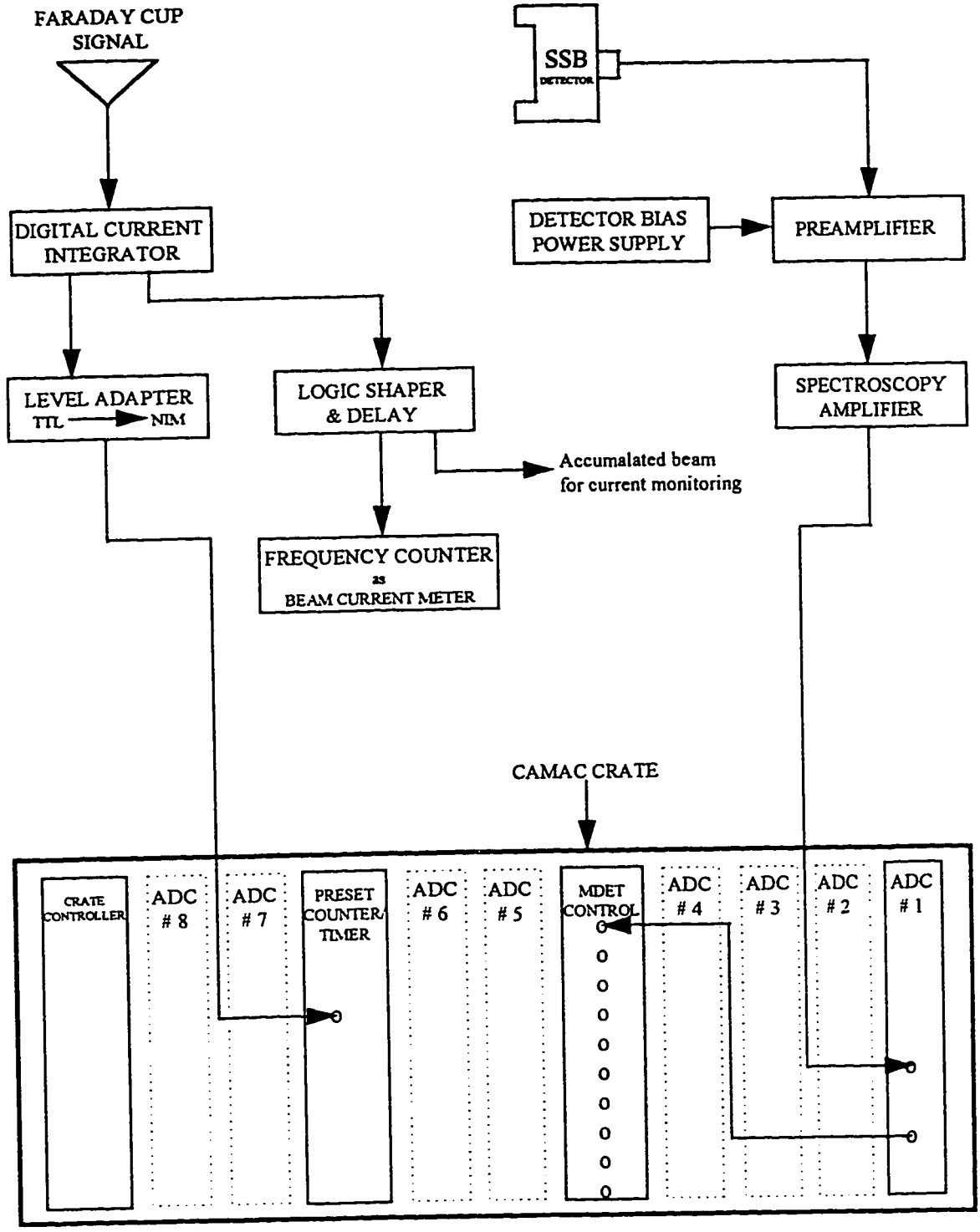

Figure 3.8 Electronics for a typical SSB detector.

constant of 1 μs. Finally the amplifier signal of the detector was fed to an Analog to Digital Converter (ADC). Figure 3.8 shows the electronics used for a typical detector.

The other circuit of the electronics was used to measure the integrated charge from the Faraday cup of the scattering chamber. This was achieved by feeding the Faraday cup signal to a Digital Current Integrator (DCI) which digitized the charge signal into pulses. A conversion factor of 10^{-8}C was used to digitize the dc beam current into pulses. The output of DCI was converted into NIM signal by a LeCroy Level Adapter and then fed into the Borer CAMAC Preset Counter/Timer which control the turning "ON" and "OFF" of the data acquisition process. Data was acquired for a preset amount of number of pulses of DCI acquired by the preset counter at the Faraday cup. This was achieved by loading a fixed number in the CAMAC preset scalar through XSYS program and down counting it by the pulses from DCI supplied through the level adopter.

3.7 DATA ACQUISITION AND ANALYSIS SYSTEM

The data acquisition and analysis facility at ERL is built around Micro-VAX system. It uses a CAMAC/Micro-programmable Branch Driver (MBD) hardware to acquire the data [14,15,16]. The data acquisition system uses the XSYS software package which was developed in the Triangle Universities Nuclear Laboratory, USA. Generally a data acquisition program consists of three files namely, '*.COM', '*.DAP' and '*.EVL' files.

The COM file contains XSYS commands which are executed at various stages of the experiment. The DAP file is CAMAC and sub process control files. It

contains CNAF commands for CAMAC crate configuration and information on the Micro-VAX data buffer size. Each MBD channel requires a separate DAP file. DAP files are also used for general sub-processes control information such as the scalar-timer preset or the scalar display. These files are very hardware specific. The EVL file contains sorting algorithms for individual ADC and its MBD channel. Each active MBD channel requires one DAP and one EVL file for the data acquisition. If the data acquisition is controlled by a preset scalar, it needs additional DAP file to read the preset scalar.

In this experiment, data from eight detectors were acquired using one MBD channel. This was achieved through a special data acquisition code "MDET". In this code eight ADCs are initialized in the MDET.DAP file and read simultaneously. A specially designed module, incorporated in the CAMAC crate, looks at the busy signal for each ADC. Later the ADC addresses are sorted out in the specified area by MDET.EVL file. Data was acquired for a fixed number of counts, counted by the preset scalar. The listing of data acquisition codes are given in appendix A.

3.8 ENERGY CALIBRATION OF SSB DETECTORS

The SSB detectors were used to detect the protons from the $^{13}C(d, p)^{14}C$ reaction. In order to identify the proton peaks, energy calibration of was carried out using a mixed α-source. The calibration source was evaporated on a stainless steel disc and it contained three elements ^{239}Pu, ^{241}Am and ^{244}Cm with 5.156, 5.486 and 5.806 MeV α-particles respectively. The relative intensities of these lines of ^{239}Pu, ^{241}Am and ^{244}Cm isotropic are 73%, 86% and 77% respectively. Since the

detectors were to be used in the experiments with 2.5 μm (0.1 mil) thick Mylar foil, the energy calibration of the detector was carried out with and without Mylar foil in front of the detector. From these measurements the energy loss of the α-particles in the foil was also determined and was subsequently used to determine the foil thickness.

The three α-line spectrums, one with and the other without Mylar foils are shown in Figure 3.9 and Figure 3.10 respectively. Due to the energy loss of the α-particles in the Mylar foil, the three α-lines in the detector spectrum with Mylar foil were shifted towards the lower energies channels. The energy loss for 5.156, 5.486 and 5.806 MeV α-particles were calculated from shift in energy channels. Table 3.1 shows the experimentally measured and calculated energy loss of the α-particles peaks in the Mylar foil. The experimental value agrees within 16-19% of the calculated values. There is an average 300 keV of energy shift in α-lines indicating the thickness of the Mylar foil for the α-particles.

3.9 EXCITATION FUNCTION AND ANGULAR DISTRIBUTION MEASUREMENTS OF $^{13}C(d, p)^{14}C$ REACTION

The excitation functions for the $^{13}C(d, p)^{14}C$ reaction were measured at eight angles, four forward angles and four backward angles over 200-350 keV deuteron energies. The measurements were carried out in steps of 10 keV, except from 200-250 keV where the energy step was increased to 50 keV. The angles for excitation functions measurements were 30°, 48°, 66°, 90°, 110°, 128°, 146° and 164°. The selected charge preset for data acquisition varied from 3.7-23.5 mC for 350-200 keV deuteron energies respectively. For each excitation function new ^{13}C target was

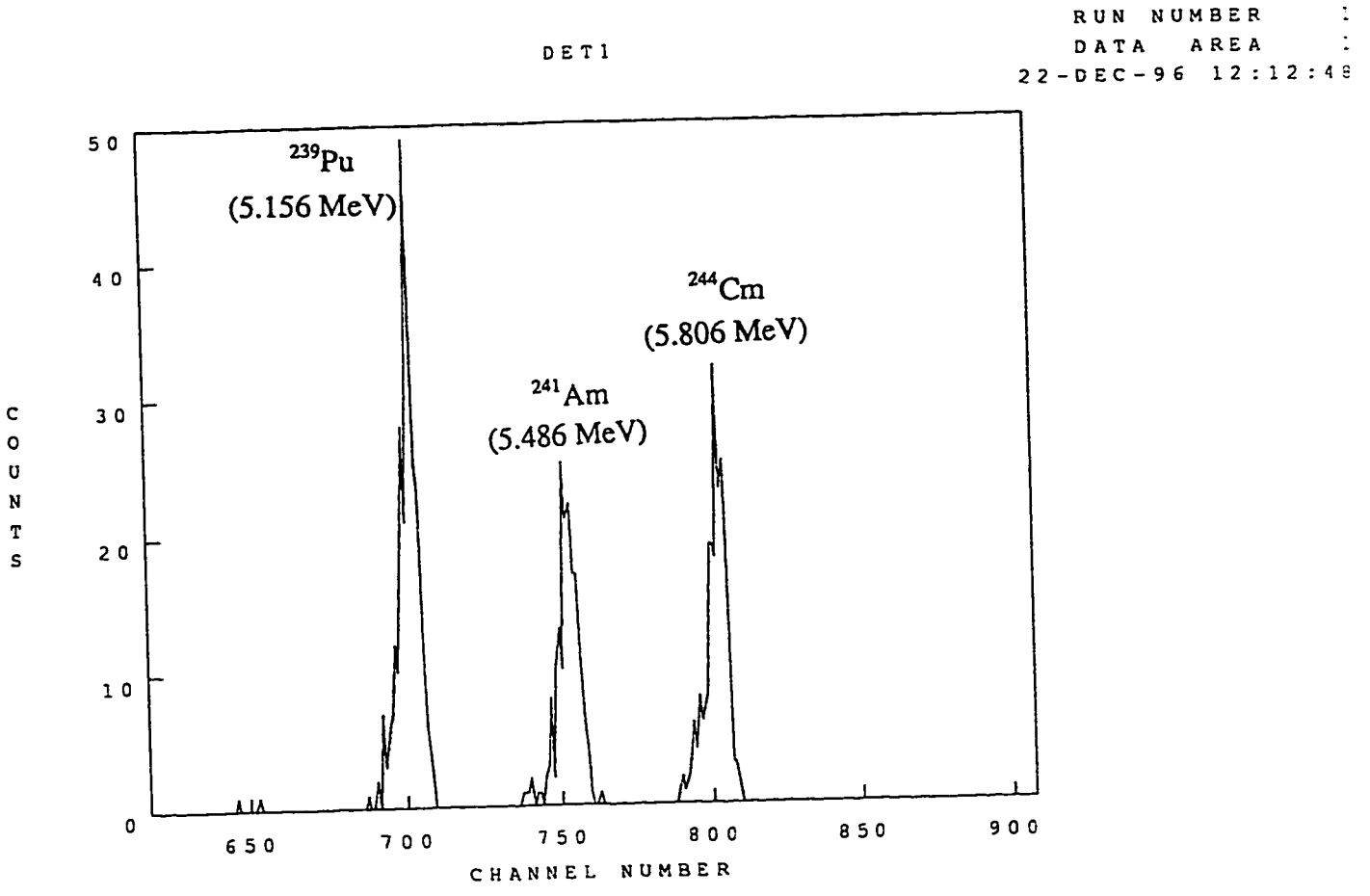

Figure 3.9 Pulse height spectrum of SSB detector with Mylar foil.

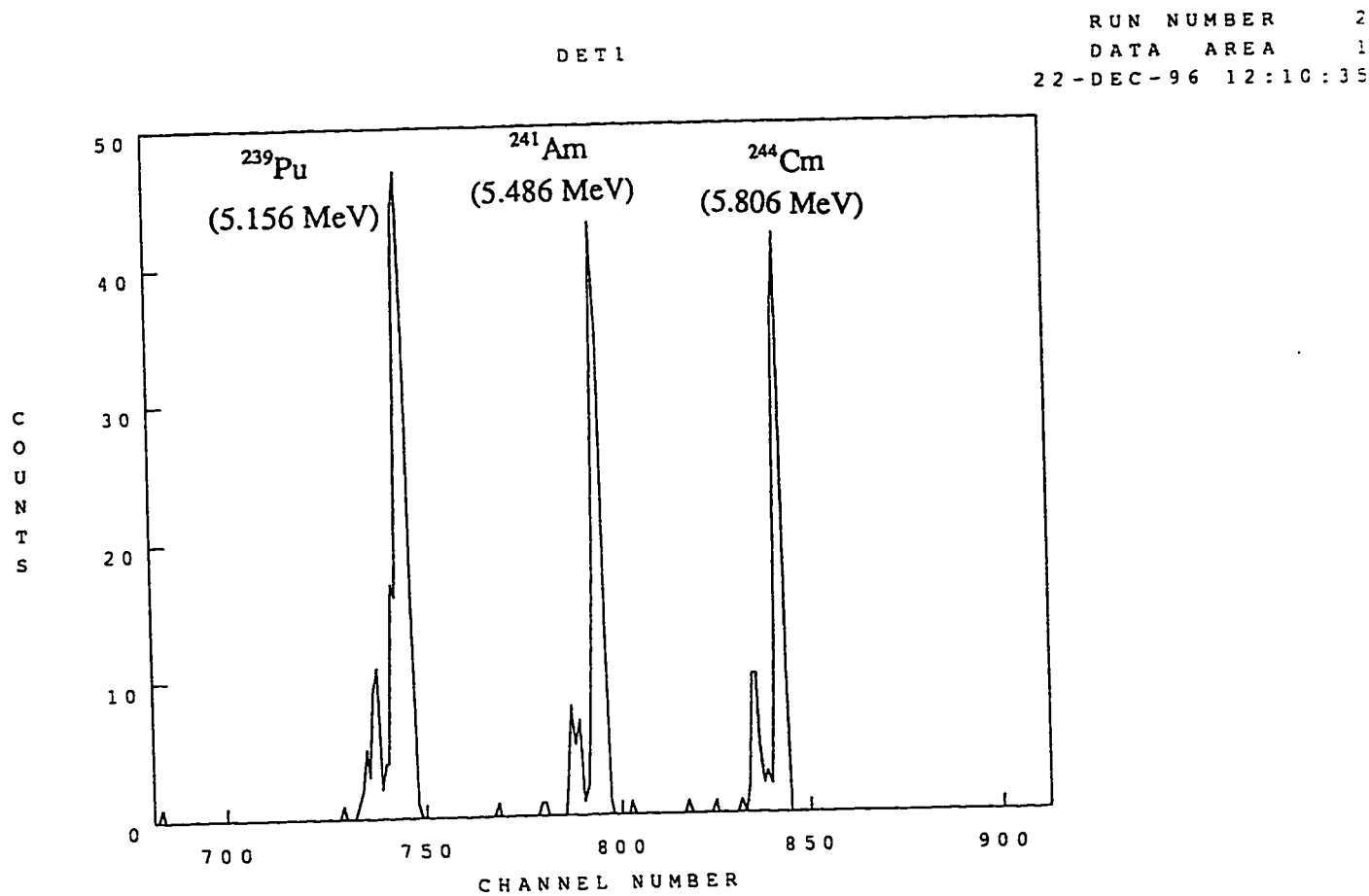

Figure 3.10 Pulse height spectrum of SSB detector without Mylar foil.

Table 3.1 Energy loss of α particles in the Mylar foil.

α particles energy (MeV)	FWHM (keV)	ΔE_x (exp.) (MeV)	ΔE_x (calc.) (MeV)	% deviation
5.156	38.9	0.352	0.304	16
5.486	32.4	0.343	0.289	19
5.806	38.0	0.326	0.278	17

mounted. To minimize the carbon buildup on the target, the beam collimator was cooled by attaching it with a cold-finger which was immersed in liquid nitrogen. A negative bias voltage of 200V was applied to the Faraday cup throughout the experiment to suppress the knockout electrons in the Faraday cup.

The angular distributions for the $^{13}C(d, p)^{14}C$ reaction were measured for fourteen angles at 200, 250, 270, 290, 310, 335 and 350 keV deuteron energies. The minimum angle was 30° and the maximum angle was 164°. Since eight detectors were used simultaneously to measure the angular distributions, two runs were required to cover the fourteen angles with two detectors as monitors. First run was taken from the data of excitation function measurement while the second run was taken anew with different set of angles, hence covering entire angle range. Two detectors were kept fixed at 30° and 164° as monitors for the two runs. New ^{13}C foils were used for all runs. In order to carry out the angular distribution measurements at eight angles in one run the target holder was fixed at an angle of 45° with respect to the beam axis and remained at the same position throughout the experiment. The beam current was kept 1.5 μA on the average. Since the $^{13}C(d, p)^{14}C$ reaction shows a forward peaking in angular distributions, reaction yield was low at the backward angles. At lower energies, yield is still lower at backward angles. To have reasonable minimum and maximum uncertainties (2-6%), data was acquired for 3.7-23.5 mC charge incident at the target. All the angular distributions and as well as the excitation functions measurements were normalized to 3.7 mC preset charge at the target for cross sections calculations.

CHAPTER 4

DATA REDUCTION AND EXPERIMENTAL RESULTS

The data reduction and analysis of $^{13}C(d, p)^{14}C$ reaction cross section data was carried out using ERL Micro-VAX computer. Proton peak for each spectrum was carefully stripped and its yield was normalized and then used to calculate the excitation function and differential cross section.

4.1 DATA STRIPPING AND NORMALIZATION

Each spectra was analyzed during off-line analysis. In this analysis the proton peak was identified for each individual spectrum and a gate was set on the peak for area integration. Since the $^{13}C(d, p)^{14}C$ reaction has the larger Q-value among the other competing $^{13}C(d, t)$, $^{13}C(d, \alpha_0)$ and $^{13}C(d, \alpha_1)$ reaction, the proton peak was completely separated from other peaks of triton and alpha particles. This resulted in relatively easier peak stripping task. Figure 4.1 shows the proton peak for 200 keV deuteron energy along with a chosen gate at 30°. In all 96 spectra were analyzed to generate the excitation function for 30°, 48°, 66°, 90°, 110°, 128°, 146° and 164° angles for 200-350 keV deuteron energies in 10 keV step. 112 spectra were stripped to cover 14 angles for each of 8 angular distributions measured at 200, 250, 270, 290, 310, 335 and 350 keV deuteron energies.

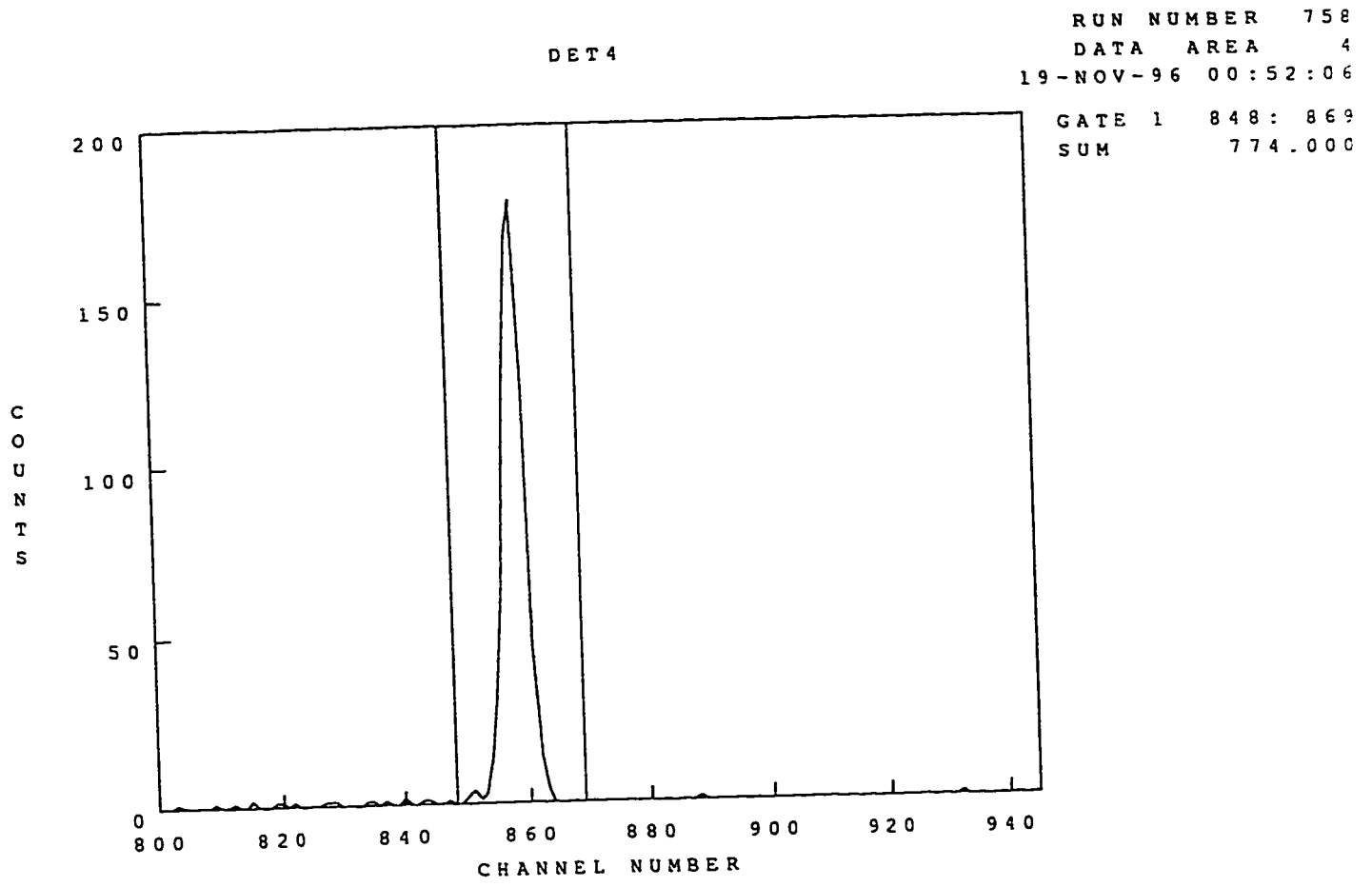

Figure 4.1 Proton peak of $^{13}C(d, p)^{14}C$ reaction at $E_d = 350$ keV at an angle of 164° showing with gate for the peak integration.

The angular distributions for 14 angles at each energy were measured in two runs using 8 detectors. In order to correct for the variation in the target thickness and incident beam flux between the two runs, two detectors were fixed (one at forward and the other at backward angle) at 30° and 164° in both runs as monitors. From the ratio of yield $Y_1(E_d, \theta)$ and $Y_2(E_d, \theta)$ of each monitor detector for run # 1 and 2, a correction factor $C(\theta)$ was calculated using the equation,

$$C(\theta) = \frac{Y_1(E_d, \theta)}{Y_2(E_d, \theta)} \tag{4.1}$$

An average value of the correction factor C was calculated from C(30°) and C(164°) and was multiplied by the yield of remaining 6 detectors in run # 2 to correct for any variation in the target thickness and incident beam flux variation. For 350-270 keV run the values of correction factor was about 1 while for 250 keV data it was 1.4. The large value of correction factor for 250 keV data was may be due to change in target thickness between the two runs. Each angular distribution data was normalized with respect to 370,000 counts of BCI which correspond to 3.7 mC charge measured at the Faraday cup of the scattering chamber.

4.2 EXPERIMENTAL CROSS SECTION CALCULATIONS

The differential cross section for the $^{13}C(d, p)^{14}C$ reaction was calculated from the normalized yield $Y_N(E_d, \theta)$ at deuteron energy E_d and angle θ using

the formula,

$$\frac{d\sigma(E_d,\theta)}{d\Omega} = \frac{Y_N(E_d,\theta)}{\phi \times N_t \times \Delta\Omega} \tag{4.2}$$

where ϕ is the total number of incident deuterons, N_t is the target nuclei per unit area, and $\Delta\Omega$ is the solid angle subtended by the detector.

The cross section calculations were carried out for ϕ = 6.24×10^{15} incident deuterons, N_t (30 $\mu g/cm^2$ ^{13}C target) = 1.38×10^{18} ^{13}C nuclei/cm^2 and $\Delta\Omega$ = 1.25 m.sr.

The Eq. 4.3 gives the differential cross section in the laboratory (lab.) system, but the cross section data was to be converted in the center-of-mass (c.m.) system for further analysis using nuclear models.

4.3 ERROR ANALYSIS

The total uncertainty in the measurements of proton yield arises from the statistical and the systematic errors which are described below.

4.3.1 Statistical errors

The statistical uncertainty ΔY_1 (E_d, θ) in the yield Y_1 (E_d, θ) data points of run # 1 would be simply given as,

$$\Delta Y_1(E_d,\theta) = \sqrt{Y_1(E_d,\theta)} \tag{4.3}$$

while the statistical uncertainty $\Delta Y_C(E_d, \theta)$ in the corrected yield $Y_N(E_d, \theta)$ data of run

2 was calculated to be ;

$$\frac{\Delta Y_C(E_d,\theta)}{Y_C(E_d,\theta)} = \frac{\Delta Y_2(E_d,\theta)}{Y_2(E_d,\theta)} + \frac{\Delta C(E_d)}{C(E_d)} \tag{4.4}$$

where,

$$\frac{\Delta C(E_d)}{C(E_d)} = \sqrt{\left(\frac{1}{Y_1(E_d,30^\circ)} + \frac{1}{Y_2(E_d,30^\circ)}\right)^2 + \left(\frac{1}{Y_1(E_d,164^\circ)} + \frac{1}{Y_2(E_d,164^\circ)}\right)^2}$$

4.3.2 Systematic errors

The systematic error associated with the experiment was due to the flux attenuation inside the target, the uncertainty in the charge integration and the finite angular resolution. The thickness of the target was assumed constant and this was due to the fact that target was kept at the same inclined angle with respect to the beam axis.

Cross section was calculated using the beam flux measured at the Faraday cup after transmitting through the target. During transmission of the beam through the target, part of it may be lost due to absorption or scattering in the target. This is a cause of systematic error. In order to estimate this error, ratio of the total incident beam flux measured at the Faraday cup, once transported directly and then transmitted through the target, is taken. This measurement was carried out for 150 keV deuteron energy where it was assumed that particle flux loss due to nuclear reactions was negligible.

The current integrator was used for precise measurement of charge and thus requires calibration. For the calibration purpose first the current from a variable current source was measured directly by an ammeter and was compared with the value

obtained with the current integrator itself. The current reading of the integrator and the ammeter were used to determine the systematic error in charge integration.

The systematic error due to flux attenuation was 2% and due to charge integration it was estimated to be 3%. The spread due to finite aperture of the detector was 0.66 degree. This 0.66 degree result at the most in 2.0 % error in the yield measurement. This error was calculated from the steepest part of the yield curve at 350 keV. The total systematic error was 4%.

The calculated statistical and the total uncertainties in the excitation functions and angular distributions are listed in Table 4.1 and Table 4.2. It could be seen from these tables that the statistical uncertainties varied from 1-6% except that for 200 keV for which the statistical uncertainty was 5-23%. This large uncertainty at 200 keV was due to the low yield count at this energy.

4.4 EXPERIMENTAL RESULTS AND DISCUSSION

The excitation functions of $^{13}C(d, p)^{14}C$ reaction were measured over 200 to 350 keV deuteron energies at 30°, 48°, 66°, 90°, 110°, 128°, 146° and 164° in 10 keV step. Figures 4.2-4.5 show these excitation functions. All these figures contain only statistical uncertainties. For 30° and 48° excitation functions statistical uncertainties are small and amounts to 1.5-2.0 % while for 66° and 90° excitation function the statistical uncertainties are 2-4 %. For 110°, 128° and 146° excitation function statistical uncertainties range from 5-6 %. Since cross section increases after 150°, the statistical uncertainties for 164° excitation function decreases to 4-5 %. The excitation functions

Table 4.1 Uncertainties in the excitation functions.

Angle	Statistical uncertainty (%)	Total uncertainty (%)
30°	1.5-1.7	5.5-5.7
48°	1.8-2.0	5.8-6.0
66°	2.4-2.7	6.4-6.7
90°	3.1-3.8	7.1-7.8
110°	4.7-5.6	8.7-9.6
128°	5.2-5.8	9.2-9.8
146°	5.0-5.7	9.0-9.7
164°	3.8-5.0	7.8-9.0

Table 4.2 Uncertainties in the angular distributions.

E_d (keV)	Statistical uncertainty (%)	Total uncertainty (%)
200	5.2-23.5	9.2-27.5
250	1.6-6.7	5.6-10.7
270	1.6-5.8	5.6-9.8
290	1.6-5.7	5.6-9.7
310	1.7-5.8	5.7-9.8
335	1.7-5.7	5.7-9.7
350	1.5-5.7	5.5-9.7

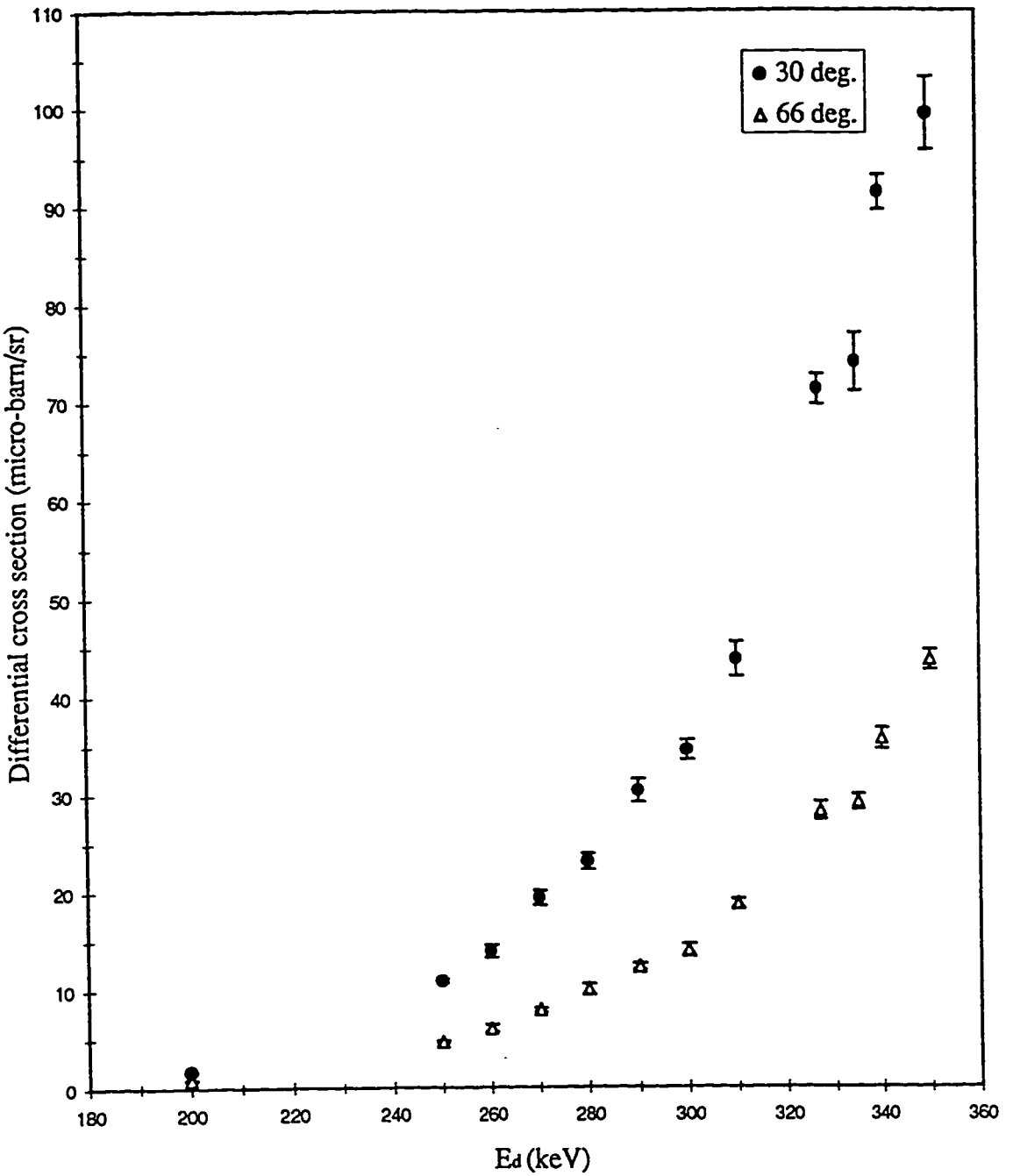

Figure 4.2 Excitation functions of $^{13}C(d, p)^{14}C$ reaction at 30° and 66°.

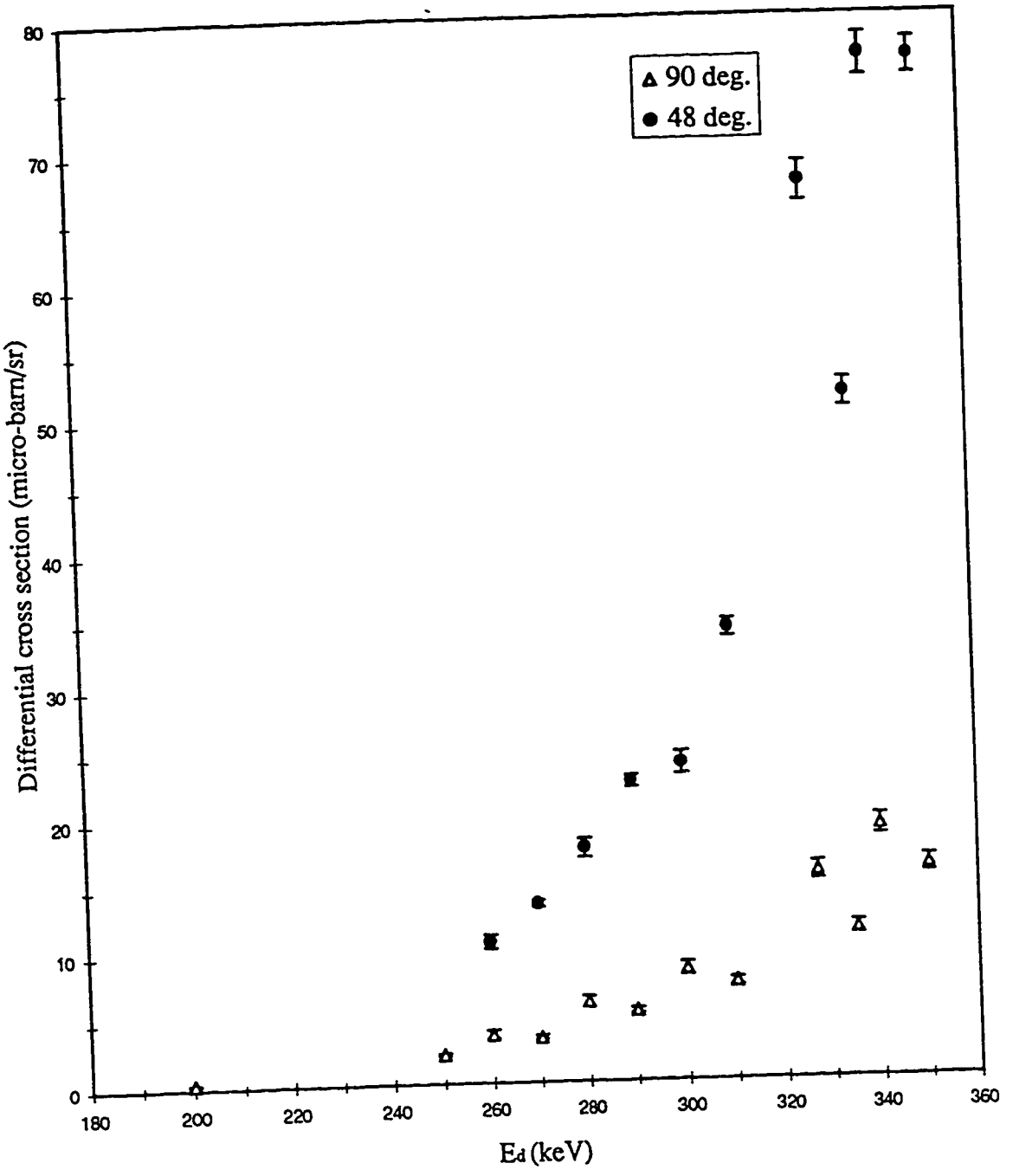

Figure 4.3 Excitation functions of $^{13}C(d, p)^{14}C$ reaction at 48° and 90°.

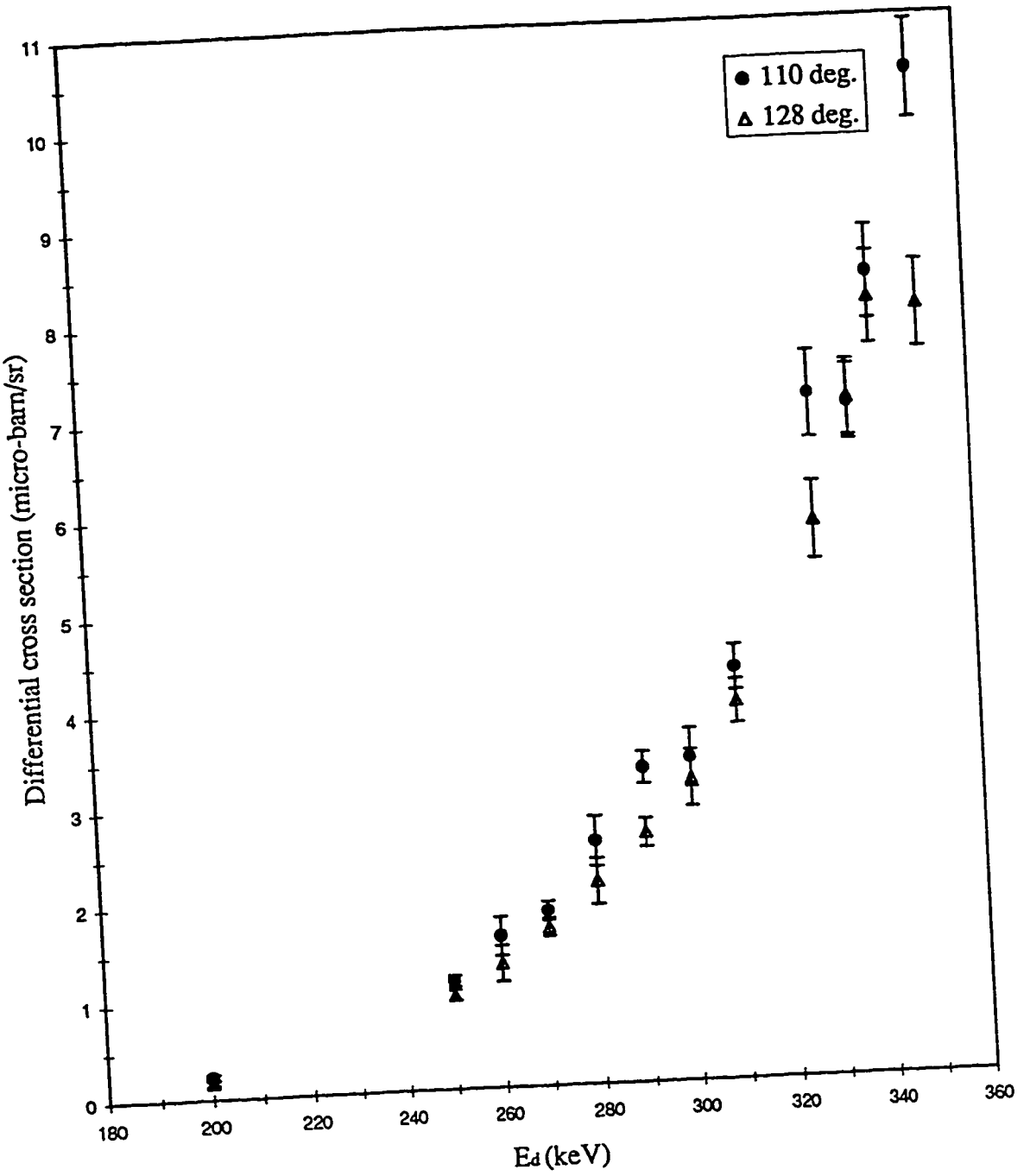

Figure 4.4 Excitation functions of $^{13}C(d, p)^{14}C$ reaction at 110° and 128°.

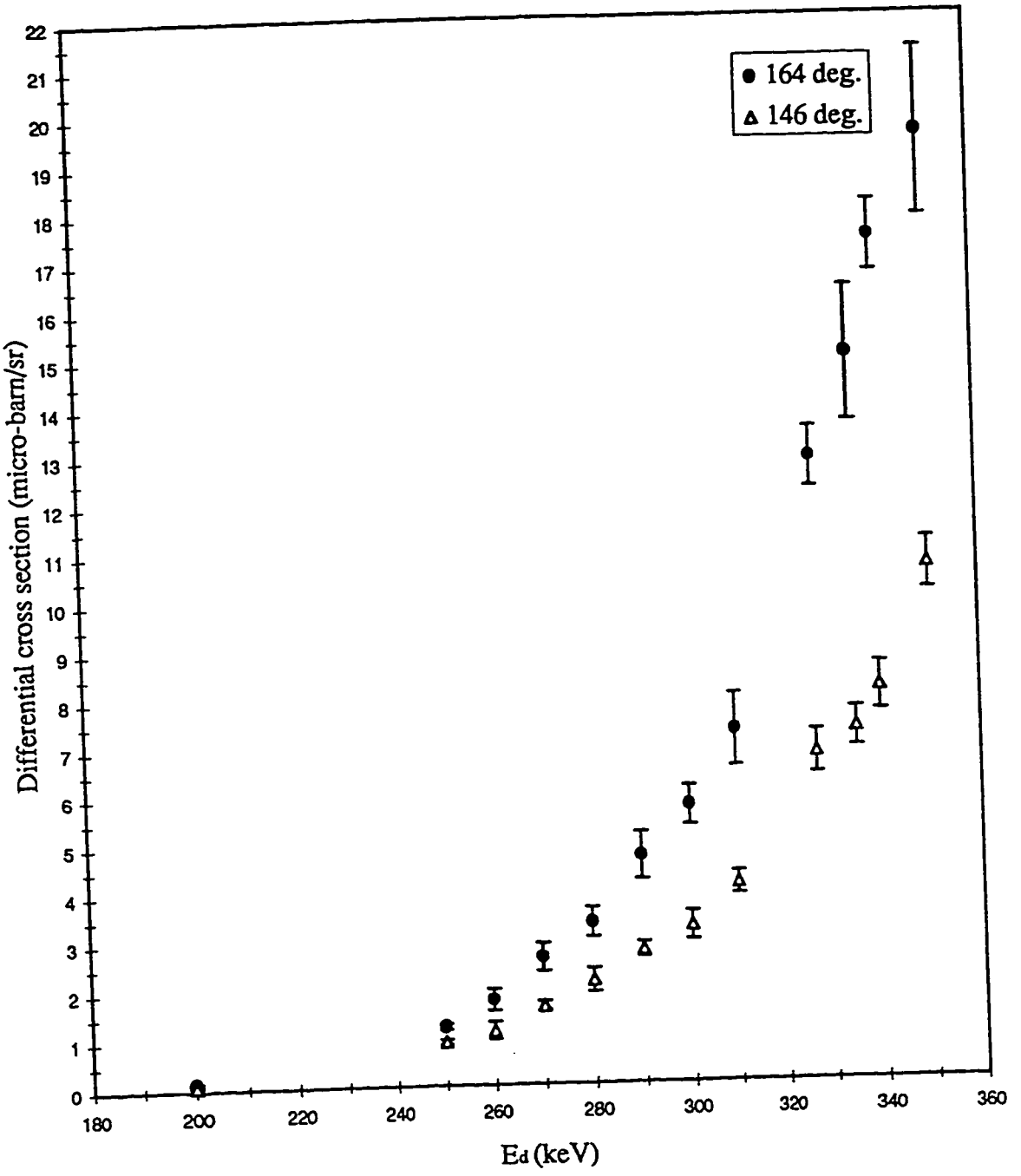

Figure 4.5 Excitation functions of $^{13}C(d, p)^{14}C$ reaction at 146° and 164°.

do not show resonance structure. They have increasing trend with deuteron energy. Excitation functions data is listed in appendix B.

Angular distributions of $^{13}C(d, p)^{14}C$ reaction were measured at 200, 250, 270, 290, 310, 335 and 350 keV deuteron energies. Figure 4.6-4.8 show the angular distributions of $^{13}C(d, p)^{14}C$ reaction at 200, 250, 270, 290, 310, 335 and 350 keV deuteron energies. All distributions are forward peaked with a minimum cross section around 120°-130°. At sub-Coulomb barrier it is expected that angular distribution is backward peaked. But for (d, p) nuclear reactions with large Q-values, proton energy exceeds the Coulomb energy and thus the angular distribution is forward peaked even in the sub-Coulomb barrier energy range. This is the case of $^{13}C(d, p)^{14}C$ reaction because the Coulomb barrier for this reaction is about 2.7 MeV and proton energy is 6 MeV which is well above the Coulomb barrier. Therefore angular distribution is forward peaked. In contrast to this case, $^{12}C(d, p)^{13}C$ reaction whose Coulomb barrier is still 2.7 MeV but proton energy is 2.5 MeV, the angular distribution of $^{12}C(d, p)^{13}C$ reaction is backward peaked [17]. Within the statistical uncertainties, all angular distributions of $^{13}C(d, p)^{14}C$ reaction showed a smooth trend and had no structure. For all angles, the cross section decreased with deuteron energy. The rate of decrease of cross section strongly depend upon the deuteron energy and the angles. For all angular distributions cross section at 30° was about 10 times larger than at about 120°-130°. The errors shown in all figures are statistical. The shape of the excitation functions and angular distributions had trends consistent with the data of Putt [1]. In Appendix C differential cross sections are listed in lab. and as well as in c.m. system.

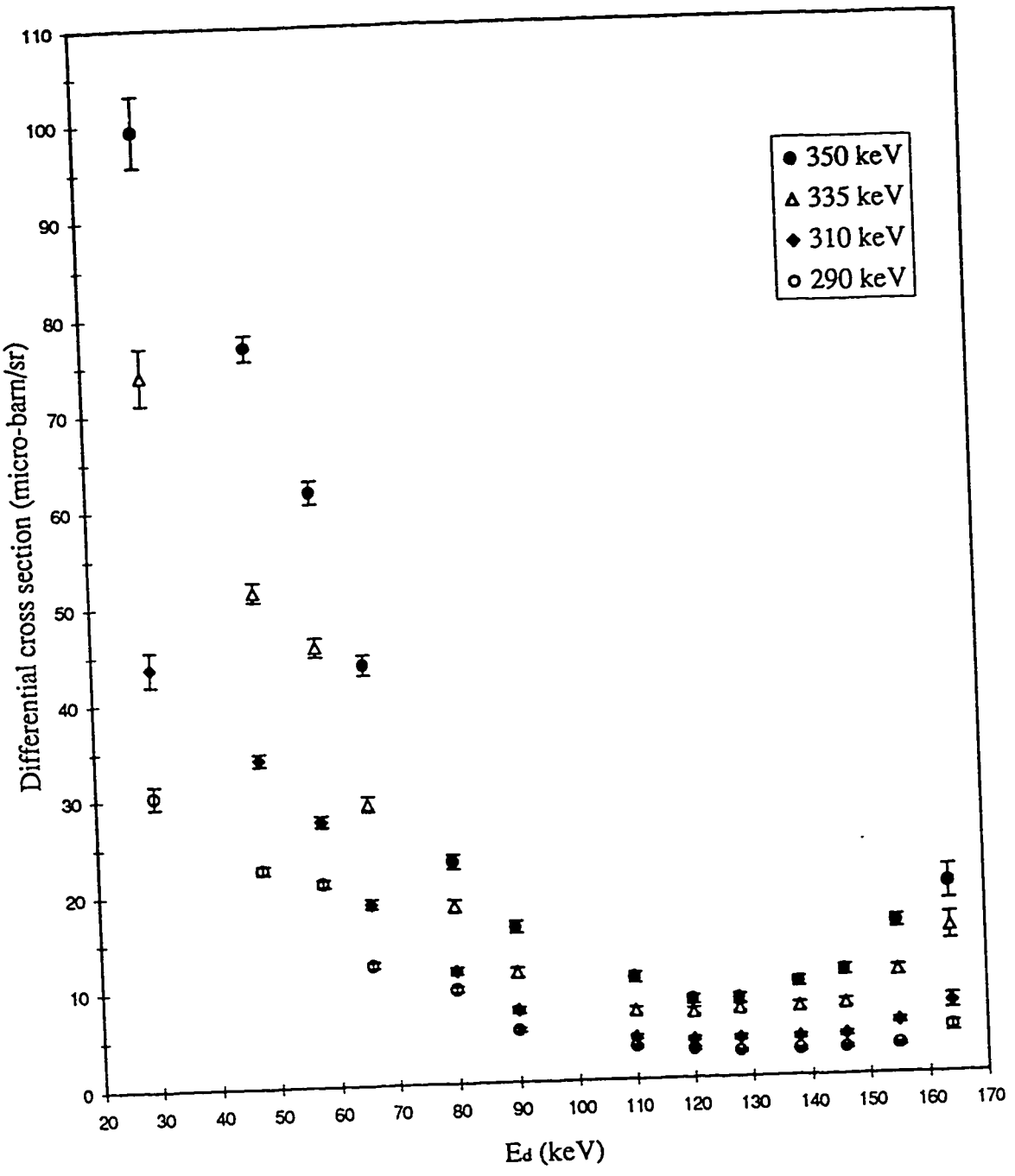

Figure 4.6 Differential cross sections of $^{13}C(d, p)^{14}C$ reaction at 350, 335, 310 and 290 keV deuteron energies. Only statistical errors are plotted.

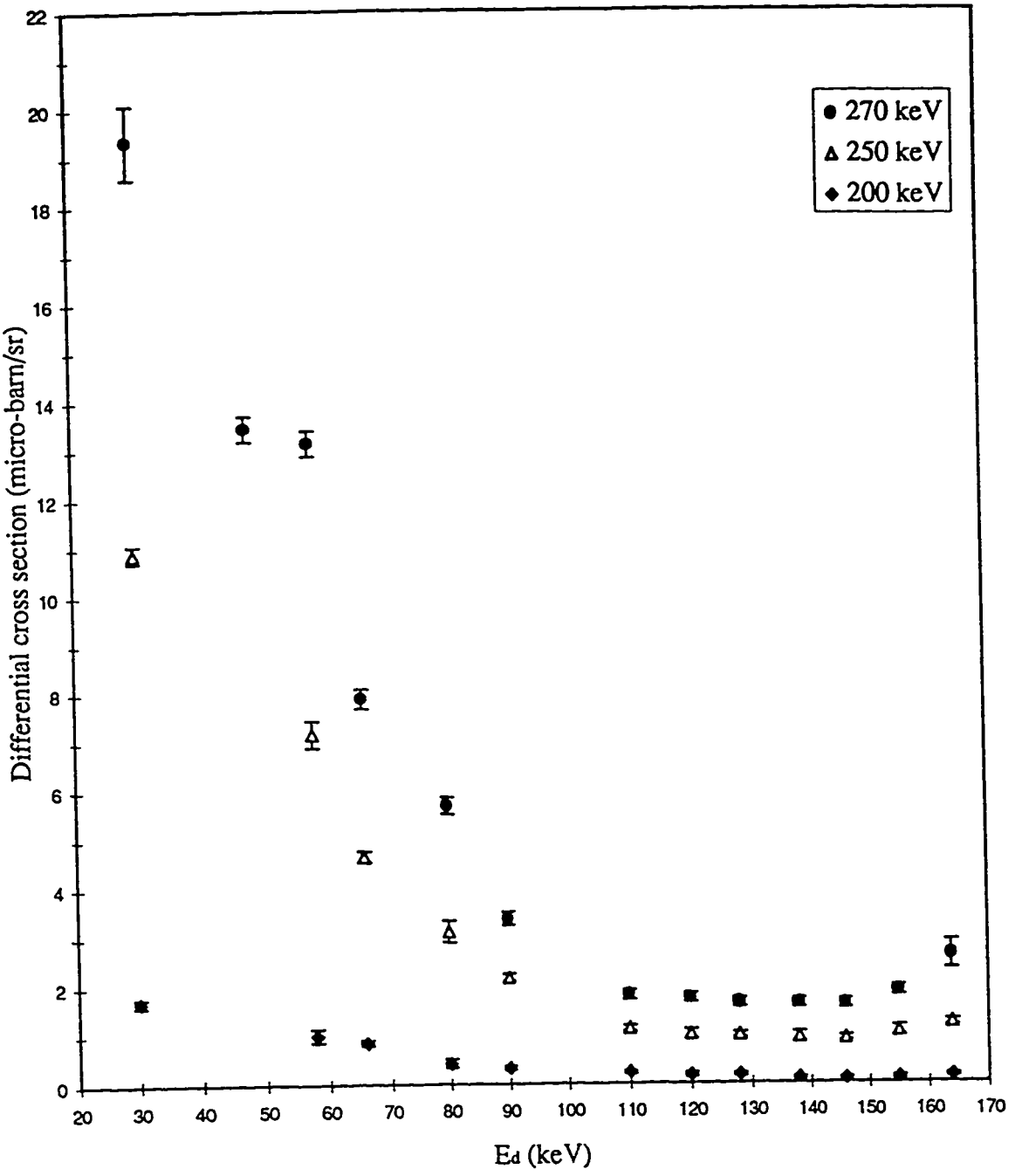

Figure 4.7 Differential cross sections of $^{13}C(d, p)^{14}C$ reaction at 270, 250 and 200 keV deuteron energies. Only statistical errors are plotted.

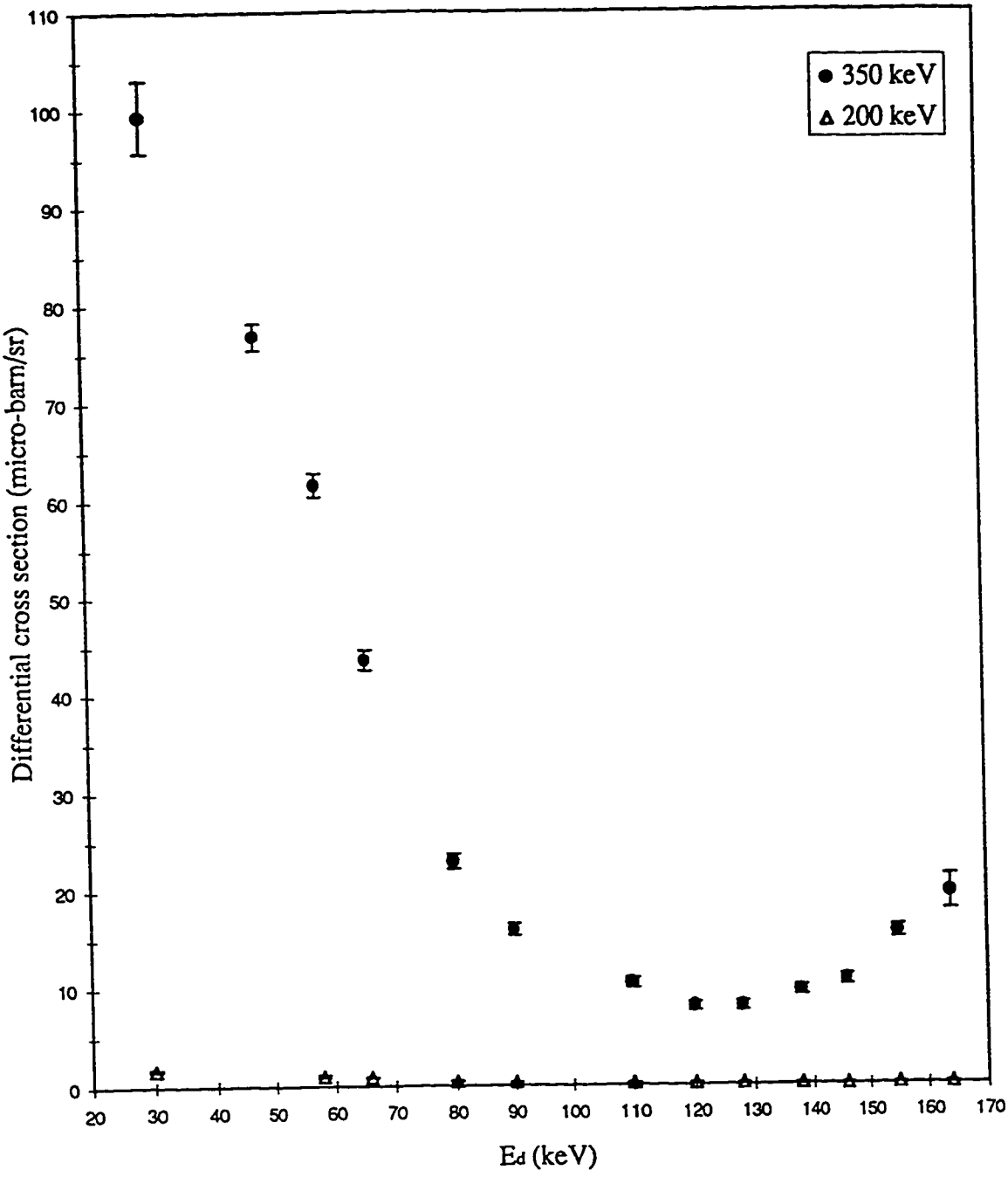

Figure 4.8 Differential cross sections of $^{13}C(d, p)^{14}C$ reaction at 350 and 200 keV deuteron energies. Only statistical errors are plotted.

4.5 EXPERIMENTAL TOTAL CROSS SECTION CALCULATIONS

In order to fit an angular distribution with a nuclear model, total experimental cross section is also required. Generally, the experimental total cross section can be calculated by Legendre polynomials fit to the experimental differential cross section $\frac{d\sigma}{d\Omega}(\theta)$ using the relation,

$$\frac{d\sigma}{d\Omega}(\theta) = \sum_{l=0}^{n} a_l P_l(x) \tag{4.5}$$

where $x = \cos\theta$, a_l are the coefficients and $P_l(x)$ are the Legendre polynomials given by,

$$P_0(x) = 1 \text{ and}$$

$$P_l(x) = [(2l - 1) \times P_{l-1}(x) - (l - 1) P_{l-2}(x)] / l \tag{4.6}$$

In order to obtain the total cross section $\sigma_{tot\text{-}exp}$, equation 4.6 has to be integrated as,

$$\int_0^{\pi} \frac{d\sigma}{d\Omega}(\theta) \sin\theta d\theta = \int_{-1}^{+1} \sum_{l=0}^{\infty} a_l P_l(\theta) d\theta \tag{4.7}$$

Due to orthogonality condition of Legendre polynomials, all terms except for l=0 would vanish and equation 4.8 can be simplified to ;

$$\sigma_{tot\text{-}exp} = 4\pi a_0 \tag{4.8}$$

where a_0 is the coefficient of l=0 term which can be obtained from the fit to the experimental data.

The total cross section $\sigma_{tot\text{-}exp}$ can also be calculated by integrating differential cross section over the solid angle $d\Omega$ given by,

$$\sigma_{tot-exp} = \int_0^{4\pi} (d\sigma / d\Omega) d\Omega = \int_0^{\pi} \sin\theta d\theta \int_0^{2\pi} d\phi (d\sigma / d\Omega) \tag{4.9}$$

If there is no spin polarization, then $d\sigma/d\Omega$ is independent of ϕ and above expression reduces to,

$$\sigma_{tot-exp} = 2\pi \int_0^{\pi} (d\sigma / d\Omega) \sin\theta d\theta = \sum_{a=0}^{I} \frac{2\pi^2}{180} \frac{d\sigma}{d\Omega}(\theta_i) \sin\theta_i \Delta\theta_i \qquad (4.10)$$

where $\Delta\theta_i$ is angular step. Therefore if one has experimental cross section calculation in one degree step, i.e. $\Delta\theta_i = 1$, one can calculate the $\sigma_{tot-exp}$.

In order to fit the data with Legendre polynomials, FORTRAN program 'LEGFIT' [18] and 'LEGPOLXSEC' were used. In order to obtain the best fit to the angular distribution, χ^2 was minimized. The χ^2 was calculated using the formula,

$$\chi^2 = \frac{1}{N-1} \sum_{i=1}^{N} \left(\frac{\sigma_{exp}(\theta_i) - \sigma_{theo}(\theta_i)}{\Delta\sigma_{exp}(\theta_i)} \right)^2 \qquad (4.11)$$

where N is the number of data points, $\sigma_{exp}(\theta_i)$ and $\Delta\sigma_{exp}(\theta_i)$ are the experimental cross section and experimental uncertainties respectively and $\sigma_{theo}(\theta_i)$ is the calculated cross section. A good fit was obtained through best fit to the shape of the angular distribution with a low value of χ^2. Initially the number of terms were varied to obtain the best fit to the shape of the angular distribution by minimizing the χ^2. As a typical example, Figure 4.9 shows the minimum χ^2 as a function of number of terms in Legendre polynomial for 350 keV cross section data. It can be seen that the χ^2 is minimum with $\chi^2 = 0.045$ for six terms but the fitted curve was not good. Hence the number of terms in the Legendre polynomial were reduced to five resulting in a increased value of χ^2 of 0.34. The resulting best fit is shown in Figure 4.10. The total cross section $\sigma_{tot-exp}$ which

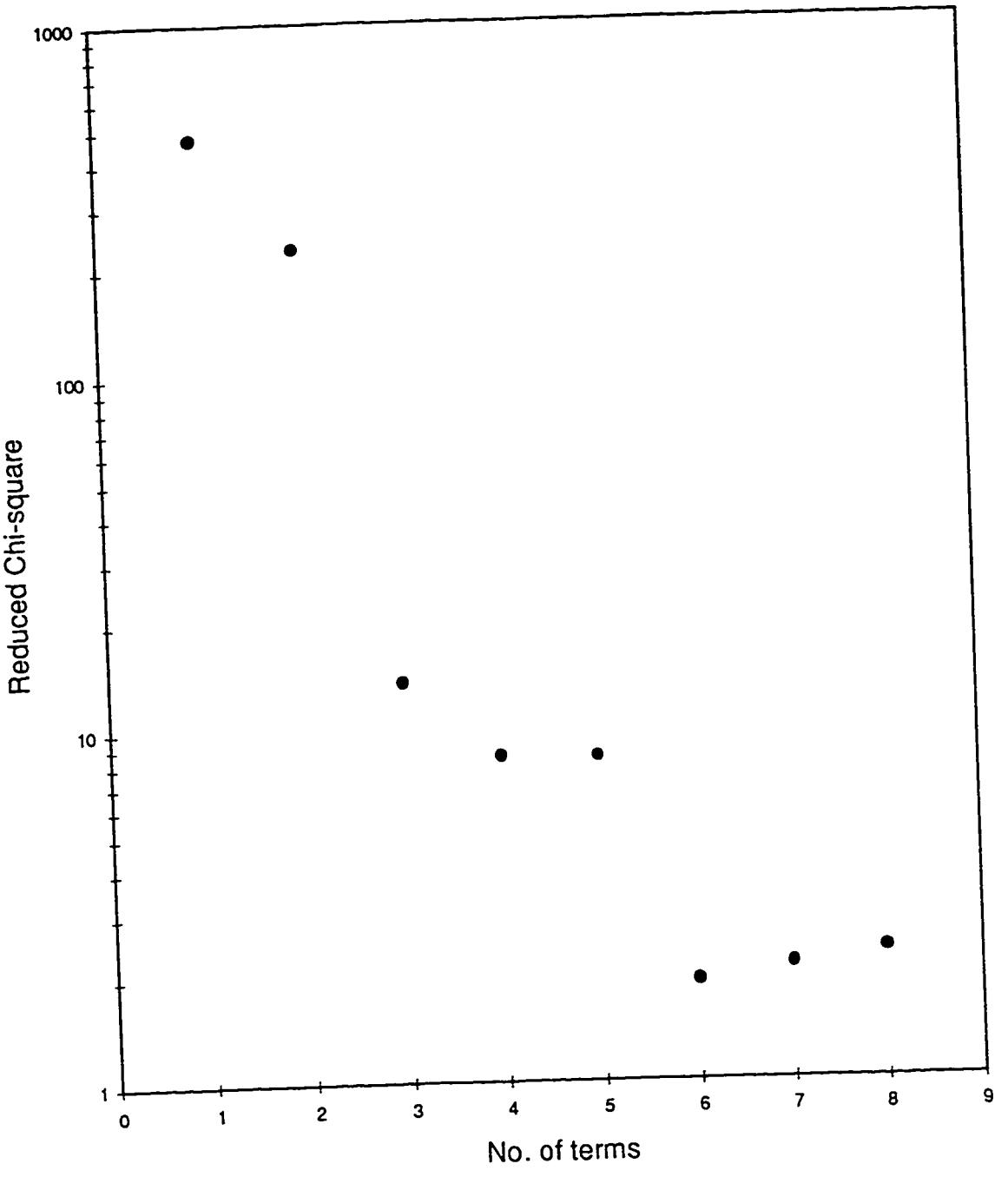

Figure 4.9 Typical graph of minimized χ^2 as a function of number of terms in Legendre polynomial for $E_d = 350$ keV.

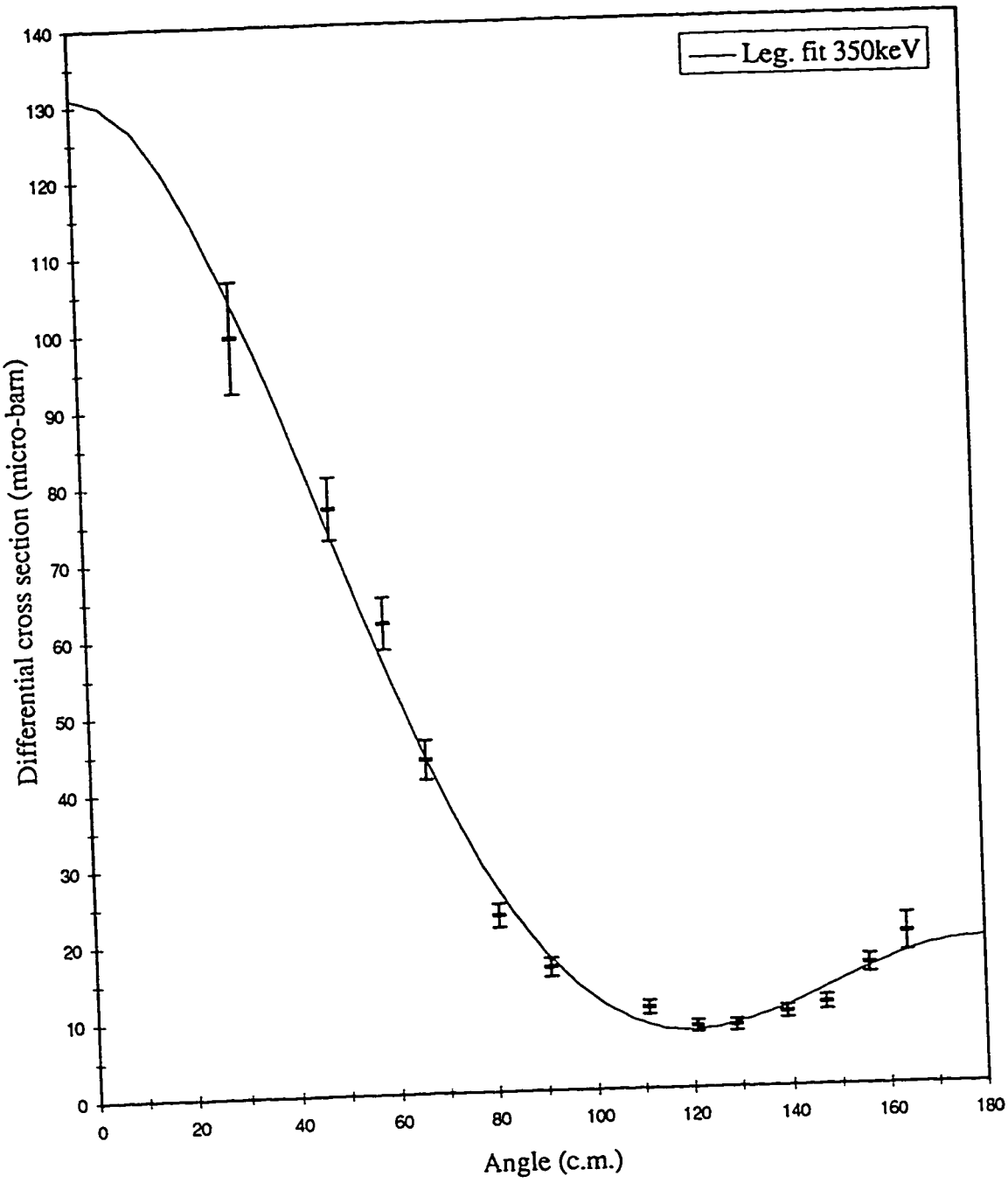

Figure 4.10 Fitted experimental data at $E_d = 350$ keV with five terms of Legendre polynomial.

was calculated using analytical (Eq. 4.8) and integral (Eq. 4.10) method, was found to be 453 ± 25 μb and 413 μb respectively. These values agree within the uncertainties.

Similarly total cross section $\sigma_{tot\text{-}exp}$ was calculated for 335, 310, 290, 270, 250 and 200 keV angular distribution individually using the Legendre polynomial fit. Table 4.3 shows the number of coefficients for the Legendre polynomial along with the total experimental cross section data. The values of coefficients of Legendre polynomials and that of χ^2 for each deuteron energy are listed in Table 4.4.

Table 4.3 Total experimental cross section.

	σ_{tot} (μb)	
E_d (keV)	curve integral	analytical
350	413	453 ± 25
335	299	328 ± 21
310	182	200 ± 16
290	128	140 ± 14
270	79	87 ± 10
250	46	50 ± 9
200	7	8 ± 4

Table 4.4 Coefficients of Legendre polynomials and χ^2 for deuteron energies.

	Coefficients of Legendre polynomials					
E_d (keV)	a_0	a_1	a_2	a_3	a_4	χ^2
350	36.0	51.2	37.3	4.9	1.6	0.34
335	26.1	36.8	27.4	5.1	1.9	0.29
310	15.9	22.7	15.3	2.1	0.1	0.11
290	11.2	15.8	9.8	1.4	0.1	0.17
270	6.9	9.9	6.2	0.9	-	0.07
250	4.0	5.7	3.4	0.5	-0.07	0.02
200	0.6	0.9	0.5	0.2	0.03	0.01

CHAPTER 5

ANALYSIS OF $^{13}C(d, p)^{14}C$ CROSS SECTION DATA

5.1 DWBA FORMALISM OF (d, p) REACTION

The distorted-wave Born approximation (DWBA) method of direct reaction has been successfully applied to analyze stripping (d, p) reactions [19]. In these reactions the projectile and target simply exchange nucleons without disturbing internal degrees of freedom of the system. In the direct reaction model of the form *A(d, p)B*, the reactions of interest result from direct coupling between the *d+A* and *p+B* channels, i.e. deuterons which are initially lost to any other configuration of the system (inelastic scattering, breakup, compound nucleus, etc.) do not couple back to the *p+B* channel.

Wave functions for the initial and final states of the system are postulated and a transition is allowed between the two configurations by making use of the Born approximation [20]. The motion of the deuterons in the elastic channel is described by an optical model potential and is used in a two-body Schrodinger equation to obtain a wave function χ_d for interaction of *d* with *A*. The complete wave function for the *d+A* system may thus be written in the form,

$$\psi_{dA} = \Phi_A(\xi)\phi_d(\mathbf{r}_{np})\chi_d(\mathbf{r}_{dA}) \tag{5.1}$$

where Φ_A and ϕ_d are the internal wave functions for the nucleus *A* and the deuteron respectively, r_{np} are the coordinates of neutron and proton in deuteron and r_{dA} are the

coordinates of the deuteron relative to the target nucleus. The symbol ξ represents all the internal coordinates of the nucleus *A*. The wave function for *p*+*B* channel may be written in an analogous manner as,

$$\psi_{pB} = \Phi_B(\xi, \mathbf{r}_{nA})\chi_p(\mathbf{r}_{pB}) \tag{5.2}$$

where Φ_B is the internal wave function of the residual nucleus (A+1) and χ_p is the proton optical model wave function which interacts with the residual nucleus. The residual nucleus is formed by capturing a neutron which is due to an approximation called the spectator approximation in which proton does not participate in the reaction.

The differential cross section of (d, p) reaction is proportional to the square of the transitional amplitude τ. For the (d, p) reaction τ is taken to be the matrix element of the appropriate transition potential between the initial and final states of the system. It can be obtained by making use of the DWBA as,

$$\tau = \int \left\langle \psi_{pB}^{(-)} | V | \psi_{dA}^{(+)} \right\rangle d\mathbf{r}_{nA} d\mathbf{r}_{pA} \tag{5.3}$$

where the matrix element implies integration over the coordinates ξ. The superscripts (±) on the wave functions refer to the choice of boundary conditions for the optical model wave functions. The transition potential is generally taken to be neutron-proton potential, V_{np} [19]. Thus we have,

$$\tau = \int \chi_p^{(-)^*}(\mathbf{r}_{pB}) \left\langle \Phi_B(\xi, \mathbf{r}_{nA}) \middle| \Phi_A(\xi) \right\rangle V_{np}(\mathbf{r}_{np}) \phi_d(\mathbf{r}_{np}) \chi_d^{(+)}(\mathbf{r}_{dA}) d\mathbf{r}_{pA} d\mathbf{r}_{nA} \tag{5.4}$$

It is this expression that one evaluates to obtain the transition amplitude in DWBA and where the matrix element is,

$$\left\langle \Phi_B^{M_B}(\xi, \mathbf{r}_{nA}) \middle| \Phi_A^{M_A}(\xi) \right\rangle \equiv \phi_n^*(\mathbf{r}_{nA}) = \sum \left\langle J_A M_A j_n m \middle| J_B M_B \right\rangle \alpha_{l_n j_n}^* \psi_{l_n j_n}^{m^*}(\mathbf{r}_{nA}) \tag{5.5}$$

where $\psi^{m}_{l_n j_n}$ is taken to be a normalized single particle wave function for a neutron which has orbital angular momentum l_n and total angular momentum j_n. Thus the quantity $\alpha_{l_n j_n}$ is a measure of the single particle purity of the state B. From Eq. 5.4 and Eq. 5.5 we see that the transition amplitude will be proportional to $\alpha_{l_n j_n}$ so that the DWBA cross section will be proportional to the spectroscopic factor, defined as $S = \left|\alpha_{l_n j_n}\right|^2$. For a (d, p) reaction the spectroscopic factor can range from 1 for a pure single particle state to zero for a state in which there is no single particle configuration.

The differential cross section is given in terms of the transition amplitude τ, by the relation [4],

$$\frac{d\sigma_{\beta}}{d\Omega} = \frac{\mu_{\alpha}\mu_{\beta}}{(2\pi\hbar^2)^2}\frac{k_{\beta}}{k_{\alpha}}|\tau|^2 \qquad (5.6)$$

where μ_α and μ_β are the reduced masses of entrance and exit channel's particles. k_α and k_β are the relative momenta of entrance and exit channel's particles and τ is the transition amplitude.

In addition to the wave functions for the initial and final states of the system, wave functions for light (n+p) and heavy (^{13}C+n) bound systems are also required to completely describe the picture of a transfer reaction. The bound systems are depicted in Figure 5.1 through vertex diagram for ^{13}C(d, p)^{14}C transfer reaction. At vertex 1 deuteron is stripped of its neutron which is then captured by the target nucleus ^{13}C at vertex 2 to form the residual nucleus ^{14}C. This encounter involves two form factors, one describing the transition of light bound system D $\rightarrow$ p+n at vertex 1, the other describing the transition of heavy bound system ^{13}C+n $\rightarrow$ ^{14}C at vertex 2. For the

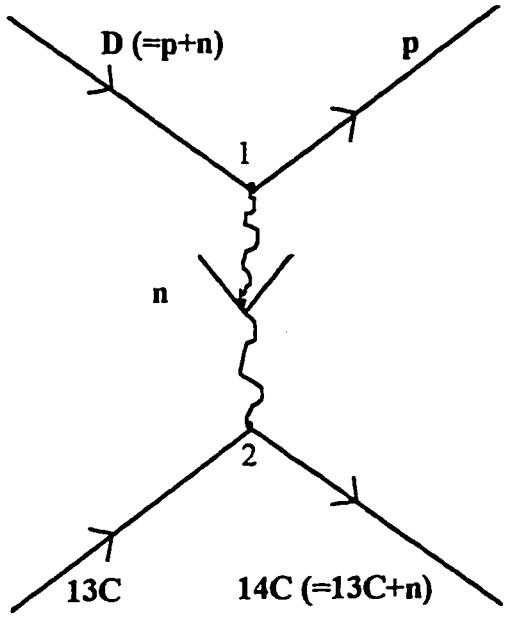

Figure 5.1 Vertex diagram of DWBA view for $^{13}C(d, p)^{14}C$ transfer reaction.

$^{13}C(d, p)^{14}C$ stripping reaction, form factors measure the degree of overlap of ^{14}C with the ^{13}C plus neutron [21].

5.2 COMPOUND NUCLEUS CONTRIBUTION IN $^{13}C(d, p)^{14}C$ REACTION

In the present study excitation functions and angular distributions of $^{13}C(d, p)^{14}C$ reaction have been measured for 200-350 keV deuteron energies. Within the experimental uncertainties, the excitation functions show that over this energy range the $^{13}C(d, p)^{14}C$ reaction does not have any resonance. Thus it was assumed the compound nucleus contribution was negligible in the energy range of 200-350 keV. In order to verify this, the compound nucleus contribution was estimated for the $^{13}C(d, p)^{14}C$ reaction at 200-350 keV deuteron energies by extrapolating the compound nucleus contribution data of $^{13}C(d, p)^{14}C$ reaction at 410-810 keV deuteron energies. The compound nucleus contribution in $^{13}C(d, p)^{14}C$ reaction at 410-810 keV energies, which was approximately isotropic was calculated using Hauser-Feshbach calculations [1]. Figure 5.2 shows the extrapolated curve down to 200 keV. The compound nucleus contribution in $^{13}C(d, p)^{14}C$ reaction at 200, 250, 270, 290, 310, 335 and 350 keV deuteron energies was estimated to be 1.2, 3.1, 4.2, 5.7, 7.4, 10.2, 12.2 μb/sr respectively. As compared to the total uncertainty (refer to Table 4.2) in the $^{13}C(d, p)^{14}C$ reaction cross section data at 200-350 keV, these compound nucleus contribution limit lies within the experimental uncertainty. Therefore for the nuclear model fit to the $^{13}C(d, p)^{14}C$ reaction cross section data compound nucleus contribution

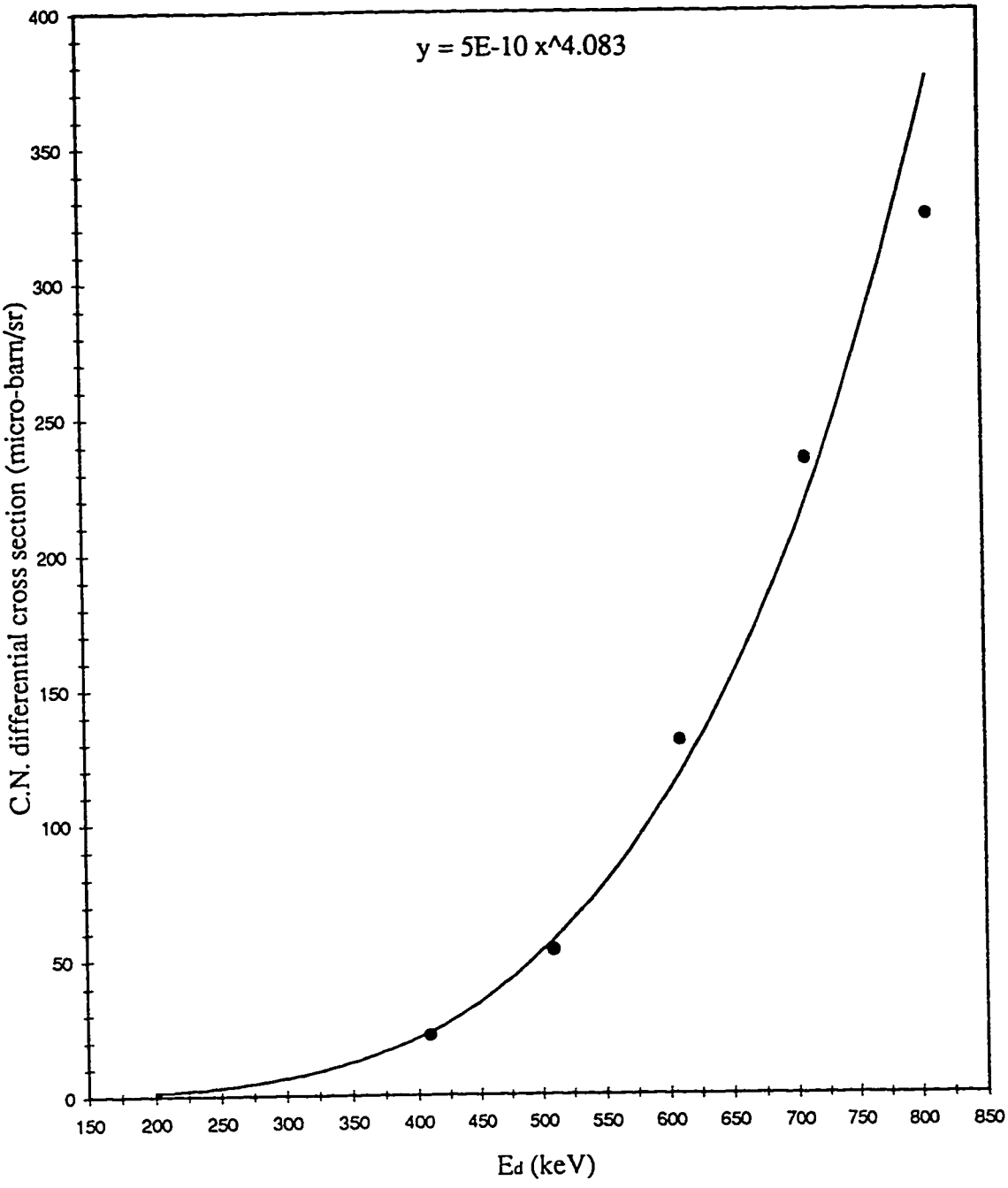

Figure 5.2 Extrapolated compound nucleus contribution in $^{13}C(d, p)^{14}C$ reaction.

was ignored and only direct reaction channel was assumed and data was fitted with a DWBA model code.

5.3 DESCRIPTION OF DWBA CODE 'TWOFNR'

DWBA calculations were carried out to calculate the differential cross section for the $^{13}C(d, p)^{14}C$ reaction using finite-range DWBA code TWOFNR [22]. TWOFNR has already been successfully used to calculate the differential cross section and analyzing power of transfer reactions [23,24] using one-step or two-step process of the reaction with zero or finite-range calculations. In one-step reaction, first order of DWBA is considered because the interaction is assumed to act only once and hence higher order of the approximation can be neglected. In a two-step process, coupling between the channels is strong and thus considering only the first order of approximation is inadequate. In zero-range calculations the point of emission of outgoing particle is the same as the point of interaction of incident particle with the target nucleus [25]. The code requires potential form factor parameters of light (n+p) and heavy (^{13}C+n) bound systems.

5.3.1 Input data to TWOFNR for $^{13}C(d, p)^{14}C$ reaction

The input data to the code consists of two parts namely, basic data and form factor data of heavy and light bound systems. Basic data of the input consist of numerical data of the reaction kinematics, Q-values and spin and angular momentum transfer for the one step process and optical model potentials for the entrance and exit

channels reactions. The optical potentials used in TWOFNR code are defined by,

$$U = -\left\{V_c f_c^{(R)}(r) + iW_c f_c^{(I)}(r)\right\} + 2\left(\frac{h}{m_\pi c}\right)^2 \frac{1}{r}\frac{\partial}{\partial r}\left\{V_{so} f_{so}^{(R)}(r) + iW_{so} f_{so}^{(I)}(r)\right\}(l.s)$$

$$+\begin{cases} \frac{1}{2R_c}\left(3-\frac{r^2}{R_c^2}\right)zZe^2; & r \le R_c \\ \frac{1}{r}zZe^2; & r > R_c \end{cases} \qquad (5.7)$$

where,

$$f_c^{(R)}(r) = \frac{1}{1 + \exp[(r - R_R)/a_r]}$$

$$f_c^{(I)}(r) = 4\exp(\frac{r - R_R}{a_i})\frac{1}{1 + \exp[(r - R_I)/a_i]}$$

$$f_{so}^{(R)}(r) = \frac{1}{1 + \exp[(r - R_{SR})/a_{sr}]}$$

$$f_{so}^{(I)}(r) = \frac{1}{1 + \exp[(r - R_{SI})/a_{si}]}$$

where $R_x = r_x A_T^{1/3}$, $f_c(r)$ and $f_{so}(r)$ are the form factors of central and spin-orbit potentials respectively. The suffices (R) and (I) refers the real and imaginary parts respectively.

In the second part of the input data the details of finite range form factor of light (n+p) and heavy (^{13}C+n) bound systems are given. They also require their respective wave functions and binding potentials. The type of reaction and its interaction potential can be selected in the control data of the form factor. In the numerical data of the form factor, the binding potentials and the quantum numbers, i.e. node, orbital angular momentum, total angular momentum, etc. are given as input for the heavy and light bound systems. The spectroscopic amplitude is also given as input parameter.

For the $^{13}C(d, p)^{14}C$ reaction, $^{13}C(d, d)^{13}C$ and $^{14}C(p, p)^{14}C$ were taken respectively as the entrance and exit elastic channel reactions. In the basic data it was assumed that the $^{13}C(d, p)^{14}C$ reaction was a one-step reaction. In order to calculate the angular momentum transfer in the one-step reaction, it was assumed that the ground state of ^{13}C (which has six protons and seven neutrons) is $1p_{1/2}$ state (an odd $1p_{1/2}$ neutron) which means $l = 1$ (p-state), $s = 1/2$ and $j^{\pi} = 1/2^-$. The ^{14}C, expected to be formed by adding a neutron in a $1p_{1/2}$ state of ^{13}C, has $l = 1$ (p-state), $s = 1/2$ and $j^{\pi} = 0^+$ (even-even nuclei). Thus the orbital angular momentum, spin and total angular momentum transferred are 0, 1/2 and 1/2 respectively.

The number of partial waves contributing to the reaction was taken to be 16. The mixing factor of volume and surface parts of imaginary potentials in the exit channel was taken to be 1 and the Q-value relative to the incident channel was taken as 5.947 MeV. Also the kinematics for the entrance channel $^{13}C(d, d)^{13}C$ and that for the exit channel $^{14}C(p, p)^{14}C$ were given in the input. The optical model potential for entrance and exit elastic channel reactions along with their geometrical parameters were taken initially from Perey and Perey data for 13.7 and 14.5 MeV energies respectively [25].

In the control data of the finite range form factor data, the bound state wave functions of heavy (^{13}C+n) and light (n+p) bound systems were calculated using a Wood-Saxon type potential. The depth of the binding potential was searched by the code itself. The deuteron wave function was chosen such that the value of the parameter D_o^2, a measure of D/S state ratio, was assumed to be 1.018×10^{-4} MeV^2 fm^3.

The input value of the spectroscopic amplitude which was the square root of the value of spectroscopic factor given by Putt [1] was taken as 1.47. The quantum number e.g. node n, the orbital angular momentum *l* and the total angular momentum *j* of the heavy bound system were taken to be 0, 1 and 0 while for the light bound system they were taken to be 0, 0 and 1 respectively. The spin of the transferred neutron was assumed to be 0.5 and the range of the interaction was taken as 1.50 fm. The binding energies of the heavy (^{13}C+n) and light (n+p) bound systems in the ^{13}C(d, p)^{14}C reaction were taken to be 4.946 and 2.224 MeV respectively. Appendix D shows a typical listing of the input file of the TWOFNR code.

5.4 DWBA FIT TO THE ^{13}C(d, p)^{14}C REACTION DATA

The DWBA analysis of ^{13}C(d, p)^{14}C reaction cross section requires optical model potential (OMP) parameters for entrance and exit elastic channel. The OMP data of ^{13}C(d, p)^{14}C reaction was available at 410-810 keV and was published by Putt [1]. There were some questions about the OMP parameters used by Putt because he had analyzed ^{13}C(d, p)^{14}C reaction cross section data using OMP parameters of ^{13}C(d, n) reaction which were derived from ^{11}B(d, n) reaction potentials assuming mass independence of optical model potential parameters. The other reservation was about the significantly small values of some of the geometry parameters of the OMP potentials in Putt's data. Also DWBA fit to Putt's data does not reproduce the amplitude and shape feature of cross section at backward angles. The calculated cross sections are higher and at backward angles do not reproduce the curvature in the cross section curves above 120°. Putt used significantly small values of diffuseness' of real,

surface-imaginary and spin-orbit potentials in the exit channel. In particular the diffuseness of the spin-orbit potential was so small that the TWOFNR code did not run. It was decided to take $^{13}C(d, p)^{14}C$ reaction data from higher energy data and optimized them to fit present experimental data. Therefore the OMP parameters were taken from Perey and Perey for $^{13}C(d, d)^{13}C$ and $^{14}C(p, p)^{14}C$ reaction at 13.7 and 14.5 MeV respectively [26] and were used as entrance and exit elastic channel data. Since the entrance and exit elastic channel data was taken from higher energies, the parameters were optimized to have the best fit for $^{13}C(d, p)^{14}C$ cross section data at 350 keV.

The OMP parameters were optimized using the $^{13}C(d, p)^{14}C$ reaction cross section data at 350 keV. This energy data was chosen due to smaller uncertainties. Also its comparison with Putt data is easier because it is the nearest energy data to the Putt data. Figure 5.3 shows the calculated $^{13}C(d, p)^{14}C$ cross section using the original Perey and Perey OMP data along with the 350 keV experimental data. The calculated cross section is higher at all the angles. The χ^2 for this fit was 1708.

In the OMP parameter optimization process, first the potential depth was varied to minimize the χ^2 and then its geometrical parameters i.e. radius and diffuseness were varied to further minimize the χ^2. In the following text both steps will be referred to as potential optimization. First real potential in the entrance channel was optimized and then in the exit channel. It was followed by optimization of surface imaginary potential in the entrance and then in the exit channel. In a similar manner

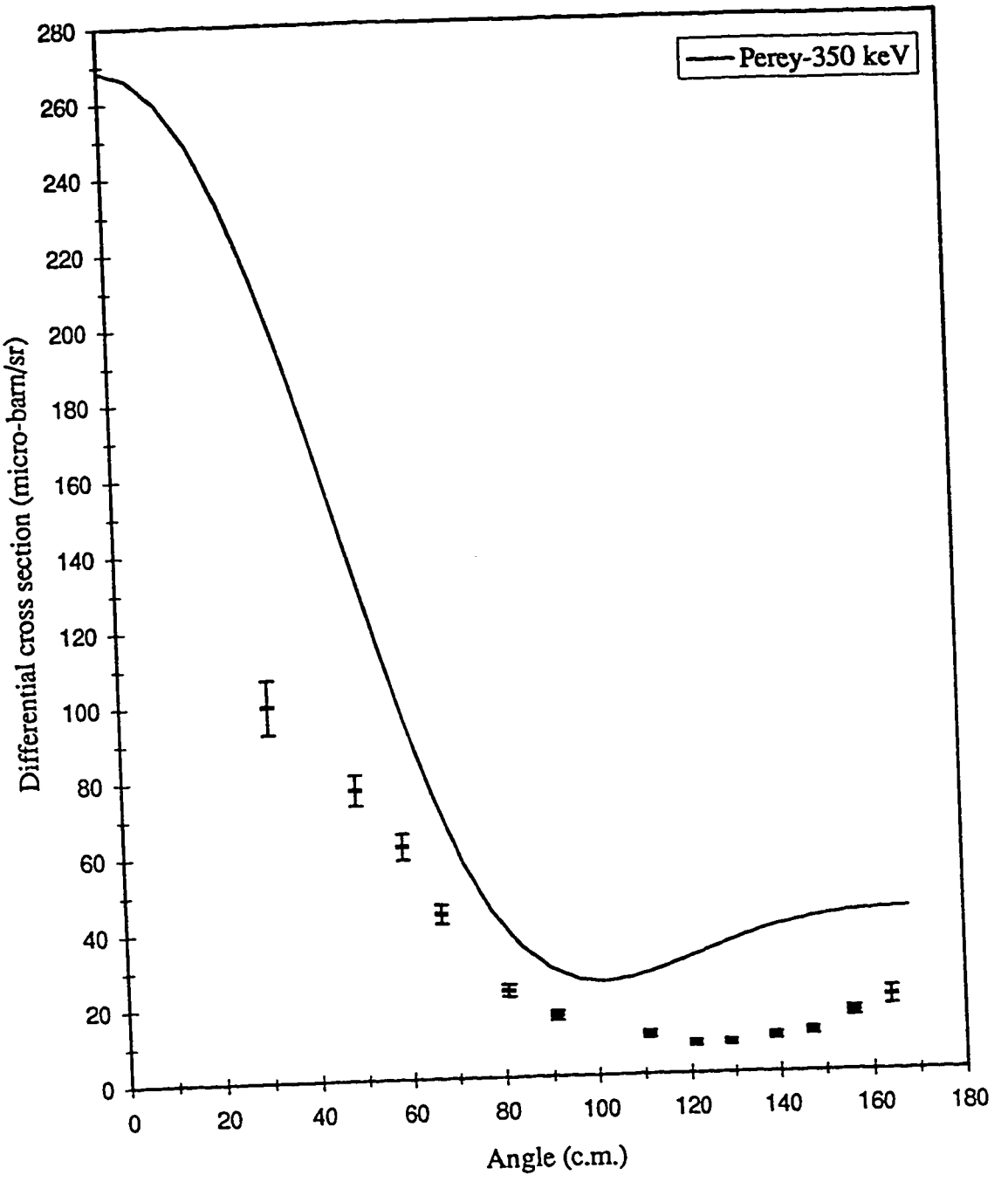

Figure 5.3 Calculated $^{13}C(d, p)^{14}C$ cross section from original Perey [26] OMP parameters at $E_d = 350$ keV.

spin-orbit potential was optimized in entrance and exit channel to obtain minimum value of χ^2.

The optimization of each OMP parameter was carried out by varying them over a range covering the values of Perey and Putt. Table 5.1 shows the OMP parameters optimum values, range of optimization and χ^2 along with Perey [26] initial data. In order to test the convergence of χ^2, optimization was carried twice. Results of the second run of optimization are also included in the table. As a example, Figure 5.4 shows the minimized χ^2 as a function of a_v in the entrance channel. The solid line indicates the first run and dashed line indicates the second run. Figure 5.5 shows the optimized DWBA fit for the $^{13}C(d, p)^{14}C$ reaction cross section after the two runs of minimization of χ^2. Two points are quiet noticeable. The calculated cross section curve passes through most of the experimental data points and it reproduces the increasing cross section at backward angle. Second feature is the flat cross section around 0°. Also the real potential V (= 30 MeV) in the exit channel was abnormally small. Adjustment of the potential parameters were required to have a reasonable value of V in the exit channel and to reduce the flatness of the curve around 0°.

To achieve this, V in the entrance channel was reduced by 5% and in the exit channel it was adjusted to 51.5V, a value close to Putt and Perey. Further the W in the entrance and exit channels were increased by 30% and 16% respectively. The V_{so} in the entrance channel was also increased by 100% to make it consistent with the value given by Putt and Perey. The geometrical parameters r_w, a_w, r_{so} in the entrance channel and r_v in the exit channel were increased by 2.5%, 10%, 20% and 5.8% respectively. Total calculated

Table 5.1 OMP parameters optimum values by minimizing the χ^2.

			First iteration					
	Perey [26]		Entrance channel			Exit channel		
OMP	ent.	Exit	range	optim. value	χ^2	range	optim. Value	χ^2
V (MeV)	100.5	63.0	92-108	100.0	1693.2	30-63	30.00	94.9
r (fm)	1.00	1.13	1.4-1.55	1.47	609.8	1.13-1.4	1.23	56.5
a (fm)	0.80	0.65	0.65-0.88	0.77	553.6	0.65-0.9	0.77	20.7
W (MeV)	5.04	9.70	3.8-7.2	5.50	17.6	8.0-16.0	11.70	15.8
r_w (fm)	2.00	1.13	1.85-2.15	2.00	17.6	0.8-1.4	1.13	15.8
a_w (fm)	0.60	0.51	0.45-0.8	0.60	17.6	0.31-0.66	0.51	15.8
V_{so} (MeV)	5.32	7.50	2.0-6.5	3.32	12.5	3.5-9.5	7.50	12.5
r_{so} (fm)	1.00	1.13	0.5-2.5	1.00	12.5	0.7-1.43	1.03	11.8
a_{so} (fm)	0.80	0.65	0.2-0.97	0.80	12.5	0.3-0.95	0.55	11.4
			Second iteration					
	Perey [26]		Entrance channel			Exit channel		
OMP	ent.	Exit	range	optim. value	χ^2	range	optim. value	χ^2
V (MeV)	100.5	63.0	94-106	100.0	11.4	29.5-45.0	30.0	11.4
r (fm)	1.00	1.13	1.4-1.55	1.47	11.4	1.15-1.35	1.23	11.4
a (fm)	0.80	0.65	0.72-0.82	0.77	11.4	0.65-0.90	0.77	11.4
W (MeV)	5.04	9.70	4.4-6.8	5.4	11.3	0.9-16.5	12.50	10.8
r_w (fm)	2.00	1.13	1.9-2.15	2.0	11.3	0.9-1.35	1.11	10.7
a_w (fm)	0.60	0.51	0.5-0.7	0.6	11.3	0.35-0.65	0.53	10.5
V_{so} (MeV)	5.32	7.50	2.0-5.0	3.0	10.2	4.0-9.0	7.50	10.2
r_{so} (fm)	1.00	1.13	1.0-1.7	1.0	10.2	0.9-1.4	1.03	10.2
a_{so} (fm)	0.80	0.65	0.5-0.95	0.8	10.2	0.3-0.85	0.55	10.2

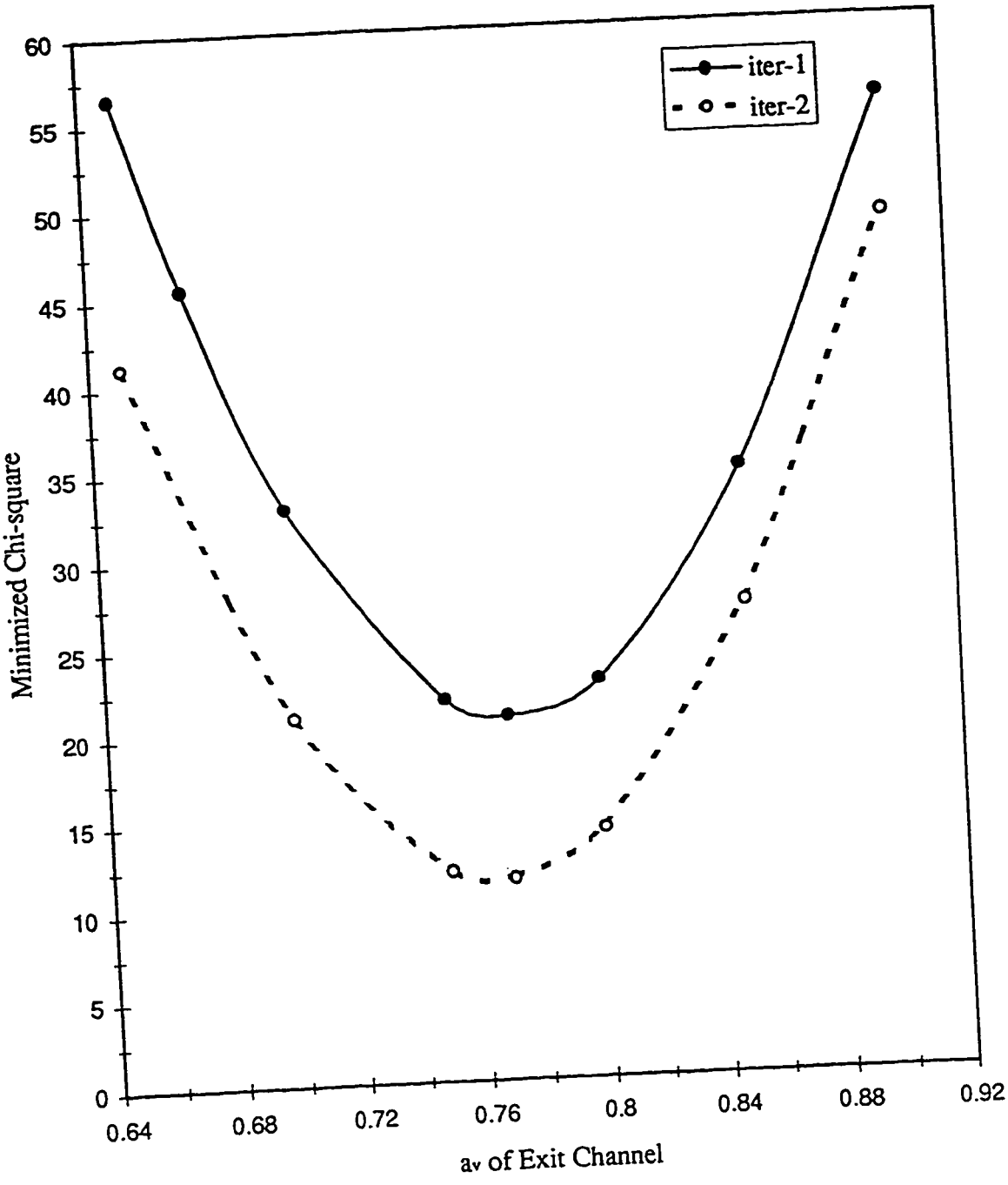

Figure 5.4 Typical graph showing minimized χ^2 as a function of OMP parameter a_v of exit channel.

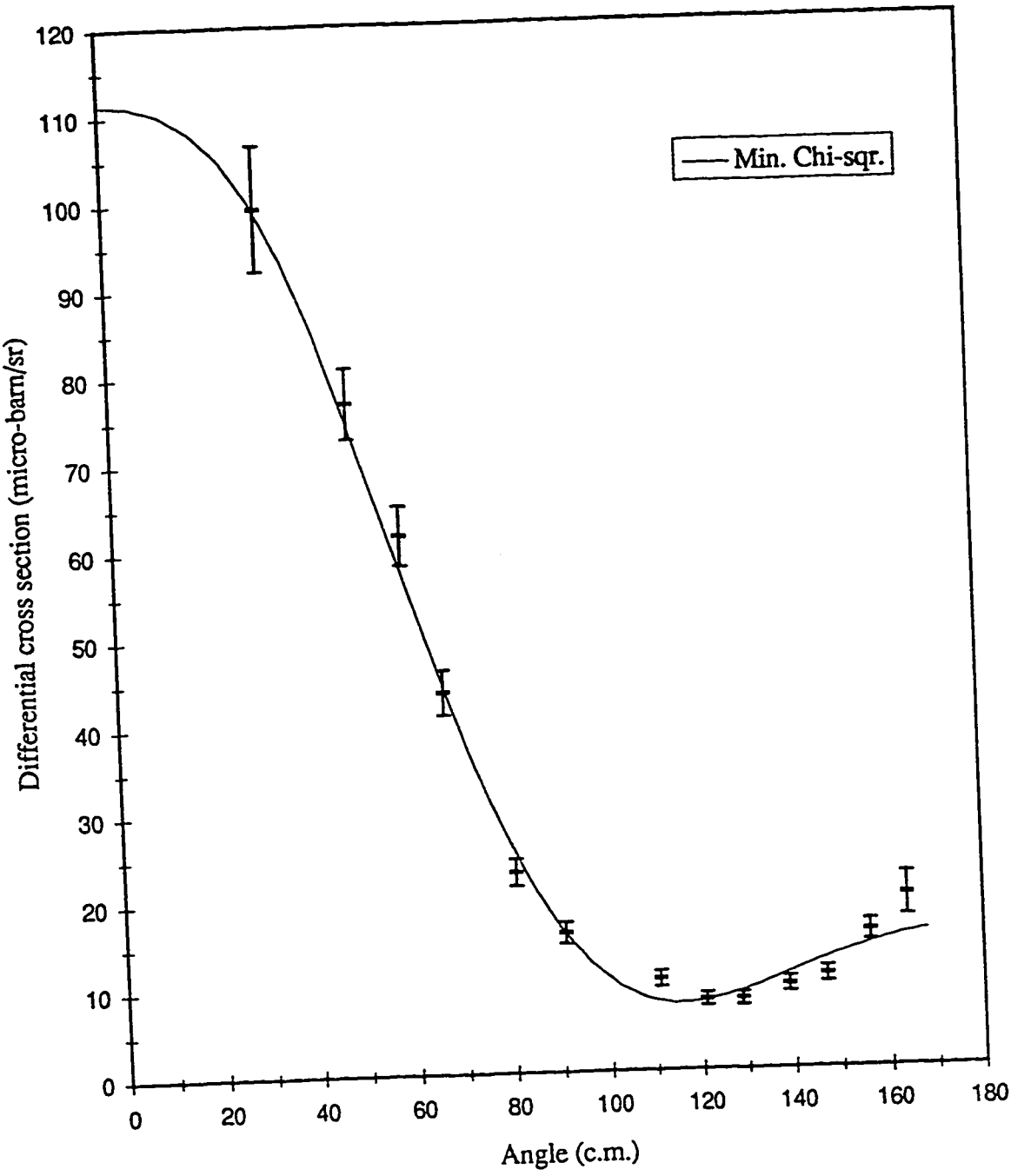

Figure 5.5 Optimized DWBA fit to 350 keV deuteron energy for $^{13}C(d, p)^{14}C$ reaction after minimizing the χ^2, with $\chi^2 = 10.2$.

calculated reaction cross section at 350 keV deuteron energy was calculated to be 435 μb which is in agreement with the experimental total reaction cross section of 453 ± 25 μb at the same deuteron energy.

Figure 5.6 shows the best fit to 350 keV deuteron energy in the present work. The error bars includes statistical as well as systematic uncertainty. Once the best fit at 350 keV was achieved, the same optical parameters were used to obtain the fit to cross section data at 335, 310, 290, 270, 250 and 200 keV deuteron energies. Figures 5.7-5.12 show the fitted cross section to experimental data at 335-200 keV. The calculated total cross section σ_{theo} and experimental total cross section σ_{exp} for 350-200 keV along with χ^2 are listed in Table 5.2. It can be seen that the σ_{exp} and σ_{theo} agree within the experimental uncertainties.

The final optimized OMP parameters are listed in Table 5.3 along with Perey [26] and Putt [1] data. Comparison of present data with the Putt data reveals that the abnormality in the diffuseness of V, W, and V_{so} in the exit channel data of Putt is removed. The diffuseness parameters of V, W and V_{so} are 0.77 fm, 0.53 fm and 0.55 fm respectively, which are comparable to the values of Perey. Although the Perey data are for higher energies, it can be taken as a reference because the geometrical parameters are energy independent. In the entrance channel the diffuseness a_w in the present work is lower by 33% than that of Putt but again agree with the Perey value within 10%. The radius r_w in the entrance channel is higher than that of Putt by 64% but agrees with that of Perey value. The V in the entrance channel in the present work is higher by 20% while the W in both the entrance and exit channels are lowered by 28 % reflecting low

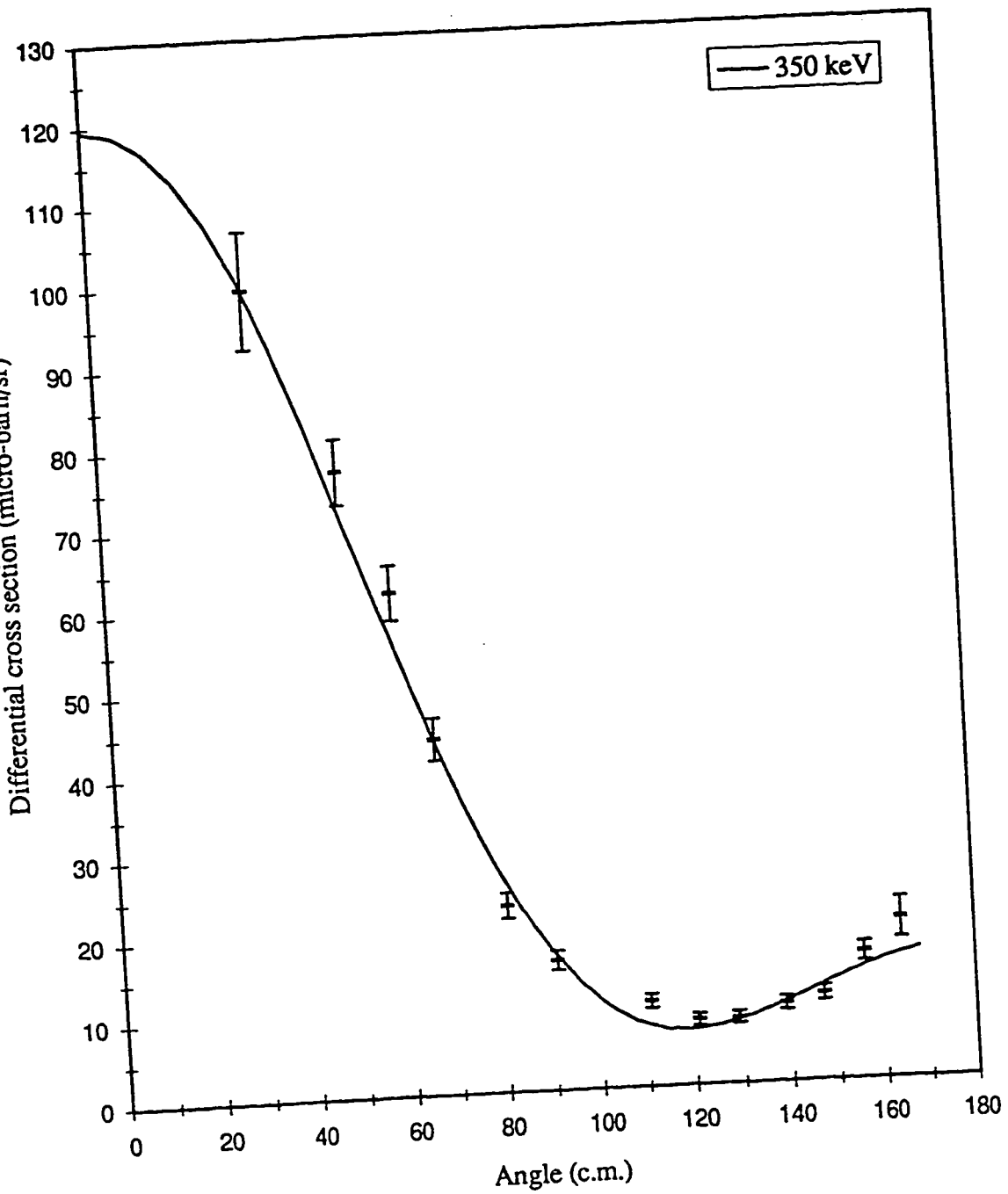

Figure 5.6 Optimized DWBA fit to E_d = 350 keV for $^{13}C(d, p)^{14}C$ reaction with $\chi^2 = 12.6$.

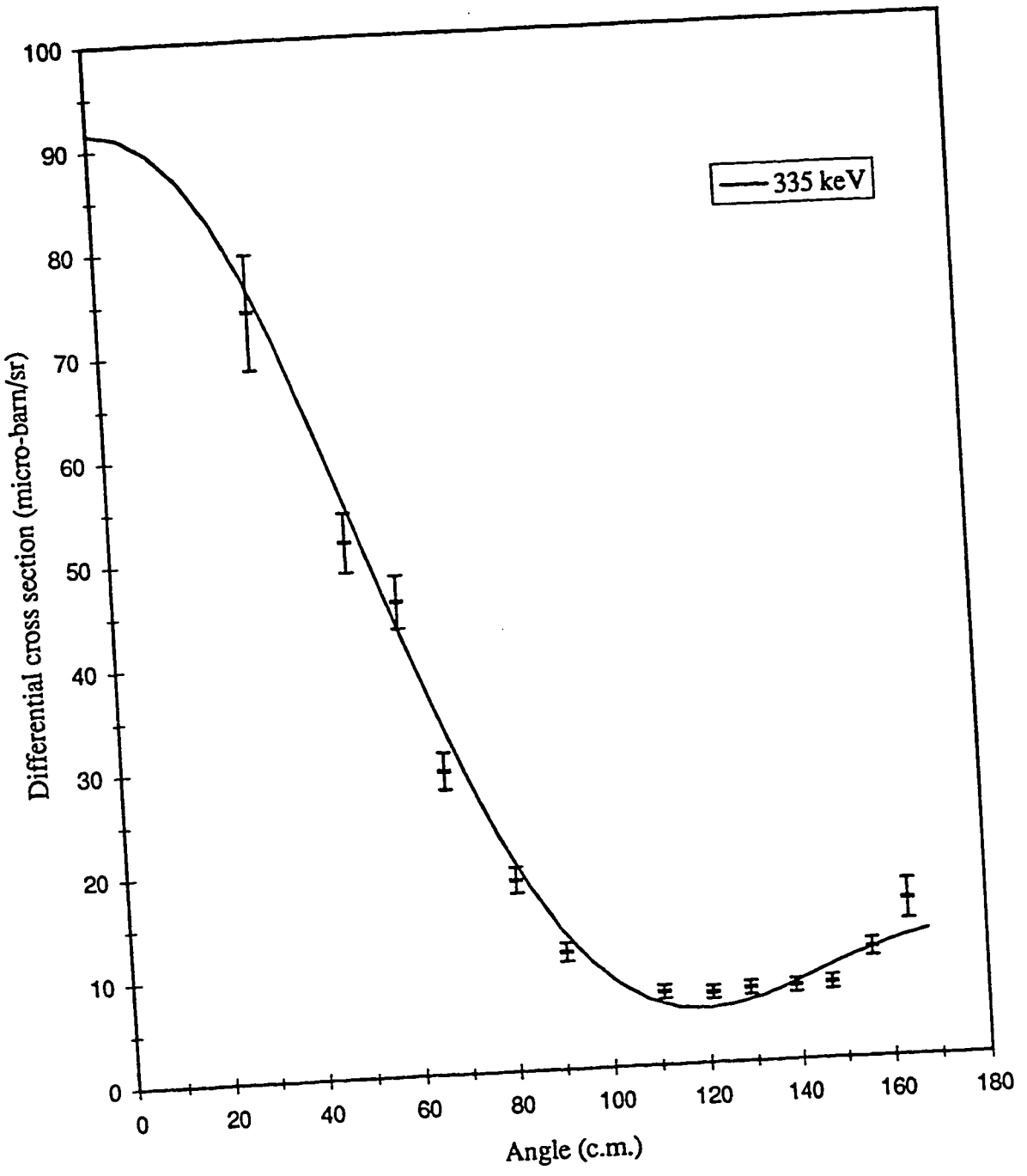

Figure 5.7 Optimized DWBA fit to $E_d = 335$ keV for $^{13}C(d, p)^{14}C$ reaction with $\chi^2 = 10.6$.

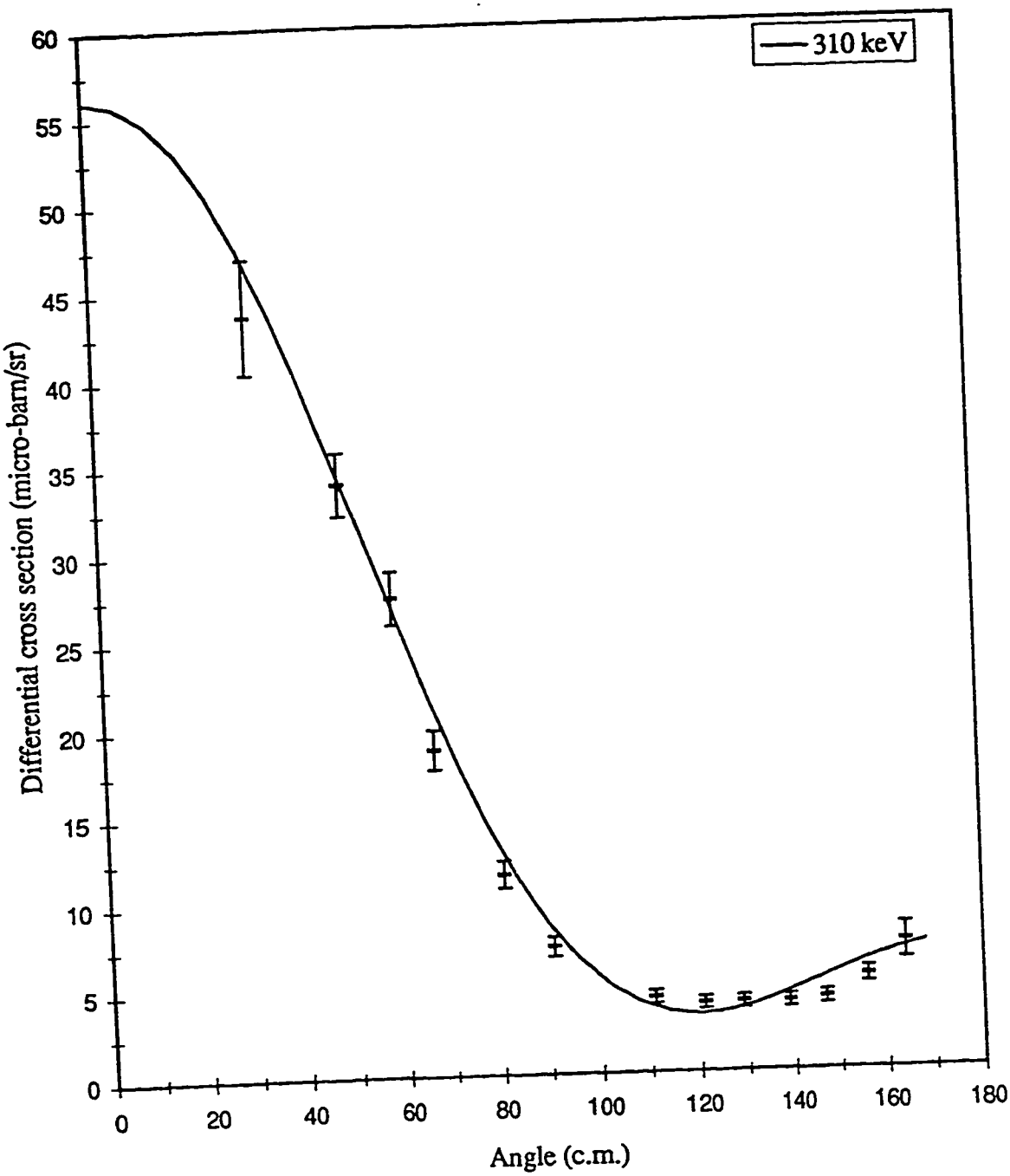

Figure 5.8 Optimized DWBA fit to $E_d = 310$ keV for $^{13}C(d, p)^{14}C$ reaction with $\chi^2 = 9.7$.

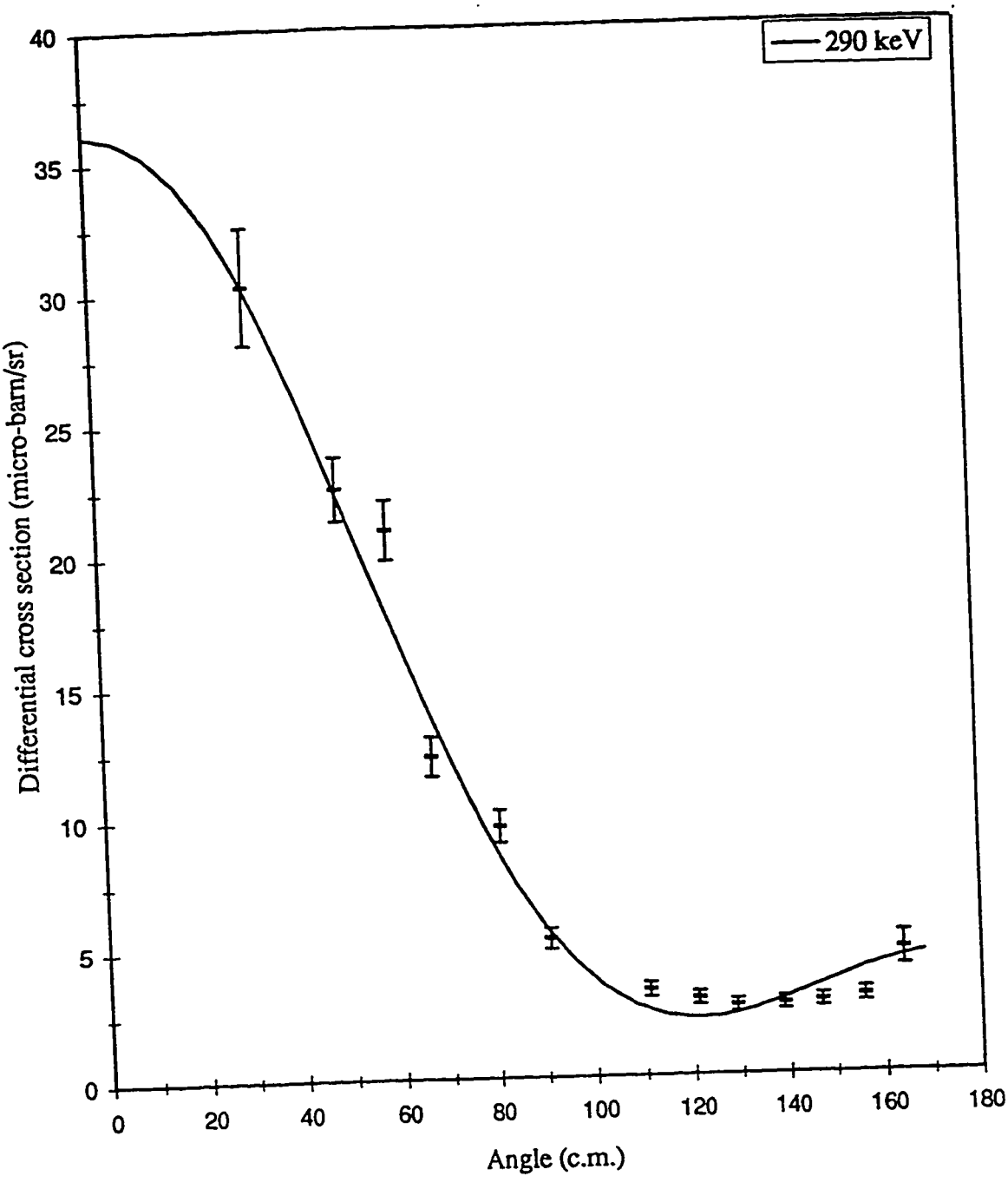

Figure 5.9 Optimized DWBA fit to $E_d = 290$ keV for $^{13}C(d, p)^{14}C$ reaction with $\chi^2 = 12.6$.

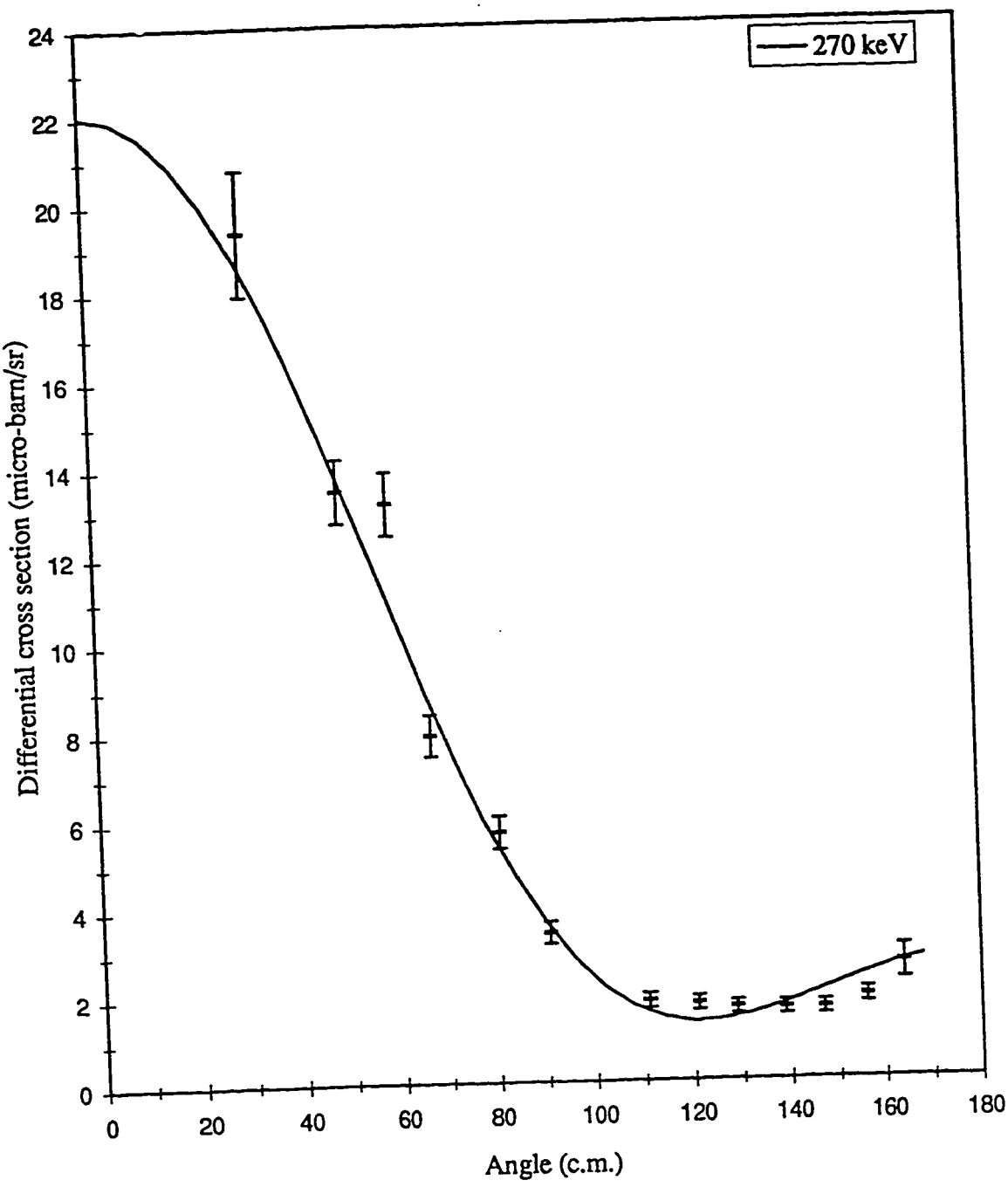

Figure 5.10 Optimized DWBA fit to $E_d = 270$ keV for $^{13}C(d, p)^{14}C$ reaction with $\chi^2 = 5.7$.

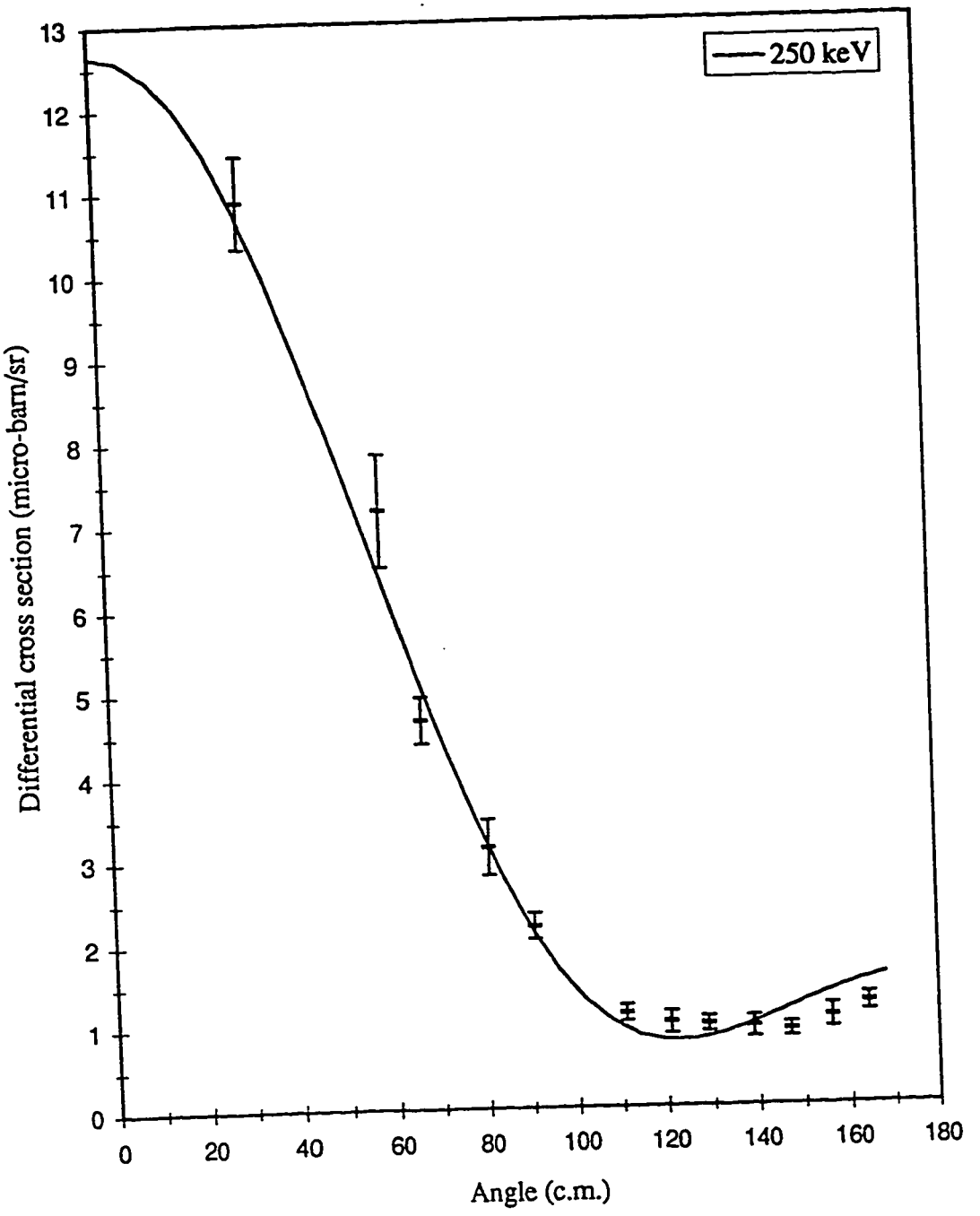

Figure 5.11 Optimized DWBA fit to $E_d = 250$ keV for $^{13}C(d, p)^{14}C$ reaction with $\chi^2 = 7.3$.

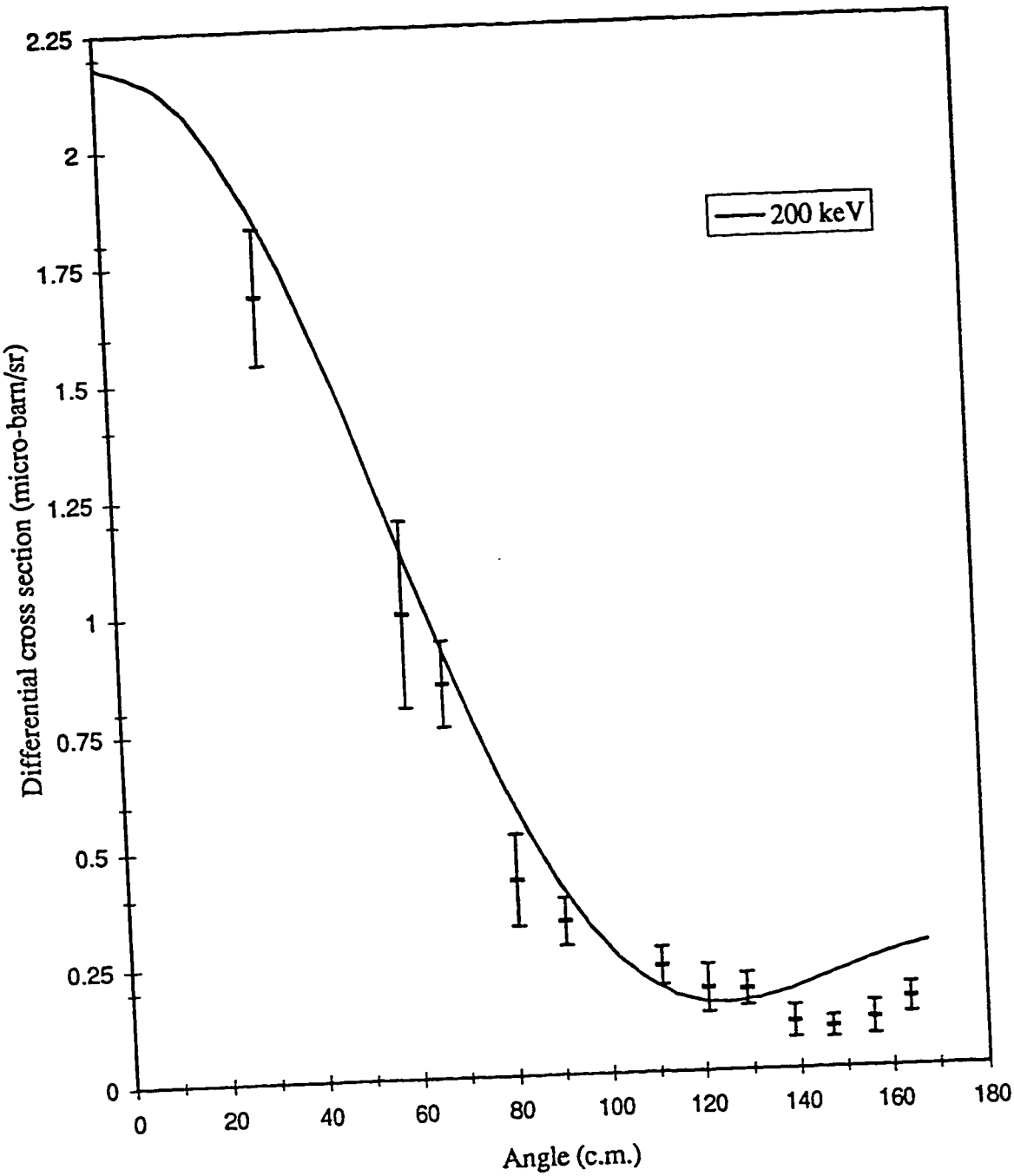

Figure 5.12 Optimized DWBA fit to $E_d = 200$ keV for $^{13}C(d, p)^{14}C$ reaction with $\chi^2 = 7.3$.

Table 5.2 Experimental and calculated total cross section along with values of χ^2.

	σ_{tot} (μb)		
E_d (keV)	σ_{exp}	σ_{theo}	χ^2
350	453 ± 25	435.0	12.6
335	328 ± 21	335.8	10.6
310	200 ± 16	208.4	9.7
290	140 ± 14	135.6	12.6
270	87 ± 10	83.9	5.7
250	50 ± 9	48.8	7.3
200	8 ± 4	8.7	7.3

Table 5.3 OMP parameters for $^{13}C(d, p)^{14}C$ reaction.

	Perey [26]		Present work		Putt [1]	
OMP parameters	**Entrance channel**	**Exit channel**	**Entrance channel**	**Exit channel**	**Entrance channel**	**Exit channel**
V (MeV)	100.5	63.0	95.0	52.0	79.50	51.50
r (fm)	1.00	1.13	1.47	1.30	1.25	1.30
a (fm)	0.80	0.65	0.77	0.77	0.80	0.34
W (MeV)	5.04	9.70	7.03	14.50	10.00	19.20
r_w (fm)	2.00	1.13	2.05	1.11	1.25	1.30
a_w (fm)	0.60	0.51	0.54	0.53	0.80	0.125
V_{so} (MeV)	5.32	7.50	6.00	7.50	6.00	6.00
r_{so} (fm)	1.00	1.13	1.20	1.03	1.25	1.30
a_{so} (fm)	0.80	0.65	0.80	0.55	0.80	0.34
r_c (fm)	1.50	1.25	1.50	1.25	1.25	1.25

absorption in the present study. It is understandable because at lower deuteron energy loss of deuteron flux from other than direct channel is negligible. The V_{so} in both the channels are comparable with Putt [1] and Perey [26] values.

CHAPTER 6

SUMMARY AND CONCLUSION

Excitation functions and angular distributions of $^{13}C(d, p)^{14}C$ reaction were measured for 200-350 keV deuterons as no data was available for this energy range. This data helped us to learn about the disagreement between the cross section data of the reaction and DWBA calculations at 410-810 keV deuteron energies. Assuming that the nuclear effects do not show change significantly over a small change in deuteron energy from 410 to 350 keV, it was expected that the data obtained in the present study will shed some light on the above mentioned disagreement at 410-810 keV energy. Furthermore data of this study would be used in the measurements of analyzing powers of $^{13}C(d, p)^{14}C$ reaction.

The excitation functions for the $^{13}C(d, p)^{14}C$ reaction were measured at 30°, 48°, 66°, 90°, 110°, 128°, 146° and 164° for 200, 250-350 keV deuterons in 10 keV steps. Within the statistical uncertainties the excitation functions did not show resonance structure. Thus compound nucleus contribution is excluded at these energies. All the excitation functions show smoothly increasing trend with the deuteron energies.

Differential cross section of the $^{13}C(d, p)^{14}C$ reaction were measured at of 200, 250, 270, 290, 310, 335 and 350 keV deuteron energies over an angular range of 30°-165° in 10° steps. Contrary to backward peaking trend of angular distribution

of transfer reaction at sub-Coulomb barrier energies, the angular distribution of $^{13}C(d, p)^{14}C$ reaction is forward peaked for 200-350 keV deuteron energies. The forward peaking of the angular distribution of $^{13}C(d, p)^{14}C$ reaction at sub-Coulomb barrier energies is due to large Q-value of the reaction. This results in kinetic energy of the emitted particle in excess of Coulomb barrier energy. Therefore the emitted particle moves in forward direction without being deflected much by the Coulomb force. The ratio of maximum to minimum cross section for each angular distribution is about ten. This indicates that although cross section decreases with energy but its shape remains the same. The angular distributions trends are consistent with the results of Putt reported for 410-810 keV deuteron energies.

The differential cross section was calculated using DWBA finite range approximation. There is a good agreement between calculated and experimental $^{13}C(d, p)^{14}C$ reaction cross section data. Also a good agreement between the total experimental and theoretical cross section has been achieved. Compared to Putt's data at 410-810 keV deuteron energies, a better agreement has been achieved in the present study between the calculated and experimental data at backward angles. It should be noted that more reasonable values of diffuseness of real, imaginary and spin orbit potentials in exit channel have been obtained as compared to those reported by Putt for 410-810 keV data. These DWBA calculations can be used to determine vector and tensor analyzing power of $^{13}C(d, p)^{14}C$ reaction below 350 keV deuteron energies.

Appendix A

LISTING OF DATA ACQUISITION PROGRAM FILES

MDET.COM

```
$ PUT 1
$ CL FLAGS
$ STOP XBOXSP
$ DMEN ALL
$ AMEN 1 1024 I*4 1D DET1
$ AMEN 2 1024 I*4 1D DET2
$ AMEN 3 1024 I*4 1D DET3
$ AMEN 4 1024 I*4 1D DET4
$ AMEN 5 1024 I*4 1D DET5
$ AMEN 6 1024 I*4 1D DET6
$ AMEN 7 1024 I*4 1D DET7
$ AMEN 8 1024 I*4 1D DET8
$ GATE NEW
$ GATE 1 5
$ GATE 2 5
$ GATE 3 5
$ GATE 4 5
$ GATE 5 5
$ GATE 6 5
$ GATE 7 5
$ GATE 8 5
$ CLEAR ALL
$ GATE SET 1 1 1 1000
$ GATE SET 1 2 1 1000
$ GATE SET 1 3 1 1000
$ GATE SET 1 4 1 1000
$ GATE TRAN 1 2
$ GATE TRAN 1 3
$ GATE TRAN 1 4
$ GATE TRAN 1 5
$ GATE TRAN 1 6
$ GATE TRAN 1 7
$ GATE TRAN 1 8
$ SCAL NEW
$ SCAL HEAD 1 Preset Run. No. Rem. Pset% Cur. Pset
$ SCAL NUMB 1 11 1 2 3 LR2551
$ SCAL NUMB 1 12 1 REGISTER
$ EVOP SE MDET
$ SCAL SE SCLR
$ STOP XBOXSP
```

```
$ ASSIGN/GROUP  TXA5 :  SD
$ @boxset
$ FOR  BOXUSR
$ BOXLINK
$ DELETE  *.OBJ;*
$ SCAL CLEAR ALL
$ SCAL READ ALL
$ WRITE  SYS$OUTPUT  "  MULTI DETECTOR DATA ACQ. RUNNING  "
```

MDET.DAP

```
MDET
0
1000
INIT
1  28  9  26
1  28  8  26
1  30  10  26
1  1  0  16  1024
1  1  0  26
1  2  0  16  1024
1  2  0  26
1  3  0  16  1024
1  3  0  26
1  4  0  16  1024
1  4  0  26
1  6  0  16  1024
1  6  0  26
1  8  0  16  1024
1  8  0  26
1  14  0  16  1024
1  14  0  26
1  16  0  16  1024
1  16  0  26
1  20  1  0
LAM
1  20  0  0
1  1  0  2
1  2  0  2
1  3  0  2
1  4  0  2
1  6  0  2
1  8  0  2
1  14  0  2
1  16  0  2
1  20  1  0
END
```

MDET.EVL

```
SPEC  S1  1
SPEC  S2  2
SPEC  S3  3
SPEC  S4  4
SPEC  S5  5
SPEC  S6  6
SPEC  S7  7
SPEC  S8  8
C
DATA EVSIZE  10
C
FORMAT  F  1  3  1
FORMAT  F1  2  10  1
FORMAT  F2  3  10  1
FORMAT  F3  4  10  1
FORMAT  F4  5  10  1
FORMAT  F5  6  10  1
FORMAT  F6  7  10  1
FORMAT  F7  8  10  1
FORMAT  F8  9  10  1
C
GET  ROUT  F
IF  ROUT  EQ  0
GET  F1
INC  S1
  ELSE
  IF  ROUT  EQ  1
  GET  F2
  INC  S2
    ELSE
    IF  ROUT  EQ  2
    GET  F3
    INC  S3
      ELSE
      IF  ROUT  EQ  3
      GET  F4
      INC  S4
        ELSE
        IF  ROUT  EQ  4
        GET  F5
        INC  S5
```

```
            ELSE
            IF ROUT EQ 5
            GET F6
            INC S6
              ELSE
              IF ROUT EQ 6
              GET F7
              INC S7
                ELSE
                IF ROUT EQ 7
                GET F8
                INC S8
ENDIF
ENDIF
ENDIF
ENDIF
ENDIF
ENDIF
ENDIF
ENDIF
END
```

Appendix B

EXCITATION FUNCTION DATA OF $^{13}C(d, p)^{14}C$ REACTION

Table B-1 Excitation function data for $^{13}C(d, p)^{14}C$ reaction in lab. system at 30° lab. angle. Total error consists of statistical and systematic errors.

E_d (keV)	$d\sigma / d\Omega$ (μb)	Statistical Error (μb)	Total Error (μb)
200	1.68	0.09	0.15
250	10.88	0.17	0.61
260	13.85	0.61	1.17
270	19.34	0.75	1.53
280	23.02	0.80	1.72
290	30.27	1.19	2.40
300	34.42	1.00	2.38
310	43.64	1.76	3.51
327	71.15	1.53	4.38
335	73.92	2.98	5.93
340	91.26	1.79	5.44
350	99.34	3.73	7.70

Table B-2 Excitation function data for $^{13}C(d, p)^{14}C$ reaction in lab. system at 48° lab. angle. Total error consists of statistical and systematic errors.

E_d (keV)	$d\sigma / d\Omega$ (μb)	Statistical Error (μb)	Total Error (μb)
200	-	-	-
250	-	-	-
260	10.59	0.53	0.96
270	13.45	0.26	0.80
280	17.55	0.70	1.40
290	22.49	0.42	1.32
300	23.81	0.83	1.78
310	33.92	0.64	2.00
327	67.40	1.49	4.18
335	51.36	1.03	3.09
340	76.83	1.62	4.70
350	76.71	1.37	4.44

Table B-3 Excitation function data for $^{13}C(d, p)^{14}C$ reaction in lab. system at 66° lab. angle. Total error consists of statistical and systematic errors.

E_d (keV)	$d\sigma / d\Omega$ (μb)	Statistical Error (μb)	Total Error (μb)
200	0.84	0.06	0.10
250	4.65	0.11	0.30
260	6.03	0.40	0.64
270	7.88	0.20	0.52
280	9.99	0.52	0.92
290	12.25	0.32	0.81
300	13.92	0.62	1.18
310	18.67	0.48	1.23
327	28.15	0.92	2.05
335	29.06	0.78	1.94
340	35.53	1.05	2.47
350	43.55	1.04	2.78

Table B-4 Excitation function data for $^{13}C(d, p)^{14}C$ reaction in lab. system at 90° lab. angle. Total error consists of statistical and systematic errors.

E_d (keV)	$d\sigma / d\Omega$ (μb)	Statistical Error (μb)	Total Error (μb)
200	0.33	0.04	0.05
250	2.18	0.08	0.17
260	3.63	0.31	0.46
270	3.37	0.13	0.27
280	5.97	0.40	0.64
290	5.27	0.21	0.42
300	8.33	0.48	0.81
310	7.31	0.30	0.60
327	15.53	0.67	1.29
335	11.19	0.49	0.94
340	18.90	0.75	1.51
350	15.91	0.63	1.27

Table B-5 Excitation function data for $^{13}C(d, p)^{14}C$ reaction in lab. system at 110° lab. angle. Total error consists of statistical and systematic errors.

E_d (keV)	$d\sigma / d\Omega$ (μb)	Statistical Error (μb)	Total Error (μb)
200	0.23	0.03	0.04
250	1.12	0.06	0.10
260	1.56	0.20	0.27
270	1.81	0.10	0.17
280	2.51	0.26	0.36
290	3.26	0.17	0.30
300	3.35	0.3	0.43
310	4.26	0.23	0.40
327	7.06	0.45	0.73
335	6.97	0.39	0.67
340	8.31	0.49	0.82
350	10.42	0.52	0.93

Table B-6 Excitation function data for $^{13}C(d, p)^{14}C$ reaction in lab. system at 128° lab. angle. Total error consists of statistical and systematic errors.

E_d (keV)	$d\sigma / d\Omega$ (μb)	Statistical Error (μb)	Total Error (μb)
200	0.17	0.03	0.04
250	0.98	0.05	0.09
260	1.28	0.18	0.24
270	1.64	0.09	0.16
280	2.10	0.24	0.32
290	2.59	0.15	0.25
300	3.14	0.29	0.42
310	3.91	0.23	0.38
327	5.75	0.40	0.63
335	7.01	0.39	0.67
340	8.04	0.48	0.80
350	7.96	0.45	0.77

Table B-7 Excitation function data for $^{13}C(d, p)^{14}C$ reaction in lab. system at 146° lab. angle. Total error consists of statistical and systematic errors.

E_d (keV)	$d\sigma / d\Omega$ (μb)	Statistical Error (μb)	Total Error (μb)
200	0.09	0.02	0.02
250	0.90	0.05	0.09
260	1.13	0.17	0.22
270	1.61	0.09	0.16
280	2.12	0.24	0.33
290	2.73	0.15	0.26
300	3.22	0.30	0.43
310	4.08	0.23	0.39
327	6.76	0.44	0.71
335	7.26	0.40	0.69
340	8.10	0.49	0.81
350	10.60	0.53	0.95

Table B-8 Excitation function data for $^{13}C(d, p)^{14}C$ reaction in lab. system at 164° lab. angle. Total error consists of statistical and systematic errors.

E_d (keV)	$d\sigma / d\Omega$ (μb)	Statistical Error (μb)	Total Error (μb)
200	0.14	0.03	0.03
250	1.21	0.06	0.11
260	1.75	0.22	0.29
270	2.61	0.29	0.39
280	3.32	0.30	0.44
290	4.66	0.48	0.67
300	5.69	0.40	0.63
310	7.24	0.75	1.04
327	12.82	0.62	1.13
335	14.95	1.40	2.00
340	17.39	0.73	1.43
350	19.54	1.75	2.53

Appendix C

CROSS SECTION DATA OF $^{13}C(d, p)^{14}C$ REACTION

Table C-1 Differential cross section data for $^{13}C(d, p)^{14}C$ reaction in lab. system for 200 keV deuteron lab. energy. Total error consists of statistical and systematic errors.

Angles (lab.)	Angles (c.m.)	$d\sigma/d\Omega_{lab}$ (μb)	$d\sigma/d\Omega_{c.m}$ (μb)	Statistical Error (μb)	Total Error (μb)
30°	30.51	1.73	1.68	0.09	0.15
48°	-	-	-	-	-
58°	58.87	1.01	0.99	0.14	0.20
66°	66.93	0.86	0.84	0.06	0.10
80°	81.01	0.42	0.42	0.08	0.10
90°	91.02	0.33	0.33	0.04	0.05
110°	110.96	0.22	0.23	0.03	0.04
120°	120.89	0.17	0.18	0.05	0.05
128°	128.81	0.17	0.17	0.03	0.04
138°	138.68	0.10	0.10	0.03	0.03
146°	146.57	0.08	0.09	0.02	0.02
155°	155.43	0.10	0.10	0.03	0.04
164°	164.28	0.14	0.14	0.03	0.03

Table C-2 Differential cross section data for $^{13}C(d, p)^{14}C$ reaction in lab. system for 250 keV deuteron lab. energy. Total error consists of statistical and systematic errors.

Angles (lab.)	Angles (c.m.)	$d\sigma/d\Omega_{lab}$ (μb)	$d\sigma/d\Omega_{c.m}$ (μb)	Statistical Error (μb)	Total Error (μb)
30°	30.57	11.25	10.88	0.17	0.61
48°	-	-	-	-	-
58°	58.97	7.31	7.16	0.27	0.71
66°	67.04	4.72	4.65	0.11	0.30
80°	81.12	3.14	3.12	0.22	0.35
90°	91.14	2.18	2.18	0.08	0.17
110°	111.07	1.10	1.12	0.06	0.10
120°	120.99	0.98	1.00	0.10	0.14
128°	128.9	0.95	0.98	0.05	0.09
138°	138.76	0.91	0.94	0.10	0.13
146°	146.64	0.87	0.90	0.05	0.09
155°	155.48	1.02	1.05	0.10	0.15
164°	164.31	1.17	1.21	0.06	0.11

Table C-3 Differential cross section data for $^{13}C(d, p)^{14}C$ reaction in lab. system for 270 keV deuteron lab. energy. Total error consists of statistical and systematic errors.

Angles (lab.)	Angles (c.m.)	$d\sigma/d\Omega_{lab}$ (μb)	$d\sigma/d\Omega_{c.m}$ (μb)	Statistical Error (μb)	Total Error (μb)
30°	30.59	20.03	19.34	0.75	1.53
48°	48.88	13.82	13.45	0.26	0.80
58°	59.00	13.44	13.15	0.26	0.78
66°	67.08	8.02	7.88	0.20	0.52
80°	81.16	5.72	5.68	0.17	0.40
90°	91.18	3.37	3.37	0.13	0.27
110°	111.11	1.79	1.81	0.10	0.17
120°	121.02	1.71	1.74	0.10	0.17
128°	128.93	1.60	1.64	0.09	0.16
138°	138.79	1.57	1.62	0.09	0.16
146°	146.66	1.55	1.61	0.09	0.16
155°	155.50	1.81	1.88	0.10	0.18
164°	164.33	2.51	2.61	0.29	0.39

Table C-4 Differential cross section data for $^{13}C(d, p)^{14}C$ reaction in lab. system for 290 keV deuteron lab. energy. Total error consists of statistical and systematic errors.

Angles (lab.)	Angles (c.m.)	$d\sigma/d\Omega_{lab}$ (μb)	$d\sigma/d\Omega_{c.m}$ (μb)	Statistical Error (μb)	Total Error (μb)
30°	30.61	31.39	30.27	1.19	2.40
48°	48.91	23.13	22.49	0.42	1.32
58°	59.04	21.37	20.90	0.41	1.25
66°	67.12	12.46	12.25	0.32	0.81
80°	81.20	9.65	9.58	0.28	0.66
90°	91.22	5.27	5.27	0.21	0.42
110°	111.15	3.22	3.26	0.17	0.30
120°	121.06	2.83	2.89	0.16	0.27
128°	128.96	2.52	2.59	0.15	0.25
138°	138.82	2.56	2.65	0.15	0.26
146°	146.68	2.64	2.73	0.15	0.26
155°	155.52	2.81	2.92	0.16	0.28
164°	164.34	4.47	4.66	0.48	0.67

Table C-5 Differential cross section data for $^{13}C(d, p)^{14}C$ reaction in lab. system for 310 keV deuteron lab. energy. Total error consists of statistical and systematic errors.

Angles (lab.)	Angles (c.m.)	$d\sigma/d\Omega_{lab}$ (μb)	$d\sigma/d\Omega_{c.m}$ (μb)	Statistical Error (μb)	Total Error (μb)
30°	30.63	45.31	43.64	1.76	3.51
48°	48.94	34.92	33.92	0.64	2.00
58°	59.07	27.99	27.36	0.58	1.67
66°	67.15	19.01	18.67	0.48	1.23
80°	81.24	11.56	11.47	0.38	0.84
90°	91.26	7.31	7.31	0.30	0.60
110°	111.19	4.20	4.26	0.23	0.40
120°	121.09	3.81	3.89	0.22	0.38
128°	129.00	3.81	3.91	0.23	0.38
138°	138.85	3.78	3.91	0.23	0.38
146°	146.71	3.93	4.08	0.23	0.39
155°	155.53	5.11	5.32	0.26	0.48
164°	164.35	6.94	7.24	0.75	1.04

Table C-6 Differential cross section data for $^{13}C(d, p)^{14}C$ reaction in lab. system for 335 keV deuteron lab. energy. Total error consists of statistical and systematic errors.

Angles (lab.)	Angles (c.m.)	$d\sigma/d\Omega_{lab}$ (μb)	$d\sigma/d\Omega_{c.m}$ (μb)	Statistical Error (μb)	Total Error (μb)
30°	30.66	76.86	73.92	2.98	5.93
48°	48.97	52.93	51.36	1.03	3.09
58°	59.11	46.58	45.49	0.97	2.79
66°	67.20	29.59	29.06	0.78	1.94
80°	81.29	18.40	18.26	0.62	1.35
90°	91.31	11.18	11.19	0.49	0.94
110°	111.23	6.86	6.97	0.39	0.67
120°	121.14	6.56	6.71	0.38	0.65
128°	129.03	6.82	7.01	0.39	0.67
138°	138.88	6.82	7.05	0.39	0.68
146°	146.73	6.99	7.26	0.40	0.69
155°	155.55	10.06	10.49	0.48	0.90
164°	164.36	14.31	14.95	1.40	2.00

Table C-7 Differential cross section data for $^{13}C(d, p)^{14}C$ reaction in lab. system for 350 keV deuteron lab. energy. Total error consists of statistical and systematic errors.

Angles (lab.)	Angles (c.m.)	$d\sigma/d\Omega_{lab}$ (μb)	$d\sigma/d\Omega_{c.m}$ (μb)	Statistical Error (μb)	Total Error (μb)
30°	30.67	103.37	99.34	3.73	7.70
48°	49.00	79.11	76.71	1.37	4.44
58°	59.14	63.08	61.56	1.23	3.69
66°	67.22	44.36	43.55	1.04	2.78
80°	81.32	23.04	22.86	0.75	1.67
90°	91.34	15.90	15.91	0.63	1.27
110°	111.26	10.25	10.42	0.52	0.93
120°	121.16	7.76	7.95	0.45	0.77
128°	129.06	7.74	7.96	0.45	0.77
138°	138.90	9.22	9.55	0.50	0.88
146°	146.75	10.20	10.60	0.53	0.95
155°	155.57	14.90	15.55	0.64	1.26
164°	164.37	18.68	19.54	1.75	2.53

Appendix D

TYPICAL LISTING OF INPUT FILE OF 'TWOFNR' CODE

```
51      1   1                13C(d,p)14C
   1.            0.          15.          1.          50.          0.350        1.0
   2.2           0.5          1.0         0.5
   3.1           0.          16.
   3.2           0.          16.          1.
   4.1           2.          13.          1.           6.          1.           0.5
   4.2           1.          14.          1.           6.          0.5          0.0          5.947
   5.1          95.00         7.03        6.00         0.0         1.47         0.77         1.50
   6.1           1.20         0.80
   7.1           0.9964       2.05        0.54
   5.2          52.00        14.50        7.50         0.          1.30         0.77         1.25
   6.2           1.03         0.55
   7.2           0.9964       1.11        0.53
   9.           61.           3.          0.

 0 0 0 0 4 0 0 0 0 1
   1.0           1.47        23.          2.           2.         120.
   2.            0.           1.          0.0          0.          0.          1.0          0.5
   3.           49.000        1.50        4.946        2.224
   4.            2.
   5.            1.          13.0         0.           1.2692       .758        6.00
                 1.3
   6.            1.           1.          0.           1.50         .50
                 1.3
   7.            1.8898

9                                MIX CALLED
   1.         -1.0000                     8.
```

References

[1] G. D. Putt. *Nucl. Phys.* **A161** (1971) 547-564.

[2] T.J.Yule and W.Haeberli. *Nucl. Phys.* **A117** (1968) 1-10.

[3] J. B. Marion, *Rev. Mod. Phys.* **33** (1961) 139-147.

[4] L. C. Feldman and S. T. Picraus. *Handbook for Material Analysis*, Academic Press, New York, 109-309.

[5] W.A.Fowler, C.C.Lauritsen and T.Lauritsen. *Rev. Mod. Phys.* **20** (1948) 236-277.

[6] C.Rolfs, W.S.Rodney, S.Durrance and H.Winkler. *Nucl. Phys.* **A240** (1975) 221-234.

[7] T.Freye, H.Lorenz-Wirzba, B.Cleff, H.P.Trautvetter and C.Rolfs. *Z. Physik* **A281** (1977) 211-218.

[8] C.R.Brune. *Private Communication*, 1994.

[9] B.Fernandez and J.S.Blair. *Phys. Rev.* **C1** (1970) 523-538.

[10] M. Uhrmacher. *Nucl. Inst. Meth. Phys. Research* **B9**(1985) 234-248.

[11] Husain Al-Juwair, G.Blume, R.J.Jaarsma, C.R.Meitzler and K.H.Purser *Nucl. Inst. Meth. Phys. Research* **B24/25** (1987) 810-812.

[12] A.A.M.Al-Jalal, A.A.Naqvi, H.A.Al-Juwair, A.Coban, F.Z.Khiari. *A.J.S.E.* **20** (1995) 179-195.

[13] EG & G ORTEC. *Silicon Charged Particle Radiation Detectors Instruction Manual.*

[14] H.A.Al-Juwair and R.E.Abdel-Aal. *IEEE Tran. Nucl. Sci.* **36** (1989) 611-614.

[15] R.E.Abdel-Aal and H.A.Al-Juwair. *IEEE Tran. Nucl. Sci.* **36** (1989) 687-691.

[16] R.E.Abdel-Aal and H.A.Al-Juwair. *IEEE Tran. Nucl. Sci.* **36** (1989) 692-696.

[17] A.A.Naqvi, Abdulaziz M.Al-Jalal, A.Coban and F.Z.Khiari, *IL Nuovo Cemento,* **105A** (1992) 1501-1506.

[18] Philip R. Bevington. *Data Reduction and Error Analysis for the Physical Sciences.* McGraw-Hill Book Company, New York (1969).

[19] R.K.Das, T.B.Clegg, H.J.Karwowski and E.J.Ludwig. *Phys. Rev. Lett.* **68** (1992) 1112-1115.

[20] L.D.Khutson and W.Haeberli. *Progress in Particle and Nuclear Physics Vol.3, edited by Sir Denys Wilkinson.* Pergamon Press, Oxford (1980).

[21] P.E.Hodgson. *Nuclear reactions and Nuclear Structure*, Clarendon Press, Oxford (1971).

[22] M. Toyama and M. Igarashi. Computer code TWOFNR (unpublished).

[23] C.M.Bhat, J.E.Bowsker, T.B.Clegg, H.J.Karwowski and E.J.Ludwig. *Phys. Rev.* **C38** (1988) 1537-1546.

[24] C.M.Bhat, Y.Tagishi, E.J.Ludwig and B.A.Brown. *Phys. Rev.* **C34** (1986) 736-739.

[25] G. R. Satchler. *Introduction to Nuclear Reactions*, John Wiley and Sons, New York (1980).

[26] C.M.Perey and F.G.Perey. *Atomic Data and Nuclear Data Tables* **13** (1974) 239-337.